

**Universität Stuttgart**

# **Simulation and Modeling of Polyelectrolyte Gels**

Von der Fakultät für Mathematik und Physik der Universität  
Stuttgart zur Erlangung der Würde eines Doktors der  
Naturwissenschaften (Dr. rer. nat.) genehmigte Abhandlung

Vorgelegt von  
Jonas Landsgesell  
aus Herrenberg

**Hauptberichter:** Prof. Dr. Christian Holm

**Mitberichter:** Prof. Dr. Johannes Roth

**Tag der mündlichen Prüfung:** 21.02.2020

Institut für Computerphysik der Universität Stuttgart

2020



---

# Contents

|          |  |           |
|----------|--|-----------|
| <b>1</b> | <b>Introduction</b>                                    | <b>11</b> |
| <b>2</b> | <b>Theoretical Background</b>                          | <b>17</b> |
| 2.1      | Canonical Ensemble . . . . .                           | 17        |
| 2.1.1    | Chemical Potential . . . . .                           | 21        |
| 2.2      | (Semi-)Grand-Canonical Ensemble . . . . .              | 22        |
| 2.3      | Chemical Reactions . . . . .                           | 24        |
| 2.3.1    | Example: Ideal Weak Acid . . . . .                     | 28        |
| 2.4      | Poisson-Boltzmann Theory . . . . .                     | 31        |
| 2.4.1    | Derivation of the Poisson-Boltzmann Equation . . . . . | 36        |
| 2.4.2    | Pressure Tensor . . . . .                              | 39        |
| 2.5      | Particle-Based Simulations . . . . .                   | 42        |
| 2.5.1    | Interactions . . . . .                                 | 43        |
| 2.5.2    | Molecular Dynamics Simulation . . . . .                | 46        |
|          | Langevin Dynamics . . . . .                            | 48        |
| 2.5.3    | Monte Carlo Simulation . . . . .                       | 49        |
|          | Canonical Monte Carlo . . . . .                        | 51        |
|          | Grand-canonical Monte Carlo . . . . .                  | 53        |
|          | Widom Insertion Method . . . . .                       | 55        |
|          | Reaction Ensemble Method . . . . .                     | 58        |
|          | Constant pH Method . . . . .                           | 60        |
| 2.5.4    | General Simulation Protocol . . . . .                  | 63        |

|          |   |            |
|----------|---|------------|
| 2.6      | Polymer Physics . . . . .   | 65         |
| 2.6.1    | Freely Jointed Chain . . . . .  | 66         |
| 2.6.2    | Gel Models . . . . .  | 67         |
|          | Donnan Model . . . . .  | 68         |
|          | Flory-Huggins / Flory-Rehner Models . . .                                   | 72         |
|          | Katchalsky Model . . . . .  | 76         |
|          | Periodic Gel Model . . . . .  | 78         |
| <b>3</b> | <b>Improved Gel Models: Cell-Gel Models</b>                                 | <b>81</b>  |
| 3.1      | Periodic Gel Model . . . . .  | 85         |
| 3.2      | Single-Chain Models . . . . .   | 86         |
| 3.3      | Pressures in an Affinely Compressed Cylinder . .                            | 89         |
| 3.4      | Particle-Based Single-Chain Cell-Gel Model . . .                            | 90         |
| 3.5      | Poisson-Boltzmann Cell-Gel Model . . . . .                                  | 94         |
| 3.5.1    | Pressures in the Poisson-Boltzmann Model                                    | 98         |
| 3.6      | Strong Polyelectrolyte Gels . . . . .                                       | 100        |
| 3.6.1    | Pressure-Volume Curves . . . . .  | 100        |
| 3.6.2    | Swelling Equilibria . . . . .   | 102        |
| 3.6.3    | Bulk Modulus . . . . .  | 109        |
| 3.6.4    | Influence of the Relative Permittivity . . .                                | 115        |
| 3.6.5    | Mass-Based Degree of Swelling (for Monodisperse Gels) . . . . .             | 117        |
| 3.6.6    | Chain Length Polydispersity . . . . .                                       | 119        |
| 3.6.7    | Influence of the Different Imposed Charge Densities in the PB CGM . . . . . | 125        |
| 3.6.8    | Influence of the Different Imposed Values of $A$ . . . . .                  | 127        |
| 3.7      | Summary . . . . .   | 128        |
| <b>4</b> | <b>Comparison with Experiment</b>   | <b>131</b> |
| 4.1      | Experiments . . . . .   | 132        |

|          |  |            |
|----------|--|------------|
| 4.2      | Simulations . . . . .  | 133        |
| 4.3      | Mapping of Simulations to Experiments . . . . .                                    | 134        |
| 4.4      | Single Networks . . . . .  | 138        |
| 4.4.1    | Salt Concentration Dependence of the Swelling<br>Equilibrium . . . . .             | 138        |
| 4.4.2    | Chain Length Dependence of the Salt Re-<br>jection . . . . .                       | 140        |
| 4.5      | Interpenetrating Networks . . . . .  | 141        |
| 4.6      | Possible Reasons for Deviations Between Experi-<br>ments and Simulations . . . . . | 143        |
| 4.7      | Summary . . . . .  | 146        |
| <b>5</b> | <b>Grand-Reaction Method</b>   | <b>149</b> |
| 5.1      | pH and Ionic Strenght . . . . .  | 151        |
| 5.2      | Ideal Donnan Equilibrium in the Presence of Weak<br>Acidic Groups . . . . .        | 154        |
| 5.3      | Reservoir with Interactions . . . . .  | 160        |
| 5.3.1    | Solving the Defining Equations for the<br>Reservoir Composition . . . . .          | 161        |
| 5.3.2    | Particle Exchanges . . . . .   | 167        |
| 5.4      | Chemical Reactions in an Interacting System . . .                                  | 169        |
| 5.5      | Simulation Protocol and Setup . . . . .  | 173        |
| 5.5.1    | Validation of the Reservoir Chemical Po-<br>tentials . . . . .                     | 175        |
| 5.6      | Polyelectrolyte Solution . . . . .   | 177        |
| 5.6.1    | Effect of pH and Salt . . . . .  | 177        |
| 5.7      | Summary . . . . .  | 182        |
| <b>6</b> | <b>Weak Polyelectrolyte Gels</b>   | <b>185</b> |
| 6.1      | Simulation Protocol and Setup . . . . .  | 186        |
| 6.1.1    | Particle-Based Simulations . . . . .   | 187        |

---

|          |  |            |
|----------|--|------------|
| 6.1.2    | Poisson-Boltzmann Cell-Gel Model . . . . .   | 187        |
| 6.2      | pH-dependent Swelling of Gels . . . . .  | 189        |
| 6.3      | Salt-Dependent Swelling of Gels . . . . .  | 193        |
| 6.4      | Degree of Dissociation on Compression . . . . .  | 195        |
| 6.5      | Charge Profile Along the Polymer Backbone . . . . .  | 197        |
| 6.6      | Outlook: Weak Polyampholyte Gels . . . . .   | 199        |
| 6.7      | Summary . . . . .  | 202        |
| <b>7</b> | <b>Conclusion</b>  | <b>205</b> |
| <b>8</b> | <b>Appendix</b>  | <b>215</b> |
| 8.1      | Directory Structure: Simulation Scripts and Figures  | 215        |
| 8.2      | Polymer Monomer Distribution in the Poisson-<br>Boltzmann Cell-Gel Model . . . . .               | 216        |
| 8.3      | Strong Polyelectrolyte Gels . . . . .  | 217        |
| 8.3.1    | Swelling Equilibria . . . . .  | 217        |
|          | Salt Concentration Dependence . . . . .  | 218        |
|          | Charge Fraction Dependence . . . . .   | 218        |
|          | Chain Length Dependence . . . . .  | 220        |
| 8.3.2    | Comparison of the CGMs to the Periodic<br>Gel Model . . . . .                                    | 220        |
| 8.4      | Charge Fraction Dependence of the Swelling of<br>Single Gels and Interpenetrating Gels . . . . . | 222        |
| <b>9</b> | <b>Acknowledgement</b>   | <b>225</b> |

---

# Zusammenfassung

Diese Dissertation behandelt die Entwicklung von Computermodellen zur Beschreibung von Polyelektrolytnetzwerken. Im Rahmen der Untersuchung von Polymersystemen hat sich gezeigt, dass Computersimulationen, neben Experimenten und Theorien, ein wertvolles Untersuchungswerkzeug darstellen: Auf der einen Seite erlauben Computersimulationen die Untersuchung von Eigenschaften, welche im Experiment nicht direkt zugänglich sind. Auf der anderen Seite verzichten Computermodelle auf stark vereinfachende Annahmen wie sie häufig in analytischen Theorien anzutreffen sind.

Nachdem wir in Kapitel 2 die theoretischen Grundlagen unserer Modelle beschrieben haben, entwickeln wir in Kapitel 3 zwei aufeinander aufbauende Computermodelle, welche zur Beschreibung der elastischen Eigenschaften von Polyelektrolytgel dienen: das Einzelketten-Zellen-Gelmodell (ZGM) und das Poisson-Boltzmann Zellen-Gelmodell (PB ZGM). Ausgangspunkt ist das bereits bekannte teilchenbasierte periodische Gelmodell [1], welches in Bild 0.1 i) dargestellt ist.

Im ersten Modellierungsschritt wird das Gel in einzelne Ketten zerlegt (siehe Abbildung 0.1 ii)). Unser Einzelketten-Zellen-Gelmodell besitzt eine ausgezeichnete Übereinstimmung mit

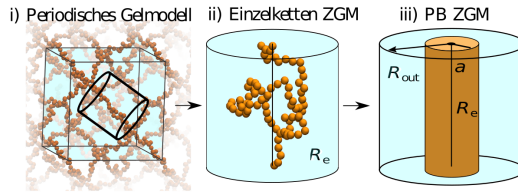


Abbildung 0.1: Schema verschiedener Gelmodelle, adaptiert aus [2]. i) Vergrößertes (periodisches) Gelmodell, ii) Einzelketten-Zellen-Gelmodell, iii) PB-Zellen-Gelmodell

dem periodischen Gelmodell, da es ebenfalls teilchenbasiert ist und somit dieselben ungenäherten Teilchenwechselwirkungen verwendet. Das Einzelketten-Zellen-Gelmodell reduziert jedoch die Zahl der zu simulierenden Teilchen um einen Faktor 16 und verringert daher die Berechnungskosten um circa eine Größenordnung.

Im Poisson-Boltzmann Zellen-Gelmodell (siehe Abbildung 0.1 iii)) wird die teilchenbasierte Beschreibung zu Gunsten einer dichte-basierten Beschreibung aufgegeben. Dadurch werden die Berechnungen nochmals um mehrere Größenordnungen beschleunigt, was jedoch mit einer verringerten Genauigkeit des Modells erkauft wird. Die hohe Berechnungseffizienz des PB ZGM erlaubt das Verhalten von Polyelektrolytgele in großen Parameterräumen zu untersuchen, was zur Optimierung von Gelparametern für reale Anwendungen nötig ist. Im Gegensatz zu dem ähnlich effizienten Katchalsky-Modell [3] ist unser Poisson-Boltzmann ZGM auch für hochgeladenen Gele anwendbar.

In Kaptiel 4 vergleichen wir erfolgreich das vergrößerte periodische Gelmodell und das Poisson-Boltzmann ZGM mit dem



---

experimentell beobachteten Quellverhalten von Polyacrylsäure-Hydrogelen.

Da viele Polyelektrolytgele aus Bausteinen bestehen, welche chemisch reaktiv sind, ist es wichtig diese Eigenschaft korrekt in Computermodellen abzubilden. Zur Untersuchung dieser schwachen Polyelektrolytgele führen wir in Kapitel 5 eine Methode zur Simulation von Ionisationsgleichgewichten in solchen Systemen ein. Der pH-Wert und die Salzkonzentration werden durch die Zusammensetzung der Überstandslösung definiert. Unsere Implementierung des Teilchenaustausches mit der Überstandslösung vermeidet bekannte Artefakte und unphysikalische Parameterkombinationen, die in der Literatur vielfach Anwendung fanden [4].

In Kapitel 6 benutzen wir die im vorigen Kapitel eingeführte Simulationsmethode zur Beschreibung des pH abhängigen Quellverhaltens schwacher Polyelektrolytgele. Im Poisson-Boltzmann Zellen-Gelmodell verwenden wir den Ansatz der Ladungsregulierung, um schwache Gruppen zu modellieren [5]. Alle unsere Modelle beschreiben den experimentell bekannten Kollaps von schwachen Polyelektrolytgelen bei hohem pH-Wert und die nicht-monotone Quellung als Funktion der Reservoirsalzkonzentration.



---

# 1 Introduction

DNA, RNA and proteins have vital functions for living organisms and are examples for the material class of polymers. Polymers are macromolecules built from repeating building blocks, so called monomers. Crosslinking charged polymers, i.e. polyelectrolytes, results in the material class of hydrogels. Their main characteristics are the response to external stimuli like pH or salt concentration and the capability to take up more than a hundred times their own weight in water. Therefore, hydrogels are well-known as superabsorbers which find applications, for example, in agriculture [6, 7] or hygiene products like diapers. Among other proposed applications like desalination of sea water [8, 9, 10], pH-sensors [11] or mechanical actors [12], hydrogels are envisioned to revolutionize drug delivery [13, 14].

Depending on the application, different gels with distinct properties are required. Accurate and computationally feasible gel models allow chemical engineers to select the optimal gel for a given task in much less time and with much less resources as would otherwise be required if they had to rely solely on experiments. This thesis aims at introducing such models, and for the first time perform accurate particle-based simulations of hydrogels including acid-base reactions.

Existing atomistic molecular dynamics simulations can serve this purpose in principle, but are too costly to exploring large parameter spaces for typical applications. Providing relief to these computational limitations, our periodic gel model i) in Figure 1.1 replaces a group of atoms by a more coarse-grained representation with effective interactions [15].

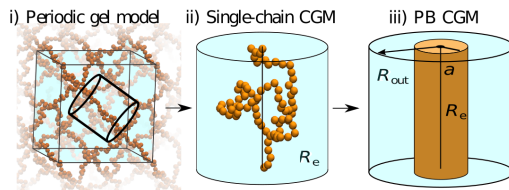


Figure 1.1: A sketch of the different models employed in this thesis: i) the periodic gel model; ii) the single-chain cell-gel model; and iii) a density based continuum model. Ions in solution are not shown. For more details we refer to Chapter 3

In the case of polyacrylic acid, pictured in Figure 1.2, all atoms of a monomer are grouped into an individual “bead”. This coarsening greatly reduces the degrees of freedom of the system enabling (still costly) screening of parameter spaces on compute clusters.

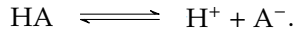
In Chapter 3, we introduce two new gel models, which are computationally less expensive than the previously employed periodic gel model but are similarly accurate. We introduce these models in the spirit of multiscale modeling which aims to strike the balance between very detailed, but computationally expensive microscopic models and cheaper, in tendency more inaccurate, macroscopic models [16]. For a quick impression of our modeling approach, we refer to Figure 1.1: we extract

---

information from the many-chain gel model with explicit salt ions i) to justify the simplification step to the single-chain model ii). The single-chain model is also particle-based and uses the same interactions as the original periodic gel model i), however it only describes the behavior of a single chain as well as the surrounding salt ions, and therefore again greatly reduces the number of particles which need to be simulated.

Additional drastic reductions in the computational cost will be realized through another coarse-graining step towards a continuum level description, where interactions are approximated on a mean-field level. In this simplified Poisson-Boltzmann cell-gel model iii), we approximate the single polymer chain by a simple cylinder with an effective end-to-end radius  $R_e$ , line charge density, and ionic exclusion radius  $a$ . The salt ions in solution are modeled as radially symmetric continuum density fields.

In the remaining Chapters 5 and 6, we investigate how to model the pH dependent swelling of polyelectrolyte gels which is mainly based on the presence of reactive monomers. These gels contain acids or bases which can release or take up a proton and, therefore, take part in a chemical reaction in the form of



A common weak acidic monomer used in synthetic hydrogels is polyacrylic acid (see Figure 1.2).

The chemical reaction couples the charge state of the weak polyelectrolyte gel to the pH value of the surrounding solution: At low pH the monomers are mostly in the state HA and, therefore,

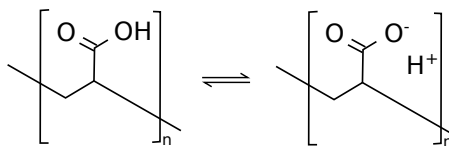


Figure 1.2: Polyacrylic acid is an example for a weak polyelectrolyte.

the gel is neutral, while at high pH the monomers are mostly in the state  $\text{A}^-$  such that the gel is negatively charged. If the gel is highly charged it tends to swell more compared to the case where it is neutral.

Over the course of this PhD project, I created and contributed to the following publications (see Chapter 7 for details):

1. **J. Landsgesell**, C. Holm., J. Smiatek “Wang-Landau Reaction Ensemble Method: Simulation of Weak Polyelectrolytes and General Acid-Base Reactions” In: *Journal of Chemical Theory and Computation* 13(2)(852–862) (2017)  
URL: <https://dx.doi.org/10.1021/acs.jctc.6b00791>
2. **J. Landsgesell**, C. Holm, J. Smiatek. “Simulation of weak polyelectrolytes: A comparison between the constant pH and the reaction ensemble method” In: *The European Physical Journal Special Topics* 226(725–736) (2017)  
URL: <https://dx.doi.org/10.1140/epjst/e2016-60324-3>
3. T. Richter, **J. Landsgesell**, P. Košovan, C. Holm. “On the efficiency of a hydrogel-based desalination cycle” In: *Desalination* 414(28–34) (2017)  
URL: <https://dx.doi.org/10.1016/j.desal.2017.03.027>

- 
4. D. Sean, **J. Landsgesell**, C. Holm. "Computer Simulations of Static and Dynamical Properties of Weak Polyelectrolyte Nanogels in Salty Solutions" In: *Gels* 4(2)(2) (2018)  
URL: <https://dx.doi.org/10.3390/gels4010002>
  5. **J. Landsgesell**, L. Nova, O. Rud, F. Uhlik, D. Sean, P. Hebbeker, C. Holm, P. Košovan. "Simulations of ionization equilibria in weak polyelectrolyte solutions and gels" In: *Soft Matter* 15(6)(1155-1185) (2019)  
URL: <http://dx.doi.org/10.1039/C8SM02085J>
  6. **J. Landsgesell**, C. Holm. "Cell Model Approaches for Predicting the Swelling and Mechanical Properties of Polyelectrolyte Gels" In: *Macromolecules* (2019)  
URL: <https://doi.org/10.1021/acs.macromol.9b01216>
  7. **J. Landsgesell**, S. Sean, P. Kreissl, K. Szuttor, C. Holm. "Modeling Gel Swelling Equilibrium in the Mean Field: From Explicit to Poisson-Boltzmann Models" In: *Physical Review Letters* 122(208002) (2019)  
URL: <https://dx.doi.org/10.1103/PhysRevLett.122.208002>
  8. L. Arens, D. Barther, **J. Landsgesell**, C. Holm, M. Wilhelm. "Poly (sodium acrylate) hydrogels: Synthesis of various network architectures, local molecular dynamics, salt partitioning, desalination and simulation" In: *Soft Matter* (2019)  
URL: <https://dx.doi.org/10.1039/C9SM01468C>
  9. F. Weik, R. Weeber, K. Szuttor, K. Breitsprecher, J. de Graaf, M. Kuron **J. Landsgesell**, H. Menke, D. Sean, C. Holm, "ESPReso 4.0 – an extensible software package for simulating soft matter systems" In: *The European Physical Journal*

*Special Topics* 227(14)(1789–1816) (2019)

URL: <http://dx.doi.org/10.1140/epjst/e2019-800186-9>

10. D. Sean, **J. Landsgesell**, C. Holm. “Influence of weak groups on polyelectrolyte mobilities” In: *Electrophoresis* 40(5)(799–809) (2019)

URL: <https://dx.doi.org/10.1002/elps.201800346>

11. F. Weik, K. Szuttor, **J. Landsgesell**, C. Holm. “Modeling the current modulation of dsDNA in nanopores – from mean-field to atomistic and back” In: *The European Physical Journal Special Topics* 227(14)(1639–1655) (2019)

URL: <https://dx.doi.org/10.1140/epjst/e2019-800189-3>

This thesis mainly discusses the topics of publications 2, 3 and 4. We plan to publish the content of chapters 5 and 6 in two separate papers 12 and 13. The papers in preparation are:

12. **J. Landsgesell**, P. Hebbeker, O. Rud, R. Lunkad, P. Košov, C. Holm. “Grand-reaction Method for Simulations of Ionization Equilibria and Ion Partitioning in a Broad Range of pH and Ionic Strength” In: *ChemRxiv* (2019)

URL: <https://doi.org/10.26434/chemrxiv.9741746.v2>

13. **J. Landsgesell**, P. Hebbeker, P. Košov, C. Holm. “Simulating the pH-dependent Swelling of Weak Gels”

14. A. Tagliabue, **J. Landsgesell**, M. Mella, C. Holm. “On the Formation of Electrostatically Cross-linked Gels via Self-assembly of Charged Star-shaped Copolymers”

15. J. Finkbeiner, **J. Landsgesell**, C. Holm. “Dilution Behaviour of Weak Acids Under the Influence of Strong Electrostatic Interactions”



---

## 2 Theoretical Background

The theoretical description of polyelectrolyte gels is based on a statistical mechanics view which is recapitulated in this chapter. Depending on the physical situation, different ensembles are most suitable to describe the system at hand. An isolated system with constant volume and particle number is best investigated in the microcanonical (NVE) ensemble. For a system with constant particle number, volume, and temperature the canonical ensemble is best suited. The thermodynamic framework of chemical reactions, the Poisson-Boltzmann mean-field theory, different gel models, and the justification for the later used simulation methods are provided in this chapter.

### 2.1 Canonical Ensemble

One of the most commonly used statistical ensembles is the canonical ensemble, which keeps the particle number  $N$ , the volume  $V$  and the temperature  $T$  constant. Therefore, this ensemble is often abbreviated as “NVT ensemble”. The partition function  $Z_{(N,V,T)}$  as well as the free energy  $F(N, V, T) = -k_B T \ln(Z(N, V, T))$  fully describe the system. The partition function can be obtained by

## 2 Theoretical Background

---

integrating the Boltzmann factor over the phase space<sup>1</sup>  $\{(\vec{r}^N, \vec{p}^N)\}$  spanned by all particle positions  $\vec{r}^N$  and momenta  $\vec{p}^N$ :

$$Z(N, V, T) = \frac{1}{h^{3N} N!} \int_{V^N} d^{3N} r \int_{\mathbb{R}^{3N}} d^{3N} p \exp(-\beta \mathcal{H}(\vec{r}^N, \vec{p}^N)),$$

where  $h$  is the Planck constant,  $\mathcal{H}$  is the Hamilton function of the system. The inverse of the Boltzmann constant  $k_B$  times the absolute temperature  $T$  is denoted by  $\beta = 1/(k_B T)$ . For a system composed by different types  $i$  of particles the canonical partition function is given by an integral over all possible positions and particle impulses:

$$Z(\{N_i\}, V, T) = \prod_i \frac{1}{h^{3N_i} N_i!} \int_{V^{N_i}} d^{3N_i} r \int_{\mathbb{R}^{3N_i}} d^{3N_i} p \exp(-\beta \mathcal{H}(\vec{r}^{\{N_i\}}, \vec{p}^{\{N_i\}})),$$

where the total energy of the system is a sum of the kinetic energy and the potential energy:

$$\mathcal{H} = E_{\text{kin}}(\vec{p}^{\{N_i\}}) + E_{\text{pot}}(\vec{r}^{\{N_i\}}),$$

and where the superscript  $\{N_i\}$  denotes that all particles of each type  $i$  are considered. The kinetic energy is the sum of the kinetic energy of all  $N_i$  particles (of each species  $i$ ):

$$E_{\text{kin}}(\vec{p}^{\{N_i\}}) = \sum_i \sum_{j=1}^{N_i} \frac{\vec{p}_{(j,i)}^2}{2m_i},$$

where  $\vec{p}_{(j,i)}$  denotes the momentum of the  $j$ -th particle of species  $i$ .

---

<sup>1</sup>We use the notation  $f(\vec{r}^N, \vec{p}^N) = f(\vec{r}_1, \vec{r}_2, \dots, \vec{r}_N, \vec{p}_1, \vec{p}_2, \dots, \vec{p}_N)$  as well as  $d^{3N} r = \prod_{j=1}^N dx_j dy_j dz_j$  and analogously  $d^{3N} p = \prod_{j=1}^N dp_{x,j} dp_{y,j} dp_{z,j}$ .

The potential energy is a function of the particle positions and does not depend on the momenta. Due to this independence, we can separate the partition function into the dimensionless “kinetic partition function”  $Z_{\text{kin}}$  and the dimensionless “configurational partition function”  $\Xi$  (where we introduced the factor  $1 = \frac{V^{N_i}}{V^{N_i}}$ ):

$$Z(\{N_i\}, V, T) = \underbrace{\left( \prod_i \frac{V^{N_i}}{N_i! h^{3N_i}} \int_{\mathbb{R}^{3N_i}} \exp(-\beta E_{\text{kin}}(\vec{p}^{\{N_i\}})) d^{3N_i} p \right)}_{Z_{\text{kin}}(\{N_i\}, V, T)} \times \underbrace{\left( \prod_i \frac{1}{V^{N_i}} \int_{V^{N_i}} d^{3N_i} r \exp(-\beta E_{\text{pot}}(\vec{r}^{\{N_i\}})) \right)}_{\Xi(\{N_i\}, V, T)}. \quad (2.1)$$

Therefore, the free energy splits into a kinetic part and a configuration part:

$$F = -k_B T \ln(Z(\{N_i\}, V, T)) = F_{\text{id}} + F_{\text{conf}}. \quad (2.2)$$

For a non-interacting system, the potential energy is  $E_{\text{pot}} \equiv 0$  and the configurational partition function is equal to one. In this case the ideal gas result for the partition function is obtained, where the integrals occurring in the kinetic partition function can be

solved analytically:

$$\begin{aligned}
 Z_{\text{kin}}(\{N_i\}, V, T) &= \prod_i \frac{V^{N_i}}{N_i! h^{3N_i}} \left( \int_{\mathbb{R}^3} \exp[-\beta E_{\text{kin}}(\vec{p}_{k_i})] d^3 p_{k_i} \right)^{N_i} \\
 &= \prod_i \frac{V^{N_i}}{N_i! h^{3N_i}} \prod_i \left( \sqrt{\frac{2\pi m_i}{\beta}} \right)^{3N_i} \\
 &= \prod_i \frac{1}{N_i!} \left( \frac{V}{\lambda_i^3} \right)^{N_i},
 \end{aligned}$$

where  $m_i$  is the mass and  $\lambda_i = h \sqrt{\frac{\beta}{2\pi m_i}}$  is the thermal de Broglie wave length of a particle of species  $i$ .

However, in most interesting cases the particles in a system interact and the configurational partition function is a non-trivial multidimensional integral which cannot be solved analytically without making simplifying assumptions. Typical simplifications employ the saddle-point approximation in order to obtain analytical expressions for the partition function [17]. We will later investigate one such simplified expression for charged systems (see Section 2.4).

Although the partition function contains all information about the system, we are usually more interested in observing average values of an observable  $\mathcal{A}(\vec{r}^N, \vec{p}^N)$ . In the canonical ensemble the average value of an observable is given by:

$$\langle \mathcal{A} \rangle_{\{N, V, T\}} = \frac{\int_{V^N} d^{3N} r \mathcal{A}(\vec{p}^N, \vec{r}^N) e^{-\beta H(\vec{r}^N, \vec{p}^N)}}{Z(N, V, T)}.$$

For calculating these averages, the concept of numerical computer

simulations is very successful [18, p. 24-27] and we introduce it in Section 2.5.

### 2.1.1 Chemical Potential

The chemical potential is an observable which is important in the context of chemical reactions (see Section 2.3). Starting from the free energy of a canonical system we can derive the chemical potential  $\mu_i$ . The chemical potential is defined as the change in free energy which occurs when changing the particle number of species  $i$  at fixed temperature, volume and number of other particles  $N_{j \neq i}$ :

$$\mu_i := \frac{\partial F(N_1, \dots, N_i, V, T)}{\partial N_i} = \frac{F(N_1, \dots, N_i + 1, V, T) - F(N_1, \dots, N_i, V, T)}{1} \quad (2.3)$$

Because the free energy splits into an ideal part and an excess part (see equation (2.2)) we can also split the chemical potential in the same way:

$$\mu_i = \mu_i^{\text{id}} + \mu_i^{\text{ex}} \quad (2.4)$$

We independently evaluate the ideal (kinetic) chemical potential and the excess chemical potential.

The kinetic free energy is given by:

$$F^{\text{id}}(\{N_i\}, V, T) = -k_B T \sum_i \left( -\ln(N_i!) + N_i \ln \left( \frac{V}{\lambda_i^3} \right) \right),$$

which implies the following ideal chemical potential

$$\begin{aligned}\mu_i^{\text{id}} &= F^{\text{id}}(\dots, N_i + 1, \dots, V, T) - F^{\text{id}}(\dots, N_i, \dots, V, T) \\ &= -kT \ln \left( \frac{V}{(N_i + 1)\lambda_i^3} \right) \approx k_B T \ln(c_i \lambda_i^3).\end{aligned}\tag{2.5}$$

In contrast to the ideal chemical potential, the excess chemical potential  $\mu_i^{\text{ex}}$  is a complicated function of all interactions in the system. We come back on how to determine the excess chemical potential in Section 2.5.3.

## 2.2 (Semi-)Grand-Canonical Ensemble

For a system with constant volume and temperature but the possibility to exchange particles with a reservoir, the (semi-)grand-canonical ensemble is used. In this ensemble the chemical potentials  $\mu_i$  of each exchangeable species  $i$  is constant. If all species may be exchanged this is the grand-canonical ensemble, otherwise the ensemble is referred to as semi-grand-canonical ensemble. The partition function  $\mathcal{Z}_G$  of the grand-canonical

ensemble with  $z$  particle species is given by [19]:

$$\begin{aligned}
 \mathcal{Z}_G(\mu_1, \dots, \mu_z, V, T) &= \sum_{N_1=0}^{\infty} \cdots \sum_{N_z=0}^{\infty} Z(\{N_i\}, V, T) \exp\left(\beta \sum_{i=1}^{i=z} N_i \mu_i\right) \\
 &= \sum_{N_1=0}^{\infty} \cdots \sum_{N_z=0}^{\infty} \underbrace{\left( \prod_{i=1}^z \frac{\left(\frac{V}{\lambda_i^3}\right)^{N_i}}{N_i!} \right)}_{Z_{\text{kin}}(\{N_i\}, V, T)} \times \\
 &\quad \underbrace{\left( \prod_{i=1}^z \frac{1}{V^{N_i}} \int_{V^{N_i}} \exp\left[-\beta E_{\text{pot}}(\vec{r}_1^{N_1}, \dots, \vec{r}_z^{N_z})\right] d\vec{r}^{3N_1} \dots d\vec{r}^{3N_z} \right)}_{\Xi(\{N_i\}, V, T)} \times \\
 &\quad \exp\left(\beta \sum_{i=1}^z N_i \mu_i\right),
 \end{aligned} \tag{2.6}$$

where  $\vec{r}_j^{N_j}$  is the vector containing all particle positions of the particles of type  $j$  and where  $Z(\{N_i\}, V, T)$  is the canonical partition function. The (semi-)grand potential is  $\Omega = -k_B T \ln(\mathcal{Z}_G)$ . Averages of an observable  $\mathcal{A}$  are given by:

$$\langle \mathcal{A} \rangle = \frac{\sum_{N_1} \cdots \sum_{N_z} \sum_k \mathcal{A}_k \exp(-\beta \mathcal{H}_k + \beta \sum_{i=1}^{i=z} N_i \mu_i)}{\sum_{N_1} \cdots \sum_{N_z} \sum_k \exp(-\beta \mathcal{H}_k + \beta \sum_{i=1}^{i=z} N_i \mu_i)} \tag{2.7}$$

#### Note 1

The particle reservoir is fully described by the set of chemical

potentials  $\{\mu_i\}$  of all species  $i$  contained in the reservoir and the temperature. For a reservoir representing an aqueous solution containing ions of valency  $z_i$  and concentration  $c_i^{\text{res}}$ , the chemical potentials of the occurring species are coupled by two constraints:

1. The macroscopic electroneutrality condition [20]. In other words, in nature there is, in very good approximation, no *macroscopic* solution of ions which is not electroneutral:

$$\sum_i c_i^{\text{res}} z_i = 0. \quad (2.8)$$

2. The autodissociation of water which connects the chemical potential of  $\text{H}^+$  and  $\text{OH}^-$  ions due to the chemical reaction  $\text{H}_2\text{O} \rightleftharpoons \text{H}^+ + \text{OH}^-$ . If the concentrations of  $\text{H}^+$  and  $\text{OH}^-$  ions are negligible this condition can be ignored.

We elaborate these two points in greater detail later in Chapter 5.

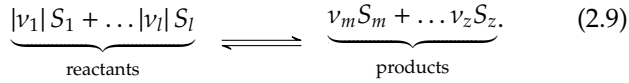
## 2.3 Chemical Reactions

In this section the concept of chemical reactions is introduced. Chemical reactions are fundamentally important in aqueous solutions of weak polyelectrolytes because they couple the concentrations of  $\text{H}^+$  and  $\text{OH}^-$  ions and, additionally, determine the charge state of the weak polyelectrolyte.

A chemical reaction turns reactants  $(S_1, \dots, S_l)$  into products  $(S_m,$



$\dots S_z$ ). We can denote this process in a chemical equation:



Here, the stoichiometric coefficient  $v_i := \Delta N_i$  is the change of numbers of particles of particle type  $S_i$  due to the reaction. For products  $v_i > 0$  is positive, for reactants  $v_i < 0$  is negative.

Chemical equilibrium is reached when the concentration of products and reactants does not change over time anymore [21]. In the state of chemical equilibrium (at constant temperature and constant volume) the sum of the chemical potentials  $\mu_i$  times the stoichiometric coefficients  $v_i$  is zero:

$$dF(N_i, V, T) = \sum_i v_i \mu_i = 0.$$

Often the chemical potentials  $\mu_i$  are defined with respect to a reference state (see Note 2). In this case we have the equality  $\mu_i = \mu_i^\ominus + k_B T \ln\left(\frac{c_i}{c^\ominus}\right) + \mu_i^{\text{ex}}$ , where  $c_i = \frac{N_i}{V}$  is the concentration of species  $i$  and  $\mu_i^\ominus$  an arbitrary reference state [22] with reference concentration  $c^\ominus$ .

### Note 2

In the derivation of the chemical potential in Section 2.1.1, no reference state occurred.

We can rearrange equation (2.5) and formally introduce an

arbitrary reference chemical potential  $\mu_i^\ominus$ :

$$\begin{aligned}
 \mu_{\text{id}} &= k_B T \ln(c_i \lambda_i^3) \\
 &= k_B T \ln\left(c_i \lambda_i^3 \frac{c^\ominus}{c^\ominus}\right) \\
 &= \underbrace{k_B T \ln\left(\lambda_i^3 c^\ominus\right)}_{\mu_i^\ominus} + k_B T \ln\left(\frac{c_i}{c^\ominus}\right).
 \end{aligned} \tag{2.10}$$

In our simulations, the solvent is not explicitly modeled and there is no interaction between the particles and the solvent. Therefore, the reference chemical potential in equation (2.10) is different from the infinite dilution reference state used in experiments. In the experiment, at infinite dilution, ions interact with the solvent, but not with other ions which are infinitely far away. In this case the following definitions are made:

$$\begin{aligned}
 \mu_i &= k_B T \ln(c_i \lambda_i^3) + \mu_i^{\text{ex}} \\
 &= \underbrace{k_B T \ln\left(\lambda_i^3 c^\ominus\right) + \mu_i^{\text{ex},\ominus}}_{\tilde{\mu}_i^\ominus} + k_B T \ln\left(\frac{c_i}{c^\ominus}\right) + \underbrace{(\mu_i^{\text{ex}} - \mu_i^{\text{ex},\ominus})}_{\tilde{\mu}_i^{\text{ex}}},
 \end{aligned} \tag{2.11}$$

with a modified reference chemical potential  $\tilde{\mu}_i^\ominus$  and a modified excess chemical potential  $\tilde{\mu}_i^{\text{ex}}$  which satisfies that the excess chemical potential goes to zero in the infinite dilution limit  $\lim_{c_i \rightarrow 0} \tilde{\mu}_i^{\text{ex}} = 0$ .

With the above definition of the chemical potentials, the equilib-

rium constant  $K$  is given by:

$$K = \exp\left(\beta \sum_i v_i (\mu_i - \mu_i^\ominus)\right) = \exp\left(-\beta \sum_i v_i \mu_i^\ominus\right) = \exp(-\beta \Delta F^\ominus), \quad (2.12)$$

which can equivalently be written (using the definition of the chemical potentials above) as:

$$K = \prod_i \left( \frac{c_i \exp(\beta \mu_i^{\text{ex}})}{c^\ominus} \right)^{v_i} = \prod_i \left( \frac{c_i \gamma_i}{c^\ominus} \right)^{v_i}, \quad (2.13)$$

where we abbreviated  $\gamma_i = \exp(\beta \mu_i^{\text{ex}})$  in the last step.

In chemistry, the activity  $a_i = \exp(\beta(\mu_i - \mu_i^\ominus)) = c_i \gamma_i / c^\ominus$  of species  $i$  is introduced for convenience (and we will use this convention in chapters 5 and 6 too). With this abbreviation the equilibrium constant is equivalently given by <sup>2</sup>:

$$K = \prod_i a_i^{v_i}. \quad (2.14)$$

The equilibrium constant can be determined from experiment via the concentrations in the infinite dilution limit:

$$K = \lim_{c_i \rightarrow 0} \prod_i \left( \frac{c_i}{c^\ominus} \right)^{v_i}. \quad (2.15)$$

The choice of the experimental reference state guarantees that

---

<sup>2</sup>Sometimes people define the activity by  $a_i = \exp\left(\frac{\tilde{\mu}_i - \tilde{\mu}_i^\ominus}{RT}\right)$ . Then they employed:

$a_i = \exp\left(\frac{\mu_i - \mu_i^\ominus}{k_B T}\right)$  and inserted  $1 = \frac{N_A}{N_A}$ , identifying the universal gas constant  $R = k_B N_A$  and  $\tilde{\mu}_i = N_A \mu_i$ . Reporting the activity like this does not change the value of  $a_i$ .

the activity coefficients  $\gamma_i \rightarrow 1$  in the limit of infinite (high) dilution.

### 2.3.1 Example: Ideal Weak Acid

Many phenomena occurring in reacting systems can be understood through examination of the ideal case, where there are no interactions present, resulting in activity coefficients  $\gamma_i$  equal to one.

Let us consider the example of a Brønsted acid HA releasing a proton ( $\text{H}^+$ ):



In the ideal case ( $\forall i : \gamma_i = 1$ ) the equilibrium constant is given by:

$$K = \frac{c_{\text{A}^-} c_{\text{H}^+}}{c_{\text{HA}} c^{\ominus}} \quad (2.17)$$

For the simple example of an ideal acid one finds two important laws: first, the response to a change in  $\text{H}^+$  concentration, and second, the law of dilution.

#### Response to a Change in $\text{H}^+$ Concentration

The law of mass action (equation 2.17) can be used to understand the dissociation response of an ideal acid. Since  $K$  is a constant, a change of the  $\text{H}^+$  concentration has to affect the other two

concentrations. In the following, we look at the degree of dissociation<sup>3</sup>  $\alpha$ , defined as:

$$\alpha := \frac{c_{A^-}}{c_{HA} + c_{A^-}}.$$

Rearranging equation (2.17) yields the ideal titration curve (or Henderson-Hasselbalch equation):

$$\alpha = \frac{1}{1 - 10^{pK - \text{pH}^{\text{id}}}}, \quad (2.18)$$

where  $pK = -\log_{10}(K)$ , and  $\text{pH}^{\text{id}} = -\log_{10}(c_{\text{H}^+}/c^{\ominus})$ . This equation describes how an ideal system reacts to a change of  $\text{H}^+$  concentration, see figure 2.1

An increase in pH can be achieved in the experiment via adding a strong base, a decrease in pH can be achieved by adding a strong acid to the solution.

## Law of Dilution

Let us assume that the concentration of titratable units is given by  $c_0 = c_{HA} + c_{A^-}$ . If protons are only generated by the dissociation of the acid, then the concentration of  $\text{H}^+$  is equal to the concentration of  $\text{A}^-$ :  $c_{\text{H}^+} = c_{A^-}$ . Rewriting equation (2.17) gives

$$K = \frac{c_{A^-}^2}{(c_0 - c_{A^-})c^{\ominus}},$$

---

<sup>3</sup>Alternatively, sometimes the degree of association is chosen:  $\bar{n} = 1 - \alpha = c_{HA}/(c_{HA} + c_{A^-})$ .

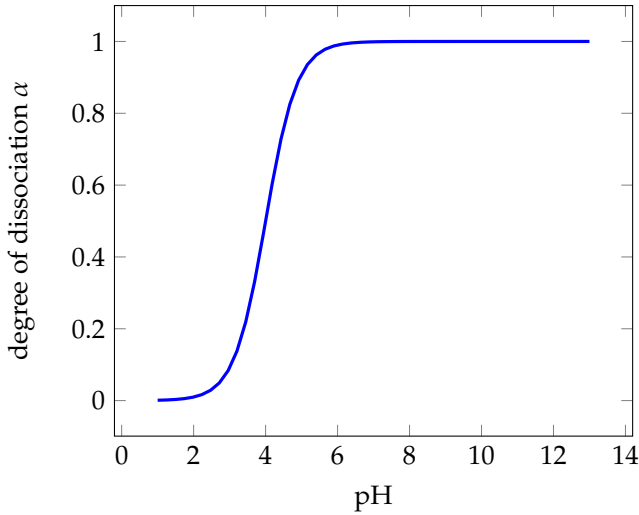


Figure 2.1: Ideal titration curve for  $pK = 4$ : The higher the pH value, the lower the  $H^+$  concentration, resulting in an increased dissociation ( $\alpha \rightarrow 1$ ). In contrary, the lower the pH value, the higher is the  $H^+$  concentration, resulting in a decreased dissociation ( $\alpha \rightarrow 0$ ).

which yields for the degree of dissociation  $\alpha := \frac{c_{A^-}}{c_0}$ :

$$\alpha = \frac{\frac{1}{2} \sqrt{Kc^\ominus} \sqrt{Kc^\ominus + 4c_0} - Kc^\ominus}{c_0}. \quad (2.19)$$

This is called the law of dilution. It predicts the two limiting cases  $\lim_{c_0 \rightarrow \infty} \alpha = 0$  and  $\lim_{c_0 \rightarrow 0} \alpha = 1$  which is easily seen by applying L'Hôpital's rule. As a result, the dissociation of the acid increases as the concentration of titratable units decreases. The law of dilution does not hold anymore if a significant amount of  $H^+$  is generated from the autodissociation of water  $H_2O \rightleftharpoons H^+ + OH^-$ . If the released amount of  $H^+$

ions is negligible to the protons released by the autodissociation reaction of water, the pH is essentially unaltered and constant. Further dilution does not affect the degree of dissociation. For interacting systems the law of dilution does not have to hold.

## 2.4 Poisson-Boltzmann Theory

The Poisson-Boltzmann (PB) theory is frequently used for describing electrostatic interactions in ionic solutions [23]. In this chapter, the main assumptions needed for deriving the PB equation are stated. The following derivation of the PB theory is inspired by publications [24, 17]. We begin by considering a system of volume  $V$ , which contains some fixed charge density  $\rho_f$  and additionally some mobile ions, which explore the phase space  $\{\vec{r}^N, \vec{p}^N\}$ .

The canonical partition function of this system is [17]:

$$Z(\{N_i\}, V, T) = \underbrace{\prod_i \frac{V^{N_i}}{N_i! \lambda_i^{3N_i}}}_{Z_{\text{kin}}} \cdot \underbrace{\prod_i \frac{1}{V^{N_i}} \int d^{3N_i} r \exp(-\beta \hat{E}_{\text{Coulomb}}(\{\vec{r}_i\}))}_{Z_{\text{conf}}}, \quad (2.20)$$

As seen before, the free energy  $F = k_B T \ln(Z)$  splits into an ideal part and a part relating to the configuration (see equation (2.2)). Using the Stirling approximation  $\ln(N!) \approx N \ln(N) - N$ , we obtain

## 2 Theoretical Background

---

for the ideal part:

$$\beta F_{\text{id}} = \ln \left( \prod_i \frac{N_i! \lambda_i^{3N_i}}{V^{N_i}} \right) = \sum_i \ln \left( \frac{N_i! \lambda_i^{3N_i}}{V^{N_i}} \right) \approx \sum_i N_i (\ln(N_i \lambda_i^3 / V) - 1), \quad (2.21)$$

$$= \sum_i \int_V c_i (\ln(c_i \lambda_i^3) - 1) \quad (2.22)$$

where  $\lambda_i = h / \sqrt{2\pi m_i k_B T}$  is the thermal de Broglie wave length and  $i$  is the index of the different species present in the system.

Unfortunately, the configurational partition function in equation (2.20) cannot be easily used to gain further insights since it explicitly depends on the instantaneous charge density  $\hat{\rho}(\vec{r})$  [17]:

$$\hat{E}_{\text{Coulomb}}(\{\vec{r}_i\}) = \frac{1}{2} \int_V d^3r \hat{\rho}(\vec{r}) \hat{\psi}(\vec{r}), \quad (2.23)$$

where  $\hat{\psi}(\vec{r})$  is the total electrostatic potential and  $\hat{\rho}(\vec{r}) = \hat{\rho}_f(\vec{r}) + \sum_i q_i \delta(\vec{r} - \vec{r}_i)$  is the total charge density for a given configuration. The electrostatic potential itself depends on the positions of all charges ( $\vec{r}_i$  and the fixed charge density). We can formally obtain  $\hat{\psi}$  via integrating the Poisson equation  $\Delta \hat{\psi}(\vec{r}) = \frac{-\hat{\rho}(\vec{r})}{\epsilon_0 \epsilon_r}$  with the Greens function  $G(\vec{r} - \vec{r}')$ :

$$\hat{\psi}(\vec{r}) = \int_V d^3r' \frac{-\hat{\rho}(\vec{r}')}{\epsilon_0 \epsilon_r} \underbrace{\frac{-1}{4\pi |\vec{r} - \vec{r}'|}}_{G(\vec{r} - \vec{r}')} \quad (2.24)$$

where  $\epsilon_r$  is the relative permittivity and  $\epsilon_0$  is the vacuum permittivity. This results in an alternative expression for the instan-



taneous Coulomb energy (neglecting the renormalization for self-energy terms proportional to  $G(\vec{0})$  [17])

$$\hat{E}_{\text{Coulomb}}(\{\vec{r}_i\}) = \frac{1}{2} \int_V d^3r \int_V d^3r' \frac{\hat{\rho}(\vec{r}, t) \hat{\rho}(\vec{r}')}{4\pi\epsilon_0\epsilon_r |\vec{r} - \vec{r}'|}. \quad (2.25)$$

For a rigorous treatment of how to obtain the Poisson-Boltzmann free energy functional we refer to [17] and [25]. The main idea is to introduce a mean-field  $\psi^{\text{MF}}$  and an average charge density  $\rho^{\text{MF}}$ . It is then assumed that the configurational partition function can be approximated via  $Z_{\text{conf}} = \sum_i \exp(-\beta E_{\text{Coulomb},i}) \approx \exp(-\beta \langle E_{\text{Coulomb}} \rangle)$ . From the analytical treatment [17] it is found that  $\langle E_{\text{Coulomb}} \rangle$  is the mean-field electrostatic energy:

$$F_{\text{conf}} = \langle E_{\text{Coulomb}} \rangle = \frac{1}{2} \int_V d^3r \rho^{\text{MF}}(\vec{r}) \psi^{\text{MF}}(\vec{r}), \quad (2.26)$$

where  $\rho^{\text{MF}}(\vec{r})$  is the mean-field charge density given by:

$$\rho^{\text{MF}}(\vec{r}) = \rho_f(\vec{r}) + \sum_i q_i c_i(\vec{r}), \quad (2.27)$$

and  $c_i(\vec{r})$  denotes the density of particles of type  $i$ .

### Note 3

Sometimes different notations for the electrostatic energy are used in literature. Using the Maxwell equation for the mean field charge density  $\rho^{\text{MF}} = \epsilon_0 \epsilon_r \nabla \cdot \vec{E}^{\text{MF}}$  (with the mean electric field  $\vec{E}^{\text{MF}}$ ) we can rewrite the PB electrostatic energy

$$\begin{aligned} \langle E_{\text{Coulomb}} \rangle &= \frac{1}{2} \int_V d^3r \rho^{\text{MF}}(\vec{r}) \Psi^{\text{MF}}(\vec{r}) \\ &= \frac{\epsilon_0 \epsilon_r}{2} \int_V d^3r \nabla \cdot \vec{E}^{\text{MF}} \Psi^{\text{MF}}(\vec{r}) \end{aligned}$$

using the relation

$$\nabla(\vec{E}^{\text{MF}} \Psi^{\text{MF}}) = \Psi^{\text{MF}} \nabla \cdot \vec{E}^{\text{MF}} + \vec{E}^{\text{MF}} \cdot \nabla \Psi^{\text{MF}}$$

and  $\nabla \Psi^{\text{MF}} = -\vec{E}^{\text{MF}}$ , we obtain:

$$\langle E_{\text{Coulomb}} \rangle = \frac{\epsilon_0 \epsilon_r}{2} \left( \int_V d^3r \nabla \cdot (\Psi^{\text{MF}}(\vec{r}) \vec{E}^{\text{MF}}) + \int_V E^{\text{MF}^2} d^3r \right)$$

Using Gauss law we obtain

$$\langle E_{\text{Coulomb}} \rangle = \frac{\epsilon_0 \epsilon_r}{2} \left( \int_{\partial V} d\vec{S} \cdot (\Psi^{\text{MF}}(\vec{r}) \vec{E}^{\text{MF}}) + \int_V E^{\text{MF}^2} d^3r \right)$$

However, on the boundary of our volume the total mean electric field perpendicular to the surface is by construction zero (due to charge neutrality) and therefore the first term vanishes if  $\Psi^{\text{MF}}$  does not diverge on the boundary  $\partial V$ .

Hence, the electrostatic energy is alternatively given by:

$$\langle E_{\text{Coulomb}} \rangle = \frac{\epsilon_0 \epsilon_r}{2} \int_V E^{\text{MF}^2} d^3 r$$

Using the superposition principle of electric potentials  $\psi^{\text{MF}} := \psi_m^{\text{MF}} + \psi_f$ , we arrive at the final Poisson-Boltzmann free energy functional:

$$\begin{aligned} F_{\text{PB}}[\{c_i(\vec{r})\}] &= F^{\text{id}} + F^{\text{conf}} \\ &= \sum_i \int_V d^3 r k_B T c_i(\vec{r}) [\ln(c_i(\vec{r}) \lambda_i^3) - 1] \\ &\quad + \frac{1}{2} \sum_i \int_V z_i e_0 c_i(\vec{r}) [\psi^{\text{MF}}(\vec{r}) + \psi_f(\vec{r})] d^3 r \\ &\quad + \frac{1}{2} \int_V d^3 r \rho_f(\vec{r}) \psi_f(\vec{r}) \\ &= \sum_i \int_V d^3 r k_B T c_i(\vec{r}) [\ln(c_i(\vec{r}) \lambda_i^3) - 1] \\ &\quad + \int_V \frac{\epsilon_0 \epsilon_r}{2} E^{\text{MF}^2} d^3 r. \end{aligned} \tag{2.28}$$

From now on we will drop the superscripts MF for simplicity of notation.

The free energy  $F_{\text{PB}}$  describes a canonical system with constant number of particles  $\{N_i\}$ :

$$N_i = \int_V d^3 r c_i(\vec{r}). \tag{2.29}$$

We can obtain the grand potential via a Legendre transforma-

tion [25]:

$$\Omega(V, T, \{\mu_i\}) = F - \sum_i \mu_i N_i, \quad (2.30)$$

where the last term can be rewritten as an integral

$$\sum_i \mu_i N_i = \sum_i \int_V d^3r \mu_i c_i(\vec{r}) \quad (2.31)$$

with  $\mu_i = \mu_i(\vec{r}) = \text{const.}$  The grand potential is, therefore, given by:

$$\Omega[\{c_i\}] = F_{\text{PB}}[\{c_i(\vec{r})\}] - \sum_{i \in \{+, -\}} \int_V d^3r \mu_i c_i(\vec{r}). \quad (2.32)$$

The Poisson-Boltzmann theory is expected to work well in aqueous solutions if there are no multivalent ions, high charge densities (e.g. at high compression of the gel) or high ionic concentrations [26, 27]. Inaccuracies in Poisson-Boltzmann theories arise due to neglecting ionic correlations and excluded volume effects.

### 2.4.1 Derivation of the Poisson-Boltzmann Equation

Requiring that the variation of the grand potential is extremal yields:

$$\begin{aligned} \frac{\delta \Omega}{\delta c_i} \stackrel{!}{=} 0 &= \frac{\delta F_{\text{PB}}[\{c_i(\vec{r})\}]}{\delta c_i} - \mu_i \\ &= \frac{\delta F_{\text{id}}}{\delta c_i}(\vec{r}) + \frac{\delta F_{\text{ex}}}{\delta c_i}(\vec{r}) - \mu_i \end{aligned}$$

Using equation (2.22) we obtain:

$$\mu_{\text{id}}(\vec{r}) = \frac{\delta F_{\text{id}}}{\delta c_i}(\vec{r}) = k_B T \ln(\lambda_i^3 c_i(\vec{r})) \quad (2.33)$$

Varying the excess contribution

$$F_{\text{ex}} = e_0 \sum_{i \in \{+, -\}} \int_V z_i c_i(\vec{r}) \left[ \frac{1}{2} \Psi_m(\vec{r}) + \Psi_f(\vec{r}) \right] d^3 r + \frac{1}{2} \int_V d^3 r \rho_f(\vec{r}) \Psi_f(\vec{r}),$$

we obtain the excess chemical potential <sup>4</sup>:

$$\mu_{\text{ex}}(\vec{r}) = \frac{\delta F_{\text{ex}}}{\delta c_i}(\vec{r}) = z_i e_0 \left[ \Psi_f(\vec{r}) + \Psi_m(\vec{r}) \right] = z_i e_0 \Psi(\vec{r}).$$

<sup>4</sup> Variation of the excess free energy with respect to the ion density gives two contributions.

The first contribution is the variation of the free energy of the ion-ion interaction where we need to apply the chain rule [25]:

$$\begin{aligned} \frac{\delta}{\delta c_j(r')} \left[ \frac{1}{2} e_0 \sum_{i \in \{+, -\}} z_i \int_V c_i(\vec{r}) \Psi_m(\vec{r}) d^3 r \right] &= \frac{1}{2} e_0 z_j \int_V \left[ \underbrace{\frac{\delta c_j(r)}{\delta c_j(r')}}_{\delta(r-r')} \Psi_m(\vec{r}) + \sum_i c_i(r) \underbrace{\frac{\delta \Psi_m(\vec{r})}{\delta c_j(r')}}_{G(r-r')} \right] d^3 r \\ &= \frac{1}{2} e_0 z_j \left[ \Psi_m(\vec{r}) + \underbrace{\int_V \sum_i c_i(r) G(r-r') d^3 r}_{\Psi_m(\vec{r})} \right] = e_0 z_j \Psi_m(\vec{r}). \end{aligned}$$

The second contribution is,

$$\frac{\delta}{\delta c_j(r')} e_0 \sum_{i \in \{+, -\}} \int_V z_i c_i(\vec{r}) \Psi_f(\vec{r}) d^3 r = e_0 z_i \Psi_f(\vec{r}).$$

## 2 Theoretical Background

---

Therefore in total the chemical potential is given by:

$$\mu_i = k_B T \ln(\lambda_i^3 c_i(\vec{r})) + z_i e_0 \Psi(\vec{r}) \quad (2.34)$$

We can solve for  $c_i(\vec{r})$  which gives

$$\Rightarrow c_i(r) = \frac{\exp(\beta \mu_i)}{\lambda_i^3} \exp(-z_i \beta e_0 \Psi(\vec{r})) = \frac{\exp(\beta \mu_i^{\text{res}})}{\lambda_i^3} \exp(-z_i \beta e_0 \Psi(\vec{r})) \quad (2.35)$$

where we have used the fact that the chemical potential is independent of the location  $\vec{r}$ . Inserting the reservoir chemical potential  $\mu_i^{\text{res}} = k_B T \ln(c_i^{\text{res}} \lambda_i^3) + z_i e_0 \Psi^{\text{res}}$  we finally obtain:

$$c_i(r) = c_i^{\text{res}} \exp(-z_i \beta e_0 (\Psi(\vec{r}) - \Psi^{\text{res}})), \quad (2.36)$$

where  $c_i^{\text{res}}$  is the density in the reservoir. Since potentials can be arbitrarily shifted, we choose  $\Psi^{\text{res}} = 0$  for convenience. The prefactors  $c_i^{\text{res}}$  alone, without the reservoir potential, have no physical meaning<sup>5</sup> [28].

Knowing the functional dependency of the particle densities on the electrostatic potential, we know the charge density in the system and insert it into Gauss's law  $\nabla_{\vec{r}}^2 \Psi(\vec{r}) = -\frac{\rho(\vec{r})}{\epsilon_0 \epsilon_r}$ , obtaining a self-consistent equation for the electrostatic potential:

$$\nabla_{\vec{r}}^2 \Psi(\vec{r}) = -\frac{1}{\epsilon_0 \epsilon_r} \left( \sum_i z_i e_0 c_i^{\text{res}} \exp(z_i \beta e_0 [\Psi^{\text{res}} - \Psi(\vec{r})]) + \rho_f(\vec{r}) \right). \quad (2.37)$$

This is the Poisson-Boltzmann equation.

---

<sup>5</sup> In the canonical ensemble  $c_i^{\text{res}}$  takes the role of a normalization constant such that equation (2.29) is fulfilled.

## 2.4.2 Pressure Tensor

The grand potential is given by the Legendre transformation of the free energy:

$$\Omega = F - \sum_i \mu_i \langle N_i \rangle = -\langle P \rangle V, \quad (2.38)$$

where  $\langle P \rangle$  is the mean pressure and  $\langle N_i \rangle$  the mean particle number of species  $i$  in the system. In integral form the grand potential equals [29]:

$$\Omega = \int_V f[\{c(\vec{r})\}] - \sum_i \mu_i c_i(\vec{r}) dV = - \int_V P(\vec{r}) dV, \quad (2.39)$$

where we have introduced a local pressure  $P(\vec{r})$ . This form is obviously equivalent in regions where there is no interface, or in systems without interactions, since the pressure is isotropic and homogeneous. More care is however required in the presence of interfaces [29]. Making use of the above equation (2.39), we equate the integrands and obtain the result that the local pressure is given by the local energy densities [23, p. 21]

$$P(\vec{r}) = -f[\{c_i(\vec{r})\}] + \sum_i \mu_i c_i(\vec{r}), \quad (2.40)$$

where  $f$  is the free energy density and  $\mu_i$  the chemical potential of species  $i$ , which is imposed in the grand-canonical ensemble. For an ideal gas, equation (2.40) is easily verified: In agreement with equation (2.22) the ideal gas free energy density reads:

$$f[\{c(\vec{r})\}] = k_B T \sum_i c_i(\vec{r}) (\ln(c_i(\vec{r}) \lambda_i^3) - 1). \quad (2.41)$$

## 2 Theoretical Background

---

We obtain the ideal gas pressure by inserting the above free energy density and the chemical potential  $\mu_i = k_B T \ln(c_i \lambda_i^3)$  into equation (2.40):

$$P(\vec{r}) = k_B T \sum_i c_i(\vec{r}), \quad (2.42)$$

where of course the densities  $c_i(\vec{r})$  do not depend on the location ( $c_i(\vec{r}) = \langle N_i \rangle / V$ ) which gives the typical ideal gas result  $P = k_B T \sum_i \langle N_i \rangle / V$ .

Using equations (2.40) and (2.28), we obtain the local pressure in an ionic solution in front of an interface [23]:

$$P(\vec{r}) = k_B T \sum_i c_i(\vec{r}) + \frac{\epsilon_0 \epsilon_r}{2} E(\vec{r})^2. \quad (2.43)$$

Unfortunately, the usage of equation (2.40) is limited, since the local pressure is a tensor in the presence of electric fields [30]. The pressure tensor which governs a PB system is given by the Maxwell pressure tensor and an isotropic kinetic part [28]:

$$\underline{\underline{P}}(\vec{r}) = \left( k_B T \sum_i c_i(\vec{r}) + \frac{\epsilon_0 \epsilon_r}{2} E(\vec{r})^2 \right) \mathbb{1} - \epsilon_0 \epsilon_r \vec{E}(\vec{r}) \otimes \vec{E}(\vec{r}), \quad (2.44)$$

The components of the pressure tensor in a Cartesian coordinate system are illustrated in figure 2.2.



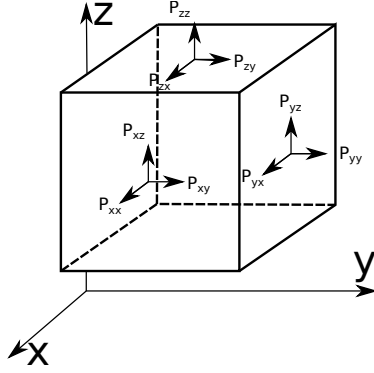


Figure 2.2: The components of the pressure tensor  $\underline{\underline{P}}$  in Cartesian coordinates.

The average pressure normal to a surface  $S$  (with local normal vector  $\vec{n}(\vec{r})$ ) is given by [28]

$$P_S = \frac{1}{S} \int_S \vec{n}^T(\vec{r}) \underline{\underline{P}}(\vec{r}) \vec{n}(\vec{r}) dS, \quad (2.45)$$

where  $dS$  is a surface element and  $S = \int_S dS$  is the surface area.

In Chapter 3, we consider a charged rod in cylindrical confinement with radius  $R_{\text{out}}$  to which we couple a grand-canonical reservoir of ions. Using the above pressure tensor formalism, we obtain the pressure on the cylinder boundaries, which are also predicted by the contact value theorem [31, 24]:

$$P(R_{\text{out}}) = k_B T \sum_i c_i(R_{\text{out}}), \quad (2.46)$$

as well as the pressure on the cylinder top as [28]:

$$P_{\text{cap}} = k_B T \sum_i \langle c_i \rangle_z + \frac{\epsilon_0 \epsilon_r}{2} \langle E_r^2 \rangle_z, \quad (2.47)$$

where  $E_r = -\partial_r \psi(r)$  is the radial component of the electric field,  $\epsilon_0$  is the vacuum permittivity, and  $\langle E_r \rangle_z = \frac{2\pi}{\pi R_{\text{out}}^2} \int_0^{R_{\text{out}}} r E_r(r) dr$  denotes the average radial electric field over the cap.

The result in equation (2.46) *looks like* an ideal gas result only because the mean electric field at the outer cylinder boundary, at  $r = R_{\text{out}}$ , is zero.

## 2.5 Particle-Based Simulations

As we have seen at the beginning of Chapter 2 on statistical mechanics, interactions of particles influence the properties of the system, and only in rare cases can the partition function of the system be determined analytically. In the following, we introduce particle-based simulations which obviate the intractable analytical evaluation of the partition function and instead estimate the average value of an observable  $\mathcal{A}(\vec{r}^N, \vec{p}^N)$  numerically. In the canonical ensemble the average value of an observable is given by:

$$\langle \mathcal{A} \rangle_{\{N, V, T\}} = \int_{V^N} d^{3N} r \mathcal{A}(\vec{r}^N, \vec{p}^N) \underbrace{\frac{1}{Z} e^{-\beta H(\vec{r}^N, \vec{p}^N)}}_{p_k(\vec{r}^N, \vec{p}^N)} \approx \frac{1}{M} \sum_{k=1}^M \mathcal{A}_k,$$

where the estimation in the last step requires the simulation to draw samples  $k$  from the joint probability density of particle positions and momenta  $p_k(\vec{r}^N, \vec{p}^N)$ .

For observables  $\mathcal{A}(\vec{r}^N)$  which do not depend on particle velocities the calculation simplifies because momenta may be integrated out:

$$\begin{aligned} \langle \mathcal{A} \rangle_{\{N,V,T\}} &= \frac{Z_{\text{kin}}^{-1} \frac{1}{V^N} \int_{V^N} d^{3N}r \mathcal{A}(\vec{r}^N) e^{-\beta E_{\text{pot}}(\vec{r}^N)}}{Z_{\text{kin}} \Xi} \\ &= \int_{V^N} d^{3N}r \mathcal{A}(\vec{r}) \underbrace{\frac{1}{V^N \Xi} e^{-\beta E_{\text{pot}}(\vec{r}^N)}}_{p_k(\vec{r}^N)} \approx \frac{1}{M} \sum_{k=1}^M \mathcal{A}_k, \end{aligned} \quad (2.48)$$

where the estimation in the last step only requires that the simulation draws samples  $k$  from the probability density of particle positions  $p_k(\vec{r}^N)$ . In the simple average over discrete states  $k$ , these sample states have to be drawn with a probability proportional to  $p_k(\vec{r}^N)$  — a concept known as importance sampling [18].

Before introducing molecular dynamics simulations, Monte Carlo simulations and associated simulation algorithms for systems with chemical reactions, we define the particle interactions which are present in our systems.

### 2.5.1 Interactions

Systems with interactions deviate from a simple ideal gas. Here we discuss how to incorporate the two most relevant kinds of

interactions into our particle-based simulations: the electrostatic interaction, as well as interactions modeling chemical bonds.

### Electrostatics

The Coulomb interaction energy of two particles with charges  $q_1 = z_1 e_0$ ,  $q_2 = z_2 e_0$  ( $z_1$  and  $z_2$  denoting their valencies) is given by [18]:

$$E_{\text{el}}(r) = \frac{1}{4\pi\epsilon_r\epsilon_0} \frac{q_1 q_2}{r} = \lambda_B k_B T \frac{z_1 z_2}{r},$$

where  $e_0$  is the elementary charge,  $r$  is the particle distance,  $\epsilon_0$  the vacuum permittivity and  $\epsilon_r$  the relative permittivity. In the last equality we used the Bjerrum length  $\lambda_B$  which is the distance where the interaction energy of two elementary charges is equal to the thermal energy  $k_B T$ :

$$k_B T = \frac{e_0^2}{4\pi\epsilon_0\epsilon_r\lambda_B} \Leftrightarrow \lambda_B = \frac{e_0^2}{4\pi\epsilon_0\epsilon_r k_B T}$$

Changing the Bjerrum length at constant temperature (i.e.  $\epsilon_r$ ) can be interpreted as changing the solvent. For water at room temperature the Bjerrum length is  $\lambda_B = 0.71$  nm.

The sum of the pairwise electrostatic energies gives the electrostatic energy of a system of many charges [18]:

$$E_{\text{el}}(\vec{r}^N) = \lambda_B k_B T \sum_{i=1}^{N-1} \sum_{j=i+1}^N \frac{z_i z_j}{|\vec{r}_i - \vec{r}_j|}$$

In simulations employing periodic boundary conditions, the electrostatic energies and forces can be evaluated efficiently

using a numerical electrostatics solver like such as the P<sup>3</sup>M algorithm [32, 33, 34] (for 3D periodic systems).

### Weeks-Chandler-Andersen Potential

One popular interaction potential for simulating almost hard spheres, is the shifted and truncated Lennard-Jones potential, i.e. the Weeks-Chandler-Andersen (WCA) potential [35], which has the following form:

$$E_{\text{WCA}}(r) = \begin{cases} 4\epsilon_{\text{LJ}} \left[ \left( \frac{\sigma}{r} \right)^{12} - \left( \frac{\sigma}{r} \right)^6 \right] + \epsilon_{\text{LJ}} & \text{if } r < 2^{1/6}\sigma \\ 0 & \text{else,} \end{cases}$$

where  $\sigma$  is the diameter of the WCA particles and  $\epsilon_{\text{LJ}}$  the interaction strength of the WCA potential. Since the gradient  $-\nabla_r E_{\text{WCA}}(r) > 0$  is strictly positive, the potential is strictly repulsive. A purely repulsive short ranged interaction mimics a good solvent, in which the particles try to maximize the solvent accessible surface and do not cluster together. Poor solvent conditions could be modeled via an interaction potential with additional attractive parts. When we simulate a charged system a short ranged repulsive potential is needed to avoid the collapse of opposite charges into one point.

### Bonds

In order to simulate polymeric systems, it is essential that the monomers are bonded together. Bonds restrict the accessible phase space of the involved particles. A common interaction

potential for bonding particles together is the “finite extensible nonlinear elastic” (FENE) potential. The FENE bond energy is given by [36]:

$$E_{\text{FENE}}(r) = -\frac{1}{2}k_{\text{FENE}}R_{\text{max}}^2 \ln\left(1 - \left[\frac{r}{R_{\text{max}}}\right]^2\right),$$

where  $k_{\text{FENE}}$  defines the strength of the bond and  $R_{\text{max}}$  is the maximal stretching of the bond: the bond energy diverges when the inter-particle distance  $r$  approaches  $R_{\text{max}}$ .

### 2.5.2 Molecular Dynamics Simulation

Having defined a simulation model, i.e. a set of particles which have certain interactions and the thermodynamic ensemble, we are interested in obtaining information about ensemble averaged observables  $\langle \mathcal{A} \rangle$ .

For a system with conserved energy (i.e. in the microcanonical ensemble) Newton’s equation of motion determine the trajectory of each particle:

$$m_i \frac{d^2 \vec{r}_i}{dt^2} = \vec{F}_i(\vec{r}^N) := -\nabla_i E_{\text{pot}}(\vec{r}^N), \quad (2.49)$$

where  $t$  is the time,  $m_i$  is the mass of particle  $i$ ,  $\vec{r}_i$  its position,  $\vec{F}_i$  the force on particle  $i$  and  $E_{\text{pot}}(\vec{r}^N)$  is the potential energy of the system, a function of all particle coordinates  $\vec{r}^N$ . For a system with WCA, FENE and electrostatic interactions the potential energy is:

$$E_{\text{pot}}(\vec{r}^N) = E_{\text{WCA}}(\vec{r}^N) + E_{\text{FENE}}(\vec{r}^N) + E_{\text{el}}(\vec{r}^N).$$

The idea behind molecular dynamics (MD) simulations is to find these trajectories. The equations of motion for systems containing many interacting particles can typically not be solved analytically [18]. Therefore, we use a numerical integration scheme to solve the equations of motion. In the microcanonical ensemble we are interested in systems with conserved energy. For these it is especially important that the integrator is symplectic and energy conserving [18]. One such integration scheme is the Velocity Verlet integrator [18, 37]:

$$\begin{aligned}\vec{r}_i(t + \Delta t) &= \vec{r}_i(t) + \vec{v}_i(t) \Delta t + \frac{\vec{F}_i(t)}{2m_i} \Delta t^2 \\ \vec{v}_i(t + \Delta t) &= \vec{v}_i(t) + \frac{\vec{F}_i(t) + \vec{F}_i(t + \Delta t)}{2m_i} \Delta t,\end{aligned}$$

where  $t$  is the discrete time,  $\delta t$  the time step of the integrator,  $i$  indexes the particle and  $\vec{r}_i$ ,  $\vec{v}_i$ ,  $m_i$ ,  $\vec{F}_i$  are its position, velocity, mass and the force acting on it.

Solving this set of differential equations, a molecular dynamics simulation generates a trajectory in the  $6N$  dimensional phase space of the  $N$  particle system. Observables are calculated as a time average:

$$\begin{aligned}\langle \mathcal{A} \rangle &= \lim_{T \rightarrow \infty} \frac{1}{T} \int_0^T \mathcal{A}(t) dt \\ &\approx \frac{1}{N\Delta t} \sum_{i(t=0)=0}^{i(t=T)=N} \mathcal{A}(i\Delta t) \Delta t = \frac{1}{N} \sum_{i=0}^N \mathcal{A}(i\Delta t),\end{aligned}\tag{2.50}$$

which is equal to the ensemble average of ergodic systems.

### Langevin Dynamics

When simulating other ensembles (like e.g. the canonical ensemble) we can modify the deterministic Newtonian equations of motion and add random influences, converting the differential equation to a stochastic differential equation. This approach is for example taken in the Langevin equation for performing simulations at constant temperature.

The Langevin equation couples the system to a heat bath [37] and therefore acts as a “Langevin thermostat”. We introduce a Gaussian random force  $\vec{R}_i(t)$  and a damping constant  $\gamma$  in Newton’s equations of motion (2.49) [37]:

$$m_i \frac{d^2 \vec{r}_i}{dt^2} = -\nabla_i E_{\text{pot}}(\vec{r}^N) - \gamma m_i \frac{d\vec{r}_i}{dt} + \vec{R}_i(t).$$

This Gaussian random force on particle  $i$  has the mean value zero:

$$\langle \vec{R}_i(t) \rangle = 0$$

and a Dirac- $\delta$  distributed autocorrelation:

$$\langle \vec{R}_i(t) \cdot \vec{R}_i(t + \tau) \rangle = 6\gamma k_B T m_i \delta(\tau), \quad (2.51)$$

with the thermal energy  $k_B T$  and the lag time  $\tau$ . The random forces on two different particles at a given time  $t$  are uncorrelated, i.e.  $\langle \vec{R}_i(t) \cdot \vec{R}_j(t) \rangle = \delta_{i,j}$ .



### 2.5.3 Monte Carlo Simulation

Monte Carlo simulations allow the calculation of ensemble averages [38]. Applying Monte Carlo sampling does not produce physically meaningful trajectories in contrast to MD which solves Newton's equations of motion. In statistical physics the probability  $P_i$  of a given state  $i$  is directly encoded in the partition sum:

$$Z = \sum_i w_i \implies P_i = \frac{w_i}{Z}, \quad (2.52)$$

where  $w_i$  is the weight of state  $i$ , which is in the example of the canonical partition function given by  $w_i = \frac{1}{h^{3N}N!} \exp(-\beta \mathcal{H}_i)$ . Taking samples according to the probability distribution  $P$  allows to calculate the ensemble averages  $\mathcal{A}$  very efficiently:

$$\langle \mathcal{A} \rangle = \sum_i \mathcal{A}_i P_i \approx \frac{1}{N} \sum_s \mathcal{A}_s, \quad (2.53)$$

where the first sum runs over all states and the last sum runs over all samples which were collected. This is the idea of importance sampling.

We can construct a Markov chain which is transitioning from one state  $i$  to another state  $j$  such that all states are visited with frequencies proportional to their probability  $P$ . A Monte Carlo algorithm generates a Markov chain which has the (unique) stationary distribution equal to the probability distribution  $P$ . The algorithm has the Markov property because the probability for the transition to a new state solely depends on the last state but no previous ones.

In the Metropolis algorithm [39] we propose a new state, but

## 2 Theoretical Background

---

accept or reject it with a certain acceptance probability. Therefore, the Monte Carlo method is a rejection sampling method [38]. The acceptance probability has to make sure that the resulting transition probabilities  $P_{i \rightarrow j}$  (from state  $i$  to state  $j$ ) and  $P_{j \rightarrow i}$  (from state  $j$  to state  $i$ ) obey detailed balance [18]:

$$P_{i \rightarrow j} P_i = P_{j \rightarrow i} P_j \Leftrightarrow \frac{P_{i \rightarrow j}}{P_{j \rightarrow i}} = \frac{P_j}{P_i}, \quad (2.54)$$

with the probabilities  $P_i$  and  $P_j$  resulting from the statistical ensemble we want to simulate.

Given a symmetric proposal probability of states  $g_{i \rightarrow j} = g_{j \rightarrow i}$  we have the transition probability  $P_{i \rightarrow j} = g_{i \rightarrow j} \cdot \text{acc}_{i \rightarrow j}$ . The detailed balance criterion (2.54) is then:

$$\frac{g_{i \rightarrow j} \cdot \text{acc}_{i \rightarrow j}}{g_{j \rightarrow i} \cdot \text{acc}_{j \rightarrow i}} = \frac{P_j}{P_i}. \quad (2.55)$$

One possible choice of the acceptance probability which guarantees detailed balance is:

$$\text{acc}_{i \rightarrow j} = \min\left(1, \frac{P_j}{P_i}\right). \quad (2.56)$$

This is easily understood: if  $\frac{P_i}{P_j} > 1$ , then  $\frac{P_j}{P_i} < 1$  and we obtain  $\frac{\text{acc}_{i \rightarrow j}}{\text{acc}_{j \rightarrow i}} = \frac{P_j}{P_i}$ .

Using the Metropolis choice (2.56) for the acceptance probability, we therefore, transit from state  $i$  to  $j$  and obeying detailed balance. Technically, we draw a uniform random number  $r$  between 0 and 1, accept the transition when  $r < \text{acc}_{i \rightarrow j}$  and reject the attempted transition otherwise. Although there are other choices for the ac-

ceptance criterion — like  $\text{acc}_{i \rightarrow j} = \frac{P_j}{P_i + P_j}$  — the Metropolis choice is typically used because it has good convergence properties: if the proposed state has a higher probability  $p_j$  than the previous state, then the move is always accepted. In some situations, convergence of the algorithm can further be improved by breaking that symmetry in the proposal probabilities [40]:  $g_{i \rightarrow j} \neq g_{j \rightarrow i}$ . The detailed balance condition (2.54) is then rearranged resulting in:

$$\frac{\text{acc}_{i \rightarrow j}}{\text{acc}_{j \rightarrow i}} = \frac{P_j g_{j \rightarrow i}}{P_i g_{i \rightarrow j}} \implies \text{acc}_{i \rightarrow j} = \min\left(1, \frac{P_j g_{j \rightarrow i}}{P_i g_{i \rightarrow j}}\right) \quad (2.57)$$

which can be used with the Metropolis choice resulting in the acceptance probability for the Metropolis-Hastings algorithm[40].

### Canonical Monte Carlo

From the partition function (2.1) we see that the probability of finding a certain configuration  $i$  in the canonical ensemble is given by:

$$P_i = \frac{\exp(-\beta E_{\text{pot},i})}{\Xi}.$$

Using equation (2.56) we obtain the acceptance probability:

$$\text{acc}_{i \rightarrow j} = \min\left(1, \exp(-\beta(E_{\text{pot},j} - E_{\text{pot},i}))\right). \quad (2.58)$$

One can combine and/or mix Monte Carlo and molecular dynamics steps in one simulation and still take samples from the canonical partition function [41, 42]. When mixing MD and MC steps, we find that it is necessary to introduce an “exclusion radius”: Monte Carlo moves may accept to place particles very

close to each other, resulting in high energy states due to the short ranged repulsive interaction potentials. Although these high energy states are rare, they typically result in forces which are outside the stability window for the MD integration scheme which results in a broken simulation. One way to avoid this problem, is to modify the proposal probability: we do not propose MC moves which result in particles being placed very close to each other or “inside the exclusion radius”, typically  $0.9\sigma$ . On the other hand we also do not propose moves which remove particles which are within the exclusion radius. Thus, detailed balance is obeyed.

## Grand-canonical Monte Carlo

As outlined earlier, the grand-canonical partition function is given by equation (2.6):

$$\begin{aligned}
 \mathcal{Z}_G(\mu_1, \dots, \mu_z, V, T) &= \sum_{N_1=0}^{\infty} \cdots \sum_{N_z=0}^{\infty} Z(\{N_i\}, V, T) \exp\left(\beta \sum_{i=1}^z N_i \mu_i\right) \\
 &= \sum_{N_1=0}^{\infty} \cdots \sum_{N_z=0}^{\infty} \underbrace{\left( \prod_{i=1}^z \frac{\left(\frac{V}{\lambda_i^3}\right)^{N_i}}{N_i!} \right)}_{Z_{\text{kin}}(\{N_i\}, V, T)} \times \\
 &\quad \underbrace{\left( \prod_{i=1}^z \frac{1}{V^{N_i}} \int_{V^{N_i}} \exp\left[-\beta E_{\text{pot}}(\vec{r}_1^{N_1}, \dots, \vec{r}_z^{N_z})\right] d\vec{r}^{3N_1} \dots d\vec{r}^{3N_z} \right)}_{\Xi(\{N_i\}, V, T)} \times \\
 &\quad \exp\left(\beta \sum_{i=1}^z N_i \mu_i\right),
 \end{aligned}$$

Here we see that the probability of finding a certain set of particle numbers and a certain configuration  $k = \{N_i, \vec{r}^{N_i}\}$  is given by:

$$P_k = \frac{1}{\mathcal{Z}_G} Z_{\text{kin}}(\{N_i^k\}, V, T) e^{-\beta E_{\text{pot}, k} + \beta \sum_{i=1}^z N_i^k \mu_i}, \quad (2.59)$$

where  $Z_{\text{kin}}(\{N_i^k\}, V, T) = \frac{V^{N_i^k}}{N_i^k! \lambda_i^{3N_i^k}}$  is the kinetic canonical partition function of species  $i$  and where  $\mathcal{Z}_G = \sum_{N_i} Z(\{N_i\}, V, T) e^{\beta \mu_i N_i}$ . Similarly, we find the probability for a state  $j$ .

## 2 Theoretical Background

---

Therefore, the acceptance probability in a grand-canonical Monte Carlo simulation is:

$$\text{acc}_{k \rightarrow j} = \min \left( 1, \prod_i \left( \frac{V}{\lambda_i^3} \right)^{N_i(j) - N_i(k)} \frac{N_i(k)!}{N_i(j)!} e^{-\beta \Delta E_{\text{pot}} + \beta \sum_i \mu_i (N_i(j) - N_i(k))} \right), \quad (2.60)$$

where the products and sums run over all species  $i$ , which are exchanged with the reservoir in the attempted move.

For the insertion of two particles (e.g. a positive and a negative ion) at the same time, the corresponding acceptance probability is [43]:

$$\text{acc}_{\text{insertion}} = \min \left( 1, \frac{V^2}{\lambda_+^3 \lambda_-^3} \frac{1}{(N_- + 1)(N_+ + 1)} e^{\beta(\mu_+ + \mu_- - \Delta E_{\text{pot}})} \right).$$

We could apply this equation directly, however, if we want to simulate a reservoir with a *given salt concentration concentrations*, we do not (yet) know which chemical potentials  $\mu_+$ ,  $\mu_-$  represent this concentration. We circumvent this problem by inserting the definition of the chemical potential  $\mu_i = k_B T \ln(c_i \lambda_i^3) + \mu_i^{\text{ex}}$  and exploiting that the chemical potential in the reservoir and the simulated system are equal in the grand-canonical ensemble  $\mu_i = \mu_i^{\text{res}}$ . We obtain the following modified acceptance probability:

$$\text{acc}_{\text{insertion}} = \min \left( 1, V^2 c_+^{\text{res}} c_-^{\text{res}} \frac{1}{(N_- + 1)(N_+ + 1)} e^{\beta \mu_s^{\text{res,ex}}} e^{-\beta \Delta E_{\text{pot}}} \right). \quad (2.61)$$

It contains the reservoir concentrations  $c_+^{\text{res}}$  and  $c_-^{\text{res}}$  and the excess chemical potential of inserting an ion pair into the reservoir  $\mu_s^{\text{res,ex}}$ . It remains the problem to determine  $\mu_s^{\text{res,ex}}$ , which can be done with the Widom insertion method (see next section).

### Widom Insertion Method

The Widom insertion method is used to determine the excess chemical potential of species [18]. Determining the excess chemical potential is a task which we left open in Section 2.1.1.

The excess chemical potential is given by the partial derivative of the conformational free energy with respect to particle number and results in [18]<sup>6</sup>:

$$\begin{aligned}\mu_i^{\text{ex}} &= \frac{\partial F^{\text{conf}}(N_i, V, T)}{\partial N_i} = F^{\text{conf}}(N_i + 1, V, T) - F^{\text{conf}}(N_i, V, T) \\ &= -kT \ln \left( \frac{1}{V} \int_V d^3 r_{N_i+1} \langle \exp(-\beta \Delta E_{\text{pot}}) \rangle_N \right).\end{aligned}\tag{2.62}$$

In order to estimate the excess chemical potential with equation (2.62), we insert particles at random positions in the box and measure the associated change in potential energy [18]. Since these insertions are only temporary, the Widom insertion method is a Monte Carlo method that employs “virtual moves”, i.e. moves which are never accepted [44].

When the inserted particles carry a charge, it is important to keep the system electroneutral, or else the measured change in energy would be different. In the case of inserting a positive and a negative ion simultaneously, the corresponding formula for

---

<sup>6</sup>The formula for the excess chemical potential is different, if we want to determine it for a system simulated in the grand-canonical ensemble or the isothermal isobaric ensemble.

## 2 Theoretical Background

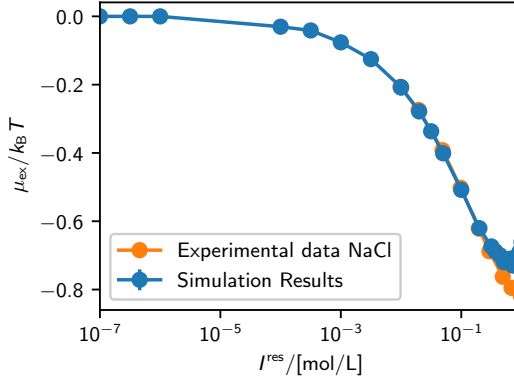


Figure 2.3: Linearly interpolated excess chemical potential  $\mu_s^{\text{res,ex}}$  for inserting a pair of ions as a function of ionic strength  $I = \frac{1}{2}(c_- + c_+) = c_+ = c_-$ . Error bars are smaller than symbol size. Orange points mark experimental results which are calculated from the activity coefficients  $\gamma_s = \exp(\mu_+^{\text{res,ex}} + \mu_-^{\text{res,ex}})$  provided by [45] and [46]. The deviations of the simulated data with the experimental data at high ionic strength are consistent within the simulation model.

the excess chemical potential is:

$$\mu_s^{\text{res,ex}} = -k_B T \ln \left( \frac{1}{V^2} \int_V \int_V d^3 r_{N+1} d^3 r_{N+2} \langle \exp(-\beta \Delta E_{\text{pot}}) \rangle_N \right), \quad (2.63)$$

We repeatedly need the excess chemical potential for simulating systems in contact with a reservoir of specific ionic concentration of monovalent ions. Therefore, we provide the data in figure 2.3. The simulations, yielding these data, were performed for systems containing 400 monovalent ion pairs (i.e. in total 800 ions) at temperature  $T = 300$  K, with  $\epsilon_r = 80$  and ions interacting with the WCA potential. By changing the volume of the simulation box, different ionic strengths were achieved.



**Note 4**

For an electroneutral reservoir, containing only ions with valency  $z_i = \pm 1$  and otherwise identical interactions, the excess chemical potential (needed to add one additional ion pair) only depends on the ionic strength  $I^{\text{res}} = \sum_i c_i^{\text{res}} z_i^2$ . In contrast, if our reservoirs contained particles with different interactions, e.g. additionally some multivalent ions or ions with different interaction potentials, then the excess chemical potential would depend on the exact reservoir composition  $c_1, c_2, \dots$ .

With the above insertion of a pair of ions, we can only determine the excess chemical potential of an ion pair. The single ion excess chemical potential cannot be determined because we cannot add a single ion and maintain the electroneutrality condition. The activity coefficient of the ion pair is:

$$\gamma_{\text{pair}} = \exp(\beta \mu_s^{\text{res,ex}}). \quad (2.64)$$

It is now convenient to define the mean activity coefficient  $\gamma_{\pm} = \sqrt{\gamma_{\text{pair}}}$  or equivalently the mean excess chemical potentials:

$$\mu_+^{\text{res,ex}} = \mu_-^{\text{res,ex}} = \mu_s^{\text{res,ex}}/2. \quad (2.65)$$

We make use of this mean activity coefficient in the definition of pH in Chapter 5.

### Reaction Ensemble Method

Since we are interested in modeling weak polyelectrolytes we need a simulation algorithm that is capable of simulating chemical equilibrium. Following the derivation by Heath et al. [19], a derivation of the reaction ensemble method is given. Using this simulation method, we can simulate arbitrary reactions, such as the one given in the general reaction equation (2.9).

The reaction ensemble method is a Monte Carlo method closely related to the grand-canonical ensemble [19, 47]. Restricting the particle number fluctuations in the grand-canonical ensemble to those which follow the stoichiometry of a chemical reaction, e.g. (2.9), we obtain the reaction ensemble. For transitioning from state  $k$  to a state  $l = \{N_i^k + \nu_{r,i}, \bar{r}^{N_i^k + \nu_{r,i}}\}$ , due to a chemical reaction  $r$  with stoichiometric coefficients  $\nu_{r,i}$ , we obtain (using equation (2.60)) [19]:

$$\begin{aligned} \text{acc}_{k \rightarrow l} &= \min \left( 1, \frac{P_l}{P_k} \right) \\ &= \min \left( 1, V^{\bar{\nu}} \prod_{i=1}^z \left( \lambda_i^{-3\nu_i} \left[ \frac{N_i^0!}{(N_i^0 + \nu_i)!} \right] e^{\beta \sum_i \nu_i \mu_i} \right) e^{-\beta \Delta E_{\text{pot}, k \rightarrow l}} \right), \end{aligned} \quad (2.66)$$

or via using the chemical equilibrium condition  $\Delta G = \sum_i \mu_i \nu_i = 0$

$$\text{acc}_{k \rightarrow l} = \min \left( 1, \Gamma V^{\bar{\nu}} \prod_{i=1}^z \left[ \frac{N_i^0!}{(N_i^0 + \nu_i)!} \right] e^{-\beta \Delta E_{\text{pot}, k \rightarrow l}} \right), \quad (2.67)$$

where

- $\lambda_i$  is the thermal de Broglie wave length of species  $i$

- $\Gamma = \prod_i \lambda_i^{-3\nu_i} := K \cdot (c^\ominus)^{\bar{\nu}}$  is proportional to the equilibrium constant  $K$
- $N_i$  denotes the number of particles of type  $i$
- $\Delta E_{\text{pot}, k \rightarrow l} = E_{\text{pot}, l} - E_{\text{pot}, k}$  is the potential energy difference between the states before ( $k$ ) and after ( $l$ ) the reaction attempt.
- $V$  stands for the volume of the system
- $\nu_i$  is the stoichiometric coefficient of the reacting species  $i$  in the chosen reaction
- $\bar{\nu} = \sum_i \nu_i$  denotes the total change of the number of molecules in the chosen reaction

Simulating in the reaction ensemble at constant volume involves the following steps [47, 19]:

1. Change the conformation with a canonical Monte Carlo algorithm or NVT molecular dynamics
2. Perform a reaction trial move:
  - a) Choose a reaction and a direction with uniform probability
  - b) Randomly select reactant particles, exchange the selected reactant particles with the corresponding product particles. If there are more product particles than there are reactant particles, create new product particles. If there is an excess of reactant particles, delete the excess

- c) Assign Maxwell-Boltzmann distributed velocities to newly created particles (important if MD moves are used for changing the configuration of the system)
3. Use the acceptance probability (2.67) to decide whether to accept the trial move or not. If the move is not accepted, restore the state of the system prior to the trial move
4. Repeat, starting from step one

### Constant pH Method

The work detailed in this section was published earlier in the following publication:

**J. Landsgesell**, C. Holm, J. Smiatek. "Simulation of weak polyelectrolytes: A comparison between the constant pH and the reaction ensemble method" In: *The European Physical Journal Special Topics* 226(725–736) (2017)

URL: <https://dx.doi.org/10.1140/epjst/e2016-60324-3>

The constant pH method is an alternative way of implementing chemical reactions in equilibrium in computer simulation. As before, we consider the special case of a weak acid which dissociates and which follows the chemical equation (2.16).

The partition sum of the constant pH ensemble is given by Reed and Reed [48] as a sum over all degrees of association  $\bar{n}$  and over

all corresponding configurational microstates  $i$  of the system:

$$Z_{\text{pH}} = \sum_{\bar{n}} \left( \frac{N_0}{(1 - \bar{n})N_0} \right) x^{N_0(1 - \bar{n})} \sum_{i(\bar{n})} \exp(-\beta E_{\text{pot}, i}), \quad (2.68)$$

where  $N_0$  is the number of titratable units and  $\bar{n} = 1 - \alpha = \frac{N_{\text{HA}}}{N_0}$  the degree of association. The individual probability for a microstate with a certain degree of association reads

$$p(\bar{n}, E_{\text{pot}, i}) = \left( \frac{N_0}{(1 - \bar{n})N_0} \right) x^{N_0(1 - \bar{n})} \exp(-\beta E_{\text{pot}, i}) \quad (2.69)$$

with  $x = 10^{\text{pH}_{\text{in}} - \text{pK}}$  where  $\text{pH}_{\text{in}}$  denotes the pH value and  $\text{pK}$  the negative decadic logarithm of the dissociation constant, which are both simulation input parameters. A deprotonation step for a single titratable group can be expressed by a change of the degree of association  $\Delta\bar{n} = 1/N_0$  in order to describe the transition from  $(\bar{n}, E_i)$  to  $(\bar{n} - \Delta\bar{n}, E_j)$ . The Metropolis acceptance probability [39] for this Monte Carlo move reads

$$\text{acc}_{\text{ass} \rightarrow \text{diss}} = \min \left( 1, \frac{p(\bar{n} - \Delta\bar{n}, E_{\text{pot}, j})}{p(\bar{n}, E_{\text{pot}, i})} \right) \quad (2.70)$$

which yields

$$\text{acc}_{\text{ass} \rightarrow \text{diss}} = \min \left( 1, \frac{\left( \frac{N_0}{(1 - \bar{n} + \Delta\bar{n})N_0} \right) x^{N_0\Delta\bar{n}} \exp(-\beta(E_{\text{pot}, j} - E_{\text{pot}, i}))}{\left( \frac{N_0}{(1 - \bar{n})N_0} \right)} \right) \quad (2.71)$$

after inserting Eqn. (2.69) into Eqn. (2.70). This expression can be reformulated for a single deprotonation step ( $\Delta\bar{n} = 1/N_0$ ) which

reads

$$\text{acc}_{\text{ass} \rightarrow \text{diss}} = \min \left( 1, \frac{\binom{N_0}{(1-\bar{n}+1/N_0)N_0}}{\binom{N_0}{(1-\bar{n})N_0}} x \exp(-\beta \Delta E_{\text{pot}}) \right) \quad (2.72)$$

with  $\Delta E_{\text{pot}} = E_{\text{pot},j} - E_{\text{pot},i}$ . By using the relation

$$\frac{\binom{N_0}{(1-\bar{n}+1/N_0)N_0}}{\binom{N_0}{(1-\bar{n})N_0}} = \frac{N_0 \bar{n}}{N_0(1-\bar{n})+1} \stackrel{N_0 \rightarrow \infty}{\sim} \frac{N_0 \bar{n}}{N_0(1-\bar{n})} = \frac{N_{\text{HA}}}{N_{\text{A}^-}} \quad (2.73)$$

in the thermodynamic limit of an infinite number of titrable groups  $N_0$ , we finally obtain a simple expression for the acceptance probability in the constant pH method with a symmetric dissociation proposal probability according to

$$\text{acc}_{\text{ass} \rightarrow \text{diss}} = \min \left( 1, \frac{N_{\text{HA}}}{N_{\text{A}^-}} 10^{\text{pH}_{\text{in}} - \text{p}K} \exp(-\beta \Delta E_{\text{pot}}) \right) \quad (2.74)$$

which can be equivalently formulated for a protonation or association reaction, respectively.

This formulation of the constant pH method is especially useful for a comparison with the reaction ensemble (which also uses symmetric proposal probabilities). We performed a direct comparison of the reaction ensemble and the constant pH ensemble in reference [4]. The key take away is that the implicit treatment of the protons gives serious deviations due to missing electrostatic screening at high and low pH.

### Note 5

In literature, the constant pH Monte Carlo method typi-

cally uses the asymmetric proposal probabilities  $g_{\text{diss} \rightarrow \text{ass}} = N_{\text{A}^-}/N_0$  for a protonation and  $g_{\text{ass} \rightarrow \text{diss}} = N_{\text{HA}}/N_0$  for a deprotonation, i.e.  $g_{\text{diss} \rightarrow \text{ass}} \neq g_{\text{ass} \rightarrow \text{diss}}$ . This choice of the proposal probabilities yields the Metropolis-Hastings acceptance probability to accept a trial move from state  $k$  to state  $l$ :

$$\text{acc}_{k \rightarrow l} = \min\left(1, e^{-\beta \Delta E_{\text{pot}}} 10^{\mp(\text{pH}_{\text{in}} - \text{pK})}\right), \quad (2.75)$$

where  $\Delta E_{\text{pot}} = E_{\text{pot},l} - E_{\text{pot},k}$  is the change in the potential energy due to the exchange of chemical species,  $\text{pH}_{\text{in}}$  is an input parameter and determines the underlying implicit pH value, and  $\text{pK}$  is the negative common logarithm of the dissociation equilibrium constant, which is also a simulation parameter. A positive sign is used for a deprotonation reaction (diss) and a negative sign for a protonation reaction (ass) [48, 49, 50, 51, 52, 53].

## 2.5.4 General Simulation Protocol

All particle-based simulations in this thesis are performed using the simulation package ESPResSo [54]. We use reduced units in order to improve numerical stability of the algorithms and the mapping of reduced units to the international system of units (SI) is given in table 2.1.

The particles which we want to represent have a diameter around  $0.355 \text{ nm} = 1\sigma$ . Therefore, we choose our Weeks-Chandler-Andersen (WCA) potential to have the effective particle size  $\sigma = 0.355 \text{ nm}$  and interaction strength  $\epsilon = 1.0 k_{\text{B}}T$ . FENE bonds connect the neighbouring monomers [55], using the typical Kremer-Grest parameters [36]  $k_{\text{FENE}} = 30.0 k_{\text{B}}T/\sigma^2$  and  $R_{\text{max}} =$

## 2 Theoretical Background

| Reduced units and SI values |  |
|-----------------------------|--|
| Basic length                | $\sigma = 0.355 \text{ nm}$                          |
| Basic energy                | $\epsilon = 1 k_B T$                                 |
| Thermal energy              | $1 k_B T = 300 \text{ K} k_B$                        |
| Bjerrum length              | $\lambda_B = 2 \sigma = 0.71 \text{ nm (for water)}$ |
| Mass                        | $m = 1 \text{ (arbitrary, see Section 3.4)}$         |

Table 2.1: Mapping of reduced units used in this dissertation to the international system of units.

$1.5\sigma$  (unless noted otherwise). The Bjerrum length is that of water at roughly  $T = 300 \text{ K}$  (corresponding to  $\epsilon_r = 80$ ):

$$\lambda_B = \frac{1}{4\pi\epsilon_0\epsilon_r} \frac{e_0^2}{k_B T} = 0.71 \text{ nm} = 2\sigma. \quad (2.76)$$

In reduced units we choose the thermal energy  $k_B T = 1\epsilon$  (with  $\epsilon$  the basic simulation unit of energy) and the elementary charge to be  $e_0 = 1q^*$  (with  $q^*$  the basic simulation unit of charge). Temperature is accounted for, using a Langevin thermostat for MD, or in the MC acceptance criteria. Electrostatic interactions are calculated using the P3M method [56] tuned to a maximal pairwise error in electrostatic force of  $10^{-3} k_B T / \sigma$  [57].

As shown for the canonical ensemble in Section 2.1, the ensemble averages of all observables  $\mathcal{A}(\vec{r}^N)$ , that only depend on the particle positions, are independent of the particle mass. Similar arguments also hold for the (semi-)grand-canonical ensemble. Therefore, we do not define a time or mass scale in our systems. The particle mass affects how fast the equilibration takes place, but not the equilibrium itself.



## 2.6 Polymer Physics

As outlined in the introduction in Chapter 1, polyelectrolytes are ubiquitous in biological systems and chemical applications. Common to all polymers is the fact, that they are made up of smaller repeating units connected to chains. Crosslinking these polymer chains yields polymer gels. Common to all polymeric systems is that they are strongly influenced by the interactions in the system. Therefore, polyelectrolyte systems typically react to “external” changes in:

- the temperature
- the solvent
- the pH
- the salt concentration
- the presence of specific ions (e.g. chelation with multivalent ions)

Additionally, their behavior also depends on “internal” properties such as

- the dissociation constant in the case of weak polyelectrolytes, or the charge fraction in the case of strong polyelectrolytes
- the polydispersity of the chain length distribution in the polymer solution or gel

The above listing illustrates the large parameter space one needs to investigate for polyelectrolyte systems.

One main idea followed throughout this thesis is that the complicated behavior of a polymer gel can be described by the behavior of single chains in appropriate geometries. Therefore, we present some properties of linear polymers in this section. For more details we refer the reader to common polymer textbooks such as references [58, 59].

### 2.6.1 Freely Jointed Chain

An ideal chain (also known as a freely jointed chain or a Gaussian polymer) is the simplest polymer model. The monomers are bonded with fixed bond length  $b$ , and do not interact with each other. For a chain containing  $N$  monomers, the maximal extension is, therefore,  $R_{\max} = (N - 1)b$ .

In general the end-to-end vector of a polymer is given by the connection vector of the first and last monomer.

$$\vec{R}_e = \vec{r}_N - \vec{r}_1 = \sum_{i=1}^N \vec{b}_i, \quad (2.77)$$

where  $\vec{b}_i$  is the  $i$ -th bond vector. For an ideal chain there is no correlation in the bond-vectors, i.e.  $\langle \vec{b}_i \vec{b}_j \rangle = b^2 \delta_{i,j}$ . Therefore, the mean squared end-to-end distance is

$$\langle R_e^2 \rangle = \sum_{i=1}^N \sum_{j=1}^N \langle \vec{b}_i \vec{b}_j \rangle = Nb^2 \Leftrightarrow R_e := \sqrt{\langle R_e^2 \rangle} \propto N^{0.5}, \quad (2.78)$$

where  $\nu = 0.5$  is the Flory exponent of the ideal chain. For a chain with excluded volume interactions we have an altered [60] Flory exponent  $\nu = 0.588$ , and in poor solvent conditions we obtain  $\nu = 0.33$ .

The force needed to separate both ends by a certain distance  $R_e$  is given by the force-extension curve. The force extension curve of a freely jointed chain can be obtained by considering the configurational partition function of the chain. For details, we refer to [58, p. 76]. The resulting force-extension curve  $f$  is given by:

$$f(R_e) = -\frac{k_B T}{b} \mathcal{L}^{-1}\left(\frac{R_e}{b(N-1)}\right), \quad (2.79)$$

where  $\mathcal{L}^{-1}$  is the inverse Langevin function. We make use of this result later in Chapter 3.

## 2.6.2 Gel Models

In this chapter four different models are presented which are commonly used to predict gel swelling:

- the Donnan model (mainly for ion partitioning) [61]
- the Flory-Rehner model [62]
- the Katchalsky model [3, 63]
- the molecular dynamics model of a periodic gel [3, 64, 65, 66, 67, 68, 69, 70, 71, 72, 73, 74, 75, 76]

All four models can be used to describe the swelling of a gel when it is in contact with a supernatant salt solution. Typically,

these models are used to investigate the behavior of strong polyelectrolyte gels in contact with a pH neutral salt solution: For pH=7,  $H^+$  and  $OH^-$  ions can be safely neglected and the supernatant solution is fully described by the salt concentration  $c_{\text{salt}}^{\text{res}}$ . In chapters 5 and 6 we go beyond studying strong polyelectrolyte gels and investigate polymer systems which are in contact with a solution which is not pH neutral.

### Donnan Model

The Donnan Model is the simplest model for determining the partitioning of ions between an infinite reservoir and a system containing a macroion and its counterions. In this model we treat all particles on the level of an ideal gas.

**Ion Partitioning:** The ion partitioning is determined based on, first, the electroneutrality constraint for the gel system

$$\sum_i c_i^{\text{gel}} z_i = 0, \quad (2.80)$$

where  $z_i$  is the valency and  $c_i^{\text{gel}}$  the concentration of particle species  $i$  in the gel and, second, the equality of all electrochemical potentials

$$\bar{\mu}_i^{\text{gel}} = \bar{\mu}_i^{\text{res}}. \quad (2.81)$$

The (electro-)chemical potential is defined as[23]:

$$\bar{\mu}_i = \mu_i^\ominus + k_B T \ln(c_i/c^\ominus) + z_i e_0 \psi. \quad (2.82)$$

Consider a simple macroion with charge fraction  $\alpha$  and concen-

tration  $c_0$ . Let the macroion be negative so that the counterions have species  $i = +$ . For a simple reservoir at pH = 7 the reservoir contains only  $i = +$  and  $i = -$  ions and the concentrations inside the gel and outside the gel satisfy:

$$\bar{\mu}_i^{\text{gel}} = \bar{\mu}_i^{\text{res}} \Leftrightarrow \frac{z_i e_0}{k_B T} (\psi^{\text{res}} - \psi^{\text{gel}}) = \ln \left( \frac{c_i^{\text{gel}}}{c_i^{\text{res}}} \right),$$

or equivalently  $\exp \left( \frac{e_0}{k_B T} (\psi^{\text{res}} - \psi^{\text{gel}}) \right) = \frac{c_+^{\text{gel}}}{c_+^{\text{res}}} = \frac{c_-^{\text{res}}}{c_-^{\text{gel}}}$ . Inserting the last equation into the electroneutrality condition (2.80) gives:

$$\alpha c_0 + c_-^{\text{gel}} = c_+^{\text{gel}} \implies \alpha c_0 + c_-^{\text{gel}} = \frac{c_-^{\text{res}} c_+^{\text{res}}}{c_-^{\text{gel}}},$$

This is the well known Donnan-partitioning [77]

$$c_-^{\text{gel}} = \frac{-\alpha c_0 + \sqrt{(\alpha c_0)^2 + 4 c_-^{\text{res}} c_+^{\text{res}}}}{2} \neq c_-^{\text{res}}. \quad (2.83)$$

For ion concentrations  $c_i^{\text{gel}} \neq c_i^{\text{res}}$  the equality of the electrochemical potential  $\bar{\mu}_i^{\text{gel}} = \bar{\mu}_i^{\text{res}}$  results in the Donnan potential  $\Delta\psi$ :

$$\Delta\psi := \psi^{\text{res}} - \psi^{\text{gel}} = \frac{k_B T}{z_i e_0} \ln(c_i^{\text{gel}}/c_i^{\text{res}}). \quad (2.84)$$

This potential is also known as the Nernst potential.

**Gel Swelling:** The Donnan model above captures the “ideal” aspects of ion partitioning by enforcing chemical potential equilibrium. For the free swelling equilibrium of polyelectrolyte gels, we have to additionally prescribe mechanical equilibrium. In mechanical equilibrium we find that the pressures at the interface

## 2 Theoretical Background

---

are equal:

$$p^{\text{gel}} = P^{\text{res}}, \quad (2.85)$$

where  $p^{\text{gel}}$  is the pressure inside the gel and  $P^{\text{res}}$  the pressure in the reservoir.

The reservoir pressure is given by (compare equation (2.2)):

$$P^{\text{res}} = -\frac{\partial F^{\text{res}}}{\partial V} = -\underbrace{\frac{\partial F_{\text{id}}}{\partial V}}_{p_{\text{id}}^{\text{res}}} - \underbrace{\frac{\partial F_{\text{conf}}}{\partial V}}_{p_{\text{ex}}^{\text{res}}} \quad (2.86)$$

In the ideal Donnan model the conformational pressure contribution  $P_{\text{ex}}^{\text{res}}$  is not present because we consider ideal gases only.

The pressure of the gel is not yet specified. Clearly it contains the kinetic pressure of the mobile ions in the gel:  $p_{\text{id}}^{\text{gel}} = k_{\text{B}}T \sum_i c_i^{\text{gel}}$ . This pressure contribution is purely repulsive. In order to model the stretching of polymers, we additionally include a stretching term:

$$p_{\text{str}}^{\text{gel}} = -\frac{\partial F_{\text{str}}}{\partial V} = -\frac{\partial F_{\text{str}}}{\partial R_{\text{e}}} \frac{\partial R_{\text{e}}}{\partial V} \quad (2.87)$$

The introduction of the stretching term requires some assumptions:

1. an assumption about the form of the stretching free energy  $F_{\text{str}}$ , or alternatively a force extension curve for the gel  $-\frac{\partial F_{\text{str}}}{\partial R_{\text{e}}}$ . For simplicity, we supply the force extension curve of a freely jointed chain:  $-\frac{\partial F_{\text{str}}}{\partial R_{\text{e}}} = -\frac{k_{\text{B}}T}{b} \mathcal{L}^{-1}\left(\frac{R_{\text{e}}}{(N-1)b}\right)$ , where  $N$  is the number of monomers per chain,  $b$  the bond length and  $k_{\text{B}}T$  proportional to the absolute temperature. For small chain extensions  $R_{\text{e}}$  this force extension curve can be

approximated by:  $-\frac{\partial F_{\text{str}}}{\partial R_e} \approx -k_B T \frac{3R_e}{Nb^2}$

2. an assumption about the deformation of the gel. We make the ansatz  $V = \frac{N}{c_m} = R_e^3/A \implies \frac{\partial V}{\partial R_e} = \frac{3R_e^2}{A}$ , where  $A$  is a constant. This ansatz is motivated later in Section 3.2.

Using these two assumptions (like Richter [1, p. 35]) we obtain the following stretching pressure:

$$p_{\text{str}}^{\text{gel}} = -\frac{k_B T}{b} \mathcal{L}^{-1} \left( \frac{R_e}{(N-1)b} \right) \frac{A}{3R_e^2} \approx -k_B T \frac{1}{Nb^2} \frac{A}{R_e}. \quad (2.88)$$

Finally, we can equate the gel pressure (which depends on the gel volume) and the reservoir pressure:

$$p^{\text{gel}}(V^{\text{gel}}) = p_{\text{id}}^{\text{gel}}(V^{\text{gel}}) + p_{\text{str}}^{\text{gel}}(V^{\text{gel}}) \stackrel{!}{=} p^{\text{res}}. \quad (2.89)$$

The volume  $V^{\text{gel}}$ , which satisfies the above equation, is called the equilibrium volume of the gel  $V_{\text{gel}}$ . This is the simplest model on gel swelling and contains the main aspects of all other investigated models:

- Chemical potential equilibrium
- Mechanical equilibrium

The reason for investigating further models is that the model predictions are not satisfactory, as it was shown by Richter [1]. Therefore, we investigate more complicated models in the following.

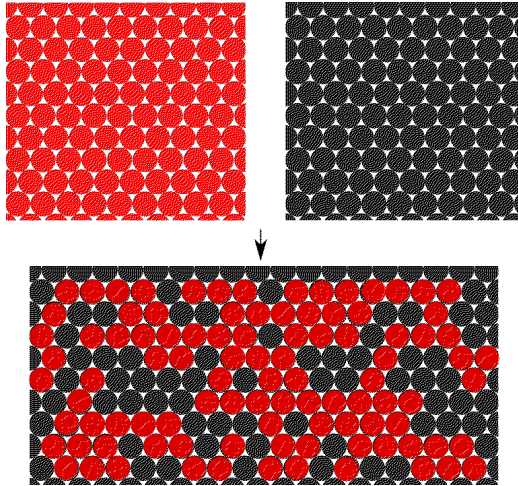


Figure 2.4: This scheme shows the mixing process of molecules *A* and *B* modeled in the Flory-Huggins model.

### Flory-Huggins / Flory-Rehner Models

The Flory-Huggins model is a lattice model used for predicting the change of free energy due to mixing of polymers with solvents [58, p. 138 ff.]. The Flory-Huggins mixing free energy is commonly, used in Flory-Rehner theories used to explain the swelling behavior of polymer systems [13].

**Flory-Huggins Model** The basic idea of this model is that the swelling of a polymer gel in a solvent can be understood as a mixing process of solvent and polymer. Let us consider two lattice systems (compare figure 2.4): In the first system all  $N_B$  lattice sites are occupied by solvent molecules of type *B*. In the second system all  $N_A$  lattice sites are occupied by monomers of type *A*. The mixed system then has  $N_A + N_B = n$  lattice sites



and the fraction of occupied lattice sites for species  $i$  is  $\phi_i = \frac{N_i}{n}$ . Mixing the initial systems, results in a change in free energy  $\Delta F_{\text{mix}} = \Delta U_{\text{mix}} - T\Delta S_{\text{mix}}$  which has an entropic and an inner energetic contribution.

The entropy of a lattice system is  $S = k_B \ln(\Omega)$ , where  $\Omega$  is the number of possible states (where we can not distinguish interchangeable, identical molecules). Therefore, the entropy of a system where all lattice sites are occupied by the same particles is  $S = k_B \ln(\Omega)$ , where there is only one possible state  $\Omega = 1$  because we cannot differentiate between identical particles. Therefore, the entropy is  $S = 0$  for the two unmixed lattice systems. The number of states in the mixed system is  $\Omega = (N_A + N_B)! / (N_A! N_B!)$  where the division accounts for the fact that we cannot distinguish identical particles. Therefore, we obtain the mixing entropy:

$$\begin{aligned} \Delta S_{\text{mix}} &= k_B \ln(\Omega) = k_B (\ln((N_A + N_B)!) - \ln(N_A!) - \ln(N_B!)) \\ &\approx -k_B n \left( \frac{N_A}{n} \ln \left( \frac{N_A}{n} \right) + \frac{N_B}{n} \ln \left( \frac{N_B}{n} \right) \right), \end{aligned} \quad (2.90)$$

where we used Stirling's approximation  $\ln m! = \sum_{k=1}^m \ln(k) \approx \int_1^m \ln(k) dk \approx m \ln m - m$ . Introducing the volume fractions  $\phi_i = \frac{N_i}{n}$ , we can rewrite this equation as following:

$$\Delta S_{\text{mix}} = -k_B n \left( \phi_A \ln(\phi_A) + \phi_B \ln(\phi_B) \right). \quad (2.91)$$

The mixing entropy for a polymer with chain length  $N$  is obtained from "modeling of the chain configurations by a random walk

## 2 Theoretical Background

---

without immediate self-reversal" [78, p. 61-65]:

$$\Delta S_{\text{mix}} = -k_B n \left( \frac{\phi_A}{N} \ln(\phi_A) + \phi_B \ln(\phi_B) \right) > 0, \quad (2.92)$$

where  $n$  is the number of lattice sites and  $N$  is the chain length of the polymer,  $\phi_A$  is the volume fraction of the monomers of type  $A$  and  $\phi_B$  is the volume fraction of the solvent. Connecting monomers to chains reduces the entropy of the system greatly, which is reflected in equation (2.92). [58, p. 140]. In general, the mixing entropy favors mixing. The change of internal energy upon mixing is:

$$\Delta U_{\text{mix}} = n\phi_A\phi_B\chi, \quad (2.93)$$

with the dimensionless Flory interaction parameter:

$$\chi = \frac{z}{2} \frac{2u_{AB} - u_{AA} - u_{BB}}{k_B T}, \quad (2.94)$$

which describes the nearest-neighbor interactions  $u_{i,j}$  between the  $A$  and  $B$  lattice sites, where  $z$  is the number of neighbors per lattice site. If  $\chi > 0$ , then the mixing process is energetically favorable. If  $\chi$  is smaller than zero, then mixing is energetically unfavorable and phase separations may occur. In total, we obtain the (Helmholtz) free energy of mixing:

$$\Delta F_{\text{mix}} = \Delta U_{\text{mix}} - T\Delta S_{\text{mix}} = n\phi_A\phi_B\chi + k_B T n \left[ \frac{\phi_A}{N} \ln(\phi_A) + \phi_B \ln(\phi_B) \right] \quad (2.95)$$

Using  $\phi_A =: \phi$  and  $\phi_B = 1 - \phi_A$ , we get the Flory-Huggins

equation for polymer solutions [58]:

$$\Delta F_{\text{mix}} = k_B T n \left( \frac{\phi}{N} \ln(\phi) + (1 - \phi) \ln(1 - \phi) + \chi(T) \phi(1 - \phi) \right), \quad (2.96)$$

If the free energy  $\Delta F_{\text{mix}}(\phi)$  has two minima (due to the internal energetic contribution  $\Delta U_{\text{mix}}$ ) phase separation can occur.

The mean-field Flory-Huggins theory is very effective in describing the miscibility of polymers in a solvent because the  $\chi$  parameter is an effective fitting parameter that contains “everything which is not understood about the thermodynamics” of the polymer system. Fitting  $\chi$  to experiments, it is found that it varies with composition and temperature [58, p. 167].

**Flory-Rehner Model:** Hydrogels can be described using the Flory-Rehner theory [13]. The free energy upon swelling is given by the mixing free energy contribution  $\Delta F_{\text{mix}}$  (see above) and a stretching free energy contribution  $\Delta F_{\text{str}}$ :

$$\Delta F^{\text{gel}} = \Delta F_{\text{mix}} + \Delta F_{\text{str}}. \quad (2.97)$$

Additionally, if there are some ionic species, the free energy change is complemented through an ionic contribution  $\Delta F_{\text{ions}}$ :

$$\Delta F^{\text{gel}} = \Delta F_{\text{mix}} + \Delta F_{\text{str}} + \Delta F_{\text{ions}} \quad (2.98)$$

Swelling equilibrium is found, where the thermodynamic pressure of the gel and the solution are equal:

$$-\frac{\partial F^{\text{gel}}}{\partial V} = P^{\text{res}}. \quad (2.99)$$

These theories are quite successful in describing experimental results due to the free fitting parameter  $\chi$ .

### Katchalsky Model

The Katchalsky model is also based on an expression for the free energy, with a stretching contribution  $F_{\text{str}}$ , a contribution for the ions  $F_{\text{ions}}$  and one for the electrostatic interaction energy  $F_{\text{el}}$  (on the level of the Debye-Hückel approximation) [63]:

$$F^{\text{gel}} = F_{\text{str}} + F_{\text{ions}} + F_{\text{el}}$$

The free energy contributions are given in more detail in [1]. Because we do not work with the free energies, we do not provide them here. Instead, we directly provide the pressure  $p^{\text{gel}} = -\partial F^{\text{gel}}/\partial V$  (i.e. the volume derivative) taken from [1].

In the Katchalsky model, the volumes and the end-to-end distances are connected through  $V(R_e) = R_e^3/A$ . The pressure in the Katchalsky model is then calculated according to

$$p^{\text{gel}} = -\frac{\partial F^{\text{gel}}}{\partial V} = p_{\text{str}}^{\text{gel}} + p_{\text{ions}}^{\text{gel}} + p_{\text{el}}^{\text{gel}}, \quad (2.100)$$

yielding [1]:

$$\begin{aligned} p_{\text{el}} &= -k_{\text{B}}T \frac{c_0}{N} \frac{(fN)^2 \lambda_{\text{B}}}{3R_e} \left[ \frac{5}{2} \frac{\xi}{(1+\xi)} - \ln(1+\xi) \right], \\ p_{\text{str}} &= -k_{\text{B}}T \frac{c_0 R_e}{3b(N-1)} \left( \mathcal{L}^{-1} \left( \frac{R_e}{b(N-1)} \right) - \mathcal{L}^{-1} \left( \frac{R_0}{b(N-1)} \right) \right), \\ p_{\text{ions}}^{\text{gel}} - p_{\text{ions}}^{\text{res}} &= k_{\text{B}}T \left( 2c_{\text{salt}}^{\text{gel}} + fc_0 - 2c_{\text{salt}}^{\text{res}} \right) \end{aligned} \quad (2.101)$$

where  $R_0 = 1.2N^{0.588}$  is the equilibrium end-to-end distance of a neutral chain of chain length[1]  $N$ . Additionally, the following variables were introduced:

$$\xi = 6V^{\frac{1}{3}}/(R_0\lambda_D^{-1}V(R_0)^{1/3}), \quad (2.102)$$

which depends on the inverse Debye screening length, given by

$$\lambda_D^{-1} = \sqrt{4\pi\lambda_B V(R_e)^{-1} \sum_i z_i N_i}.$$

The swelling equilibrium is found where the pressure in the gel equals the pressure of the reservoir:

$$p^{\text{gel}} = \underbrace{p_{\text{ext}}^{\text{res}} + p_{\text{ions}}^{\text{res}}}_{p^{\text{res}}} \Leftrightarrow p_{\text{el}}^{\text{gel}} + p_{\text{str}}^{\text{gel}} + (p_{\text{ions}}^{\text{gel}} - p_{\text{ions}}^{\text{res}}) = p_{\text{ext}}^{\text{res}} \quad (2.103)$$

In free swelling equilibrium we do not apply additional pressure to the reservoir ( $p_{\text{ext}}^{\text{res}} = 0$ ).

It is evident from the formulas (2.101) that the pressure contributions and the swelling equilibrium depend on the salt partitioning between the inside and the outside of the gel. It is determined solving the following two equations self-consistently [3]:

$$c_{\text{salt}}^{\text{gel}} = \sqrt{\left(\frac{fc_0}{2}\right)^2 + (c_{\text{salt}}^{\text{res}})^2} C - \frac{fc_0}{2}, \quad (2.104)$$

$$C = \exp\left(\frac{c_0}{2(c_{\text{salt}}^{\text{gel}} + fc_m)} \frac{6f^2 N \lambda_B}{\lambda_D^{-1} R_0^2 (1 + \xi)}\right), \quad (2.105)$$

where for  $C = 1$  the Donnan salt partitioning (see equation (2.83))

is obtained, which is chosen as initial guess for solving these two equations.

### Periodic Gel Model

We use molecular dynamics (MD) simulations to model periodically connected tetrafunctional strong polyelectrolyte gels on a coarse-grained level. Bonds are modeled via FENE bonds with Kremer-Grest parameters (see section 2.5.4). The solvent is implicitly modeled via choosing a corresponding value for the electrostatic permittivity  $\epsilon_r$ .

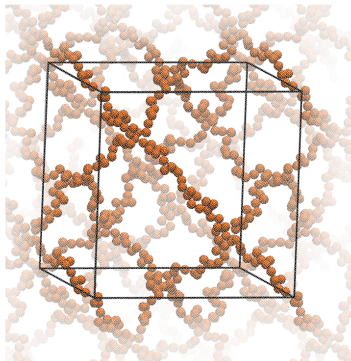


Figure 2.5: Illustration of the unit cell of the periodic gel model.

We simulate a cubic unit cell of a tetrafunctional gel. The unit cell contains 16 chains and 8 nodes, i.e. in total  $16N + 8$  gel monomers. An example snapshot of a periodic gel can be seen in figure 2.5. All MD simulations are performed using the MD simulation package ESPResSo [54]. Simulations of a periodic gel are performed in full analogy to the setup described

by Košován [3]. The number of monomers per chain in our simulation varies:  $N \in \{40, 64, 80\}$ .

For each simulation the volume and ensemble averaged virial pressure inside the gel is recorded yielding a pressure-volume (PV) curve. The Coulomb part of the pressure is calculated as described by [79]. The simulations are performed in a semi-grand-canonical ensemble [80], where salt and counterions are allowed to enter and leave the gel. The exchange of salt ions is performed by inserting pairs of salt ions. The acceptance probability for the insertion of one positive and one negative ion is [18]:

$$\text{acc}_{\text{insertion}} = \min \left( 1, V^2 c_+^{\text{res}} c_-^{\text{res}} \frac{1}{(N_- + 1)(N_+ + 1)} e^{\beta \mu_s^{\text{res,ex}}} e^{-\beta \Delta E_{\text{pot}}} \right), \quad (2.106)$$

with  $\beta = \frac{1}{k_B T}$  and  $\Delta E_{\text{pot}}$  the potential energy change due to the Monte Carlo move.  $N_i$  is the number of ions of species  $i$  in the simulation volume  $V$  and  $c_i^{\text{res}}$  is the concentration of species  $i$  in the reservoir. The semi-grand canonical simulation makes use of the pair excess chemical potential in the reservoir  $\mu_s^{\text{res,ex}} = \mu_+^{\text{res,ex}} + \mu_-^{\text{res,ex}}$  for inserting a positive ( $i = +$ ) and a negative ion ( $i = -$ ) at the same time (see Section 2.5.3) so that electroneutrality is satisfied at any time. The pair excess chemical potential is calculated in independent simulations of the reservoir (at different but fixed  $c_{\text{salt}}^{\text{res}}$ ) via the Widom insertion method [18] (see figure 2.3).





---

## 3 Improved Gel Models: Cell-Gel Models

The work detailed in this chapter was published earlier. These results are part of the following publications:

**J. Landsgesell**, C. Holm. “Cell Model Approaches for Predicting the Swelling and Mechanical Properties of Polyelectrolyte Gels” In: *Macromolecules* (2019)

URL: <https://doi.org/10.1021/acs.macromol.9b01216>

**J. Landsgesell**, S. Sean, P. Kreissl, K. Szuttor, C. Holm. “Modeling Gel Swelling Equilibrium in the Mean Field: From Explicit to Poisson-Boltzmann Models” In: *Physical Review Letters* 122(208002) (2019)

URL: <https://dx.doi.org/10.1103/PhysRevLett.122.208002>

Polyelectrolyte gels show a large, reversible uptake of water that is exploited in numerous applications. Tailoring polyelectrolyte gels to their applications requires a sufficiently accurate prediction of their swelling capabilities and elastic responses, a task that still goes beyond analytical approaches [81, 63, 82, 83, 84, 68, 85, 86, 87]. Coarse-grained polyelectrolyte network models have demonstrated their ability to amend analytical approaches, showing that structural microscopic details

can have noticeable effects on the macroscopic properties such as the swelling [64, 88, 65, 89, 70, 71, 66, 73, 3, 90]. Macroscopic gels with monodisperse chain length can be simulated with microscopic detail using molecular dynamics (MD) simulations with periodic boundary conditions (PBCs) (cf. *periodic gel model*) where a unit gel section is connected periodically to yield an infinite gel without boundaries. These expensive coarse-grained simulations provide predictions about mechanical and swelling properties of macroscopic gels and revealed insights into the validity of various analytical predictions. However, some features of real gels like polydispersity are hard to include in such models. To represent polydispersity faithfully, one would have to simulate a huge volume element with many chains of different length and a sufficiently large number of realizations. Huge particle-based simulations with more than  $10^5$  monomers have been performed for investigating polydispersity in uncharged networks by [91] and [92]. To our knowledge, the only simulation study that treats polydispersity in charged polymer gels is that of Edgecombe [93]. Due to the computational cost of simulations with explicit charges Edgecombe et al. are only able to simulate gels with  $10^2$  monomers [93]. With this setup the polyelectrolyte chains are highly correlated since the small unit cell is periodically repeated. We compare the results obtained by Edgecombe qualitatively to a simple extension of our models. Additionally, even MD simulations of periodic gels remain computationally very expensive due to the many particles and the slow relaxation times of the involved polymers.

Thus, the development of computationally efficient mean-field models capable of predicting swelling equilibria have been of scientific interest in the last years [94, 68, 3, 90]. The Katchalsky

---

model [63, 3, 1] (compare Section 2.6.2) is an established mean-field model shown to predict swelling equilibria reasonably well [3] when compared to MD simulations of charged bead-spring gels. However, the Katchalsky model fails [3] for Manning parameters  $\xi = \lambda_B / \langle d \rangle > 1$  [95], where  $\lambda_B$  denotes the Bjerrum length, and  $\langle d \rangle$  the average distance between polymer backbone charges. This is presumably due to the usage of the Debye-Hückel approximation. First ideas of using a Poisson-Boltzmann (PB) cell model under tension were put forward by Mann for salt-free gels, with moderate success [94].

In this chapter we describe two successive mean-field models to render the determination of swelling equilibria of polyelectrolytes accurately and efficiently. Figure 3.1 displays our construction scheme of the two different models. First, we describe a *single-chain MD cell model*, that reproduces results similar to those obtained from expensive periodic gel MD simulations. This reduces the many-body problem of the periodic gel to one of computing the pressure exerted within a cell containing a single polyelectrolyte chain. The single-chain cell model can thus be viewed as a mean-field attempt to factorize the many-body partition function of the macrogel into a product state of suitable identical subunits [24]. We then show that the single-chain cell model can further be simplified in a second mean-field step using a PB description of the chain with appropriate boundary conditions. The PB cell description has been successful in describing a variety of polyelectrolyte phenomena [96, 97, 98, 27, 99, 100] and is here applied to macroscopic polyelectrolyte gels for the first time. The quality of our two mean-field models is gauged by comparing them to 60 data points for the swelling equilibrium of periodic monodisperse gel MD simulations obtained within a

### 3 Improved Gel Models: Cell-Gel Models

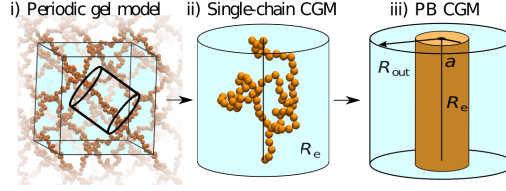


Figure 3.1: A schematic of the i) macroscopic gel; ii) single-chain cell-gel model (CGM); and iii) PB CGM of a macroscopic gel, which are in equilibrium with a salt reservoir. The symbols are introduced in the text.

wide range of system parameters.

In our models, the polymer chains are characterized by the number of monomers  $N$  per chain, and the charge fraction per monomer  $f \in [0, 1]$ . The reservoir, on the other hand, is characterized by the salt concentration  $c_{\text{salt}}^{\text{res}}$ , which is related to the reservoir concentrations of positive and negative ions  $c_{\text{salt}}^{\text{res}} = c_+^{\text{res}} = c_-^{\text{res}}$  ensuring electroneutrality.

Two important features of all models i–iii) that deserve to be highlighted, are the following two equilibrium conditions [82, 101]: First, the chemical potentials for all reservoir particle species  $i$  are constant (in the following, we use species  $i \in \{+, -\}$ ). Therefore, the chemical potentials (of each species  $i$ ) in the gel ( $\mu_i^{\text{gel}}$ ) and in the reservoir ( $\mu_i^{\text{res}}$ ) are equal:

$$\mu_i^{\text{gel}} = \mu_i^{\text{res}}. \quad (3.1)$$

Second, there has to be mechanical equilibrium, dictating that the pressure of the gel ( $P_{\text{in}}$ ) has to balance the pressure exerted

on the system by the reservoir ( $P_{\text{res}}$ ):

$$P_{\text{in}}(V_{\text{eq}}) = P_{\text{res}}. \quad (3.2)$$

In all models we approximate the reservoir pressure by the pressure of an ideal gas  $P_{\text{res}} \approx k_{\text{B}}T \sum_i c_i^{\text{res}}$  (unless specified otherwise). The gel, while in contact with a reservoir, is simulated at different volumes and the equilibrium volume  $V_{\text{eq}}$  is determined by eq. (3.2). In mechanical and chemical equilibrium the end-to-end distance is the equilibrium chain extension  $R_{\text{eq}}$ .

## 3.1 Periodic Gel Model

The periodic gel simulations are performed as described in Section 2.6.2. All periodic gel data in this thesis stem from simulations performed explicitly for this thesis with interaction parameters as discussed in Section 2.5.4.

We could not use the periodic gel data from Richter [3, 1] because the simulations by Richter were performed using FENE bonds with a spring constant  $k_{\text{FENE}} = 10k_{\text{B}}T/\sigma^2$ . For FENE bonds with such a low spring constant, the average bond length  $b$  depends on the stretching state of the gel, i.e.  $b(R_{\text{e}})$ . A varying bond length is a complication we want to avoid in our models. Additionally, Richter et al. [3, 1] employed a flawed grand-canonical scheme: when a particle was inserted very close to another particle (i.e. in a high energy configuration due to the short ranged repulsive interactions), the trial move was repeated until the particle was inserted in the simulation box without particle overlap — this leads to wrong statistics. Instead, the Monte

Carlo simulation should have rejected this trial move (according to the acceptance probability) due to a particle overlap and the corresponding high energy. A correct implementation would not have repeatedly attempted to insert the particle until a non-overlapping configuration was found.

## 3.2 Single-Chain Models

In contrast to the previously discussed expensive MD simulations of periodic gels, we proposed a reduction of the many-chain problem to a single-chain problem in our recent publication [102]. In this section we describe common features of the (particle-based) single-chain CGM and the PB CGM.

Using simple geometric considerations, it is found, that for a fully stretched tetrafunctional, monodisperse gel the volume  $V_{\text{chain}}$ , which is associated to a single-chain, depends on the end-to-end distance  $R_e$  via the relation [3]

$$V_{\text{chain}} = R_e^3/A. \quad (3.3)$$

For an ideal affine compression of a diamond lattice the denominator has the value  $A = \sqrt{27}/4 \approx 1.3$  as discussed in Note 6.

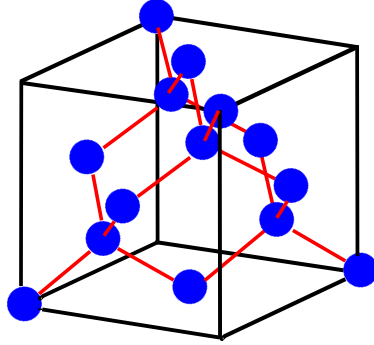


Figure 3.2: Diamond lattice containing 8 nodes (in dark blue) and 16 fully stretched chains (in red). Locations where a node occurs due to periodic boundary conditions are shown in light blue.

#### Note 6

The value for the parameter  $A$  derives from the following consideration: There are 16 chains (shown as red strokes in Figure 3.2) in the unit cell of a tetrafunctional gel. For a fully stretched gel the chains have chain length  $R_e = R_{\max}$ . The cubic unit cell has box length  $a$  and the distance between each node (in blue) is  $R_e = a \sqrt{3}/4$  (this is the length of the connection vector from the node at  $(0, 0, 0)^T$  to the node at  $\frac{a}{4}(1, 1, 1)^T$ ). Therefore, the total volume of the unit cell is

$$V = a^3 = \left( \frac{R_e}{\frac{\sqrt{3}}{4}} \right)^3 \text{ and the volume per chain is}$$

$$V_{\text{chain}} = \frac{V}{16} = \frac{R_e^3}{16 \frac{\sqrt{3}^3}{4^3}} = \frac{R_e^3}{\sqrt{27}/4} \implies A = \sqrt{27}/4$$

Whenever referring to the volume in the two single-chain models,

we mean the volume per chain  $V_{\text{chain}}$ . For a not completely stretched gel, the denominator  $A$  is non-trivially depending on the end-to-end distance [3]. For simplicity, we neglect this dependence and assume for the rest of the thesis that  $A$  is a constant (we discuss this point in the Section 3.6.8).

Relation (3.3) connects the end-to-end distance and the volume which is available for a chain: on compression the end-to-end distance decreases since the ends of the polymer chains are brought closer together — at the same time the available volume per chain shrinks as well. This fact is illustrated in Figure 3.3.

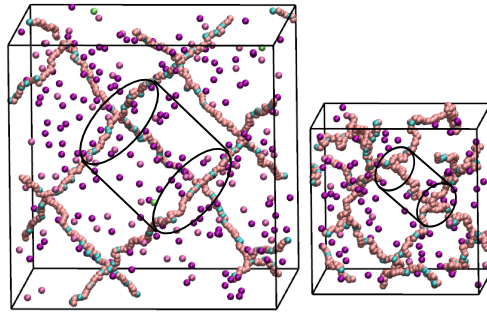


Figure 3.3: Illustration of the scaling of the (cylindrical) volume per chain  $V_{\text{chain}}$ : The volume per chain is bigger for a stretched gel, than for a compressed gel.

We still need to decide on the geometry of the volume per chain: In a macroscopic polyelectrolyte gel the monomers on one chain experience forces that originate from the electrostatic environment imposed by other chains and from the elastic response to the cross-linking. To emulate this environment, we choose a cylindrical volume and connect the chain ends through the cylinder top and bottom by applying PBCs.



Because of restrictions in the single-chain CGM and application of PBCs (see section 3.4) the cylinder height needs to be  $L(R_e) = R_e + b$  with the bond length  $b \approx 0.966\sigma \ll R_e$ . Here  $b$  takes a value typical for the Kremer-Grest FENE potential [55]. To use results obtained for an affine compression of the cylinder (see Section 3.3), and since  $b$  is typically much smaller than  $R_e$ , we approximate the volume available per chain via:

$$V_{\text{chain}} \approx L(R_e)^3 / A. \quad (3.4)$$

From the cylinder height and the cell volume (3.4) the outer cell radius  $R_{\text{out}}$  is given by:

$$R_{\text{out}} = \sqrt{\frac{V_{\text{chain}}(R_e)}{L(R_e)\pi}} = \sqrt{\frac{L(R_e)^3}{L(R_e)\pi A}} = \frac{L(R_e)}{\sqrt{\pi A}}, \quad (3.5)$$

as depicted in Figure 3.1. Because we consider only affine compressions we keep the aspect ratio  $\alpha = R_{\text{out}}/L$  constant in the single-chain CGM and the PB CGM.

## 3.3 Pressures in an Affinely Compressed Cylinder

Applying the chain rule for the volume derivative of the free energy of the system  $F_{\text{gel}}$  (at fixed aspect ratio  $\alpha$ ) we find the

pressure in the cylindrical cell geometry as [100]:

$$P_{\text{in}} = - \left. \frac{\partial F_{\text{gel}}}{\partial V_{\text{chain}}} \right|_{\alpha} = - \left. \frac{\partial F_{\text{gel}}}{\partial R_{\text{out}}} \frac{\partial R_{\text{out}}}{\partial V_{\text{chain}}} \right|_{\alpha} - \left. \frac{\partial F_{\text{gel}}}{\partial L} \frac{\partial L}{\partial V_{\text{chain}}} \right|_{\alpha} \quad (3.6)$$

$$= \frac{2}{3} P_{\text{side}} + \frac{1}{3} P_{\text{cap}}. \quad (3.7)$$

This result allows to express the pressure of the cylindrical system via the pressure contribution  $P_{\text{cap}}$  from the top and a pressure contribution  $P_{\text{side}}$  from the side of the cylinder.

## 3.4 Particle-Based Single-Chain Cell-Gel Model

Using the above described geometrical considerations, we introduce the first simplification for solving the many-chain problem of a periodic gel: the particle-based single-chain CGM depicted in Figure 3.1 ii). In the remainder of the text we call this model “single-chain CGM”. It consists of a single polyelectrolyte chain, confined to a cylinder of height  $L(R_e)$  and radius<sup>1</sup>  $R_{\text{out}}$ . The first and last monomers of the single chain are bonded through the periodic boundary conditions and fixed to the cylinder center but are free to diffuse along the cylinder axis. Applying PBCs mimics the electrostatic interactions in the gel where one end of the chain sees the beginning of the next chain, and where the fixed end points of the chain correspond to crosslinks in the gel.

---

<sup>1</sup>Note that in the MD simulation the outer cell radius is increased by one  $\sigma$  because the WCA wall of the outer cylinder interacts with all particles with a WCA interaction with cutoff  $2^{1/6}\sigma$  which corresponds to good approximation to a reduction of the ion available volume of about one  $\sigma$  in radial direction. This technicality is not further noted in the description of the MD simulations.

A single chain consists of  $N$  monomers and its contour length is  $R_{\max} = (N-1)b$ , where  $b$  is the average bond length. The particles in this model interact through the same type of interactions and parameters as in the periodic gel model (FENE bonds, WCA potential, Langevin thermostat, P3M, semi-grand-canonical ensemble). To compute the electrostatic forces and energies, we use the P3M algorithm<sup>2</sup> with 3D periodic boundary conditions, tuned to an absolute accuracy [56] in the electrostatic force of at least  $10^{-3} \frac{k_B T}{\sigma}$ .

In order to obtain a prediction for the swelling equilibrium, we need to find the state of chemical potential equilibrium and mechanical equilibrium (see introduction of chapter 3). Therefore, we need to calculate the pressure inside the gel with the cap contribution  $P_{\text{cap}}$  and the side contribution  $P_{\text{side}}$  (see Equation (3.7)). The caps of the cylinder are, however, only imaginary and not explicitly modeled. In the particle-based single-chain CGM, the cap pressure is given by the ensemble average of the  $(z, z)$  component of the instantaneous pressure tensor  $P_{\text{cap}} := \langle \Pi_{(z,z)} \rangle$ :

$$\Pi_{(z,z)} = \frac{\sum_i m_i \vec{v}_i^{(z)} \vec{v}_i^{(z)}}{V_{\text{chain}}} + \frac{\sum_{j>i} f_{ij}^{(z)} r_{ij}^{(z)}}{V_{\text{chain}}} + \Pi_{(z,z)}^{\text{Coulomb, P3M}}.$$

Here  $V_{\text{chain}}$  is the effective available volume,  $m_i$  is the mass of particle  $i$ ,  $\vec{v}_i$  the velocity (and the superscript  $(z)$  denotes the

---

<sup>2</sup> We compared the obtained forces of P3M with the MMM1D algorithm [103] designed for 1D periodic systems. We observed only small deviations compared to the P3M forces — this is especially true when using a gap in radial direction to separate the infinite number of infinitely long cylinders.

z-component).  $\vec{r}_{i,j}$  is the connection vector between particles  $i$  and  $j$ ,  $\vec{f}_{i,j}$  is the pair force (excluding the electrostatic force) between particles  $i$  and  $j$ . The last term is the zz-component of the instantaneous Coulomb pressure tensor [79] and accounts for the electrostatic interactions:

$$\Pi_{(z,z)}^{\text{Coulomb, P3M}} = \Pi_{(z,z)}^{\text{Coulomb, P3M, dir}} + \Pi_{(z,z)}^{\text{Coulomb, P3M, rec}} \quad (3.8)$$

The first contribution is<sup>3</sup>:

$$\begin{aligned} \Pi_{(z,z)}^{\text{Coulomb, P3M, dir}} &= \frac{1}{4\pi\epsilon_0\epsilon_r} \frac{1}{2V} \sum_{\vec{n}}^* \sum_{i,j=1}^N q_i q_j \times \\ &\left( \frac{\text{erfc}(\beta|\vec{r}_j - \vec{r}_i + \vec{n}|)}{|\vec{r}_j - \vec{r}_i + \vec{n}|^3} + \frac{2\beta\pi^{-1/2} \exp(-(\beta|\vec{r}_j - \vec{r}_i + \vec{n}|)^2)}{|\vec{r}_j - \vec{r}_i + \vec{n}|^2} \right) ((\vec{r}_j - \vec{r}_i + \vec{n})_z)^2 \end{aligned} \quad (3.9)$$

and the second term is:

$$\begin{aligned} \Pi_{(z,z)}^{\text{Coulomb, P3M, rec}} &= \frac{1}{4\pi\epsilon_0\epsilon_r} \frac{1}{2\pi V} \sum_{\vec{k} \neq 0} \frac{\exp(-\pi^2 \vec{k}^2 / \beta^2)}{\vec{k}^2} |S(\vec{k})|^2 \times \\ &\left( 1 - 2 \frac{1 + \pi^2 \vec{k}^2 / \beta^2}{\vec{k}^2} \vec{k}_z \vec{k}_z \right). \end{aligned} \quad (3.10)$$

$\vec{n}$  is a vector identifying the periodic image [79],  $\beta$  is the P3M splitting parameter,  $S(\vec{k})$  is the spacial Fourier transform of the charge density  $\rho(\vec{r}) = \sum_i q_i \delta(\vec{r} - \vec{r}_i)$  and  $\vec{k}$  are the wave vectors.

Note that the particle mass is irrelevant to the calculation of the ensemble averaged kinetic pressure tensor component  $\langle \Pi_{\text{kin},(z,z)} \rangle := \langle \frac{\sum_i m_i \vec{v}_i^{(z)} \vec{v}_i^{(z)}}{V_{\text{chain}}} \rangle$ . This statement holds in the canonical ensemble, the

---

<sup>3</sup>The asterisk denotes that terms with  $\vec{n} = 0$  and  $i = j$  are omitted, see [79].

grand-canonical ensemble and the semi-grand-canonical ensemble. The calculation in the canonical ensemble is straight forward and uses that the velocities are Maxwell-Boltzmann distributed: The probability density to find a certain component (e.g. the  $z$  component) is  $p(v_i^{(z)}) = \left(\frac{m_i}{2\pi k_B T}\right)^{1/2} \exp(-\beta \frac{m_i}{2} v_i^{(z)2})$ . The ensemble average is:

$$\langle \Pi_{\text{kin},(z,z)} \rangle = \frac{1}{V_{\text{chain}}} \sum_i \int_{v_i^{(z)}=-\infty}^{\infty} m_i v_i^{(z)} v_i^{(z)} p(v_i^{(z)}) dv_i^{(z)} \quad (3.11)$$

where the first sum runs over all particles  $i$ . A straight forward calculation yields  $\langle \Pi_{\text{kin},(z,z)} \rangle = \frac{\sum_j N_j k_B T}{V_{\text{chain}}}$ , where the last sum runs over all species  $j$ . This result is necessary in order to recover the limiting case of an ideal gas (which has no interactions) and for which the result of the isotropic pressure is well known:  $P_{\text{ideal}} = \langle \Pi_{\text{kin},(z,z)} \rangle = \frac{\sum_j N_j k_B T}{V}$ . This result holds in a slightly modified form also for the grand-canonical ensemble:  $\langle \Pi_{\text{kin},(z,z)} \rangle = \frac{\sum_j \langle N_j \rangle k_B T}{V}$  (with the average numbers of particles  $\langle N_j \rangle$ ) which can be proven by direct calculation. Finally, mixing both cases, we also obtain in the semi-grand-canonical ensemble that the kinetic pressure is independent of the particle mass. Therefore, we choose the arbitrary particle mass  $m_i = 1$  simulation unit.

To confine the particles in a cylindrical cell we need to impose a cylindrical constraint in the cuboid simulation box. To constrain the particles in the cylinder all particles are repelled from the cylinder wall via a Weeks-Chandler-Andersen interaction. The contribution of the pressure  $P_{\text{side}}$  acting on the side walls is directly measured as the average normal force on the outer wall per area. This pressure mainly arises due to the pressure that the mobile ions exert onto the wall. Therefore, the side pressure

could have also been obtained using the contact value theorem for the cylindrical cell model [31]. However, the contact theorem does not account for a possible interaction of the polymer chain with the wall and is therefore potentially less accurate.

To increase the accuracy of our description in the particle based models (namely the single-chain CGM and the periodic gel model), we include the excess pressure in the pressure of the reservoir (for Bjerrum lengths  $\lambda_B > 2\sigma$ , i.e.  $\epsilon_r < 80$ ):  $P_{\text{res}} = k_B T \sum_i c_i^{\text{res}} + P^{\text{ex, res}}$  (measured via independent MD simulations of the reservoir). In this case the excess pressure significantly lowers the pressure in the reservoir compared to the ideal gas pressure. This is due to the attractive nature of the electrostatic interaction.

Next, we present the second mean-field model which further simplifies the single-chain CGM.

## 3.5 Poisson-Boltzmann Cell-Gel Model

The Poisson-Boltzmann (PB) CGM uses a density-based description of the polymer charges and the surrounding ions instead of a particle-based description. As before, the polymer and the ion densities are enclosed in a cylinder with a radius  $R_{\text{out}}$  and a height of  $R_e + b$  as shown in Figure 3.1 iii). The electrostatic environment in a gel is mimicked through periodic replication of the system along the  $z$ -axis. Therefore, we can calculate the electrostatic interaction in the gel by solving the electrostatic problem for an infinite rod with prescribed charge density. In

contrast to the original rod cell model [96, 97] our rod is penetrable to the ions. The maximal radial extension of the polymer density is denoted by the radius  $a$  in Figure 3.1 iii).

In the PB model the distribution of the monomers is, in principle, arbitrary with the following two restrictions: 1) the maximal extension  $a$  needs to be smaller than the cell radius  $R_{\text{out}}$  and 2) the monomer distribution should be as realistic and as close as possible to that of a charged polymer bead-spring chain while maintaining the simplicity of the model. In the spirit of multiscale modeling, we use data from our previous single-chain CGM simulations to fulfill restrictions 1) and 2). From this data we extract a fitting curve for the average distance  $\langle r \rangle_{\text{MD}}$  of the chain monomers from the cylinder axis as a function of  $R_e$ :

$$\langle r \rangle_{\text{MD}}(R_e) = N\sigma \left( C_1 \left( \frac{R_e}{N\sigma} \right)^2 + C_2 \frac{R_e}{N\sigma} + C_3 \right), \quad (3.12)$$

with  $C_1 = -0.17$ ,  $C_2 = 0.14$  and  $C_3 = 0.03$  (fit to single-chain CGM data for chain lengths  $N \in \{39, 79, 300\}$ ,  $\epsilon_r = 80$ , for a fully charged chain without added salt, see Section 8.2).

This average distance of the monomers  $\langle r \rangle_{\text{MD}}$  from the end-to-end vector is imposed on the monomer densities occurring in the PB model. To investigate the influence of the chosen monomer densities, we investigate two distributions: a rectangular distribution and, in Section 3.6.7, a more realistic approximately Gaussian distribution with compact support. The probability density to find a monomer in a given distance  $r$  from the cylinder axis has, in the case of a rectangular distribution, the form

$$p(\vec{r}) = N_1 H(-(r - a)), \quad (3.13)$$

where  $H(x)$  denotes the Heaviside function, and  $\mathcal{N}_1$  a normalization such that  $p(\vec{r})$  is a probability density. This condition for  $p(\vec{r})$  gives  $\mathcal{N}_1 = \frac{1}{\pi a^2 L}$ . The parameter  $a$  is chosen such that the average distance from the end-to-end vector  $\langle r \rangle = \int_{V_{\text{chain}}} p(\vec{r}) r \, dV$  is equal to the average distance from the end-to-end vector which was observed in simulations of the single-chain CGM:  $\langle r \rangle \stackrel{!}{=} \langle r \rangle_{\text{MD}}$ . Thus, we obtain  $a = \frac{3}{2} \langle r \rangle_{\text{MD}}$ .

The above probability density to find a monomer  $p(\vec{r})$ , together with the charge fraction  $f$  and the number of monomers in the chain  $N$ , imply a corresponding charge density  $\rho_f(\vec{r}) = -N f e_0 p(\vec{r})$ , where  $e_0$  is the absolute value of the elementary charge. This charge density is the key input to the Poisson-Boltzmann equation which describes the electrostatic interaction in the system:

$$\nabla^2 \psi = -\frac{1}{\epsilon_r \epsilon_0} (q_+ c_+(\vec{r}) + q_- c_-(\vec{r}) + \rho_f(\vec{r})), \quad (3.14)$$

where  $\psi$  is the total electric potential,  $\epsilon_0$  the vacuum permittivity, and  $\epsilon_r$  is the relative permittivity. Charge densities  $\rho_i(\vec{r}) = c_i(\vec{r}) q_i$  are given by standard Poisson-Boltzmann theory [23] (with the choice of the reservoir potential  $\psi^{\text{res}} = 0$ ):

$$c_i(r) = c_i^{\text{res}} e^{\frac{-q_i \psi(x,y,z)}{k_B T}}, \quad (3.15)$$

where  $c_i^{\text{res}} = c_{\text{salt}}^{\text{res}}$  are the ion densities in the reservoir of species  $i$ , and  $i$  is either  $+$  or  $-$ .

Because we model macroscopic gels, we impose charge neutrality. Hence, there is no flux of electric field through the surface of the cell. The two boundary conditions which we employ for solving the PB Equation (3.14) are, therefore, that the radial electric field



$E_r(r)$  is zero at  $r = 0$  and  $r = R_{\text{out}}$ .

### Note 7

Applying a third incompatible boundary condition like e.g. setting the electric potential  $\psi(R_{\text{out}}) = 0$  would be wrong and electroneutrality of the system would be violated:

In chemical potential equilibrium we have equality of chemical potentials between the system and the reservoir:

$$\mu_i^{\text{gel}} = \mu_i^{\text{res}}. \quad (3.16)$$

In Poisson-Boltzmann theory the chemical potential is given by [23]:

$$\mu_i = \mu_i^\ominus + k_B T \ln(c_i(\vec{r})/c^\ominus) + z_i e_0 \psi(\vec{r}), \quad (3.17)$$

where  $c^\ominus$  is a reference concentration and  $\mu_i^\ominus$  is a reference chemical potential. In the limit of  $\epsilon_r \rightarrow \infty$  the electrostatic interaction and therefore the electric field in the system vanishes. For a system of ideal particles the equation practically loses its  $r$  dependence and we obtain (from Equation (3.16)):

$$k_B T \ln(c_i^{\text{gel}}/c^\ominus) + z_i e_0 \psi^{\text{gel}} = k_B T \ln(c_i^{\text{res}}/c^\ominus) + z_i e_0 \psi^{\text{res}}. \quad (3.18)$$

Due to the influence of the potential  $\psi$  (which does not vanish even for a close to ideal system) there may be a difference between the reservoir density and the density at the boundary: In general the concentrations at the boundary do not have to be equal to the reservoir concentrations:

( $c_i^{\text{res}} \neq c_i^{\text{gel}}$ ). This difference in concentrations translates into a difference in electric potential:

$$\psi^{\text{gel}} - \psi^{\text{res}} = \frac{k_B T \ln(c_i^{\text{res}}/c_i^{\text{gel}})}{z_i e_0}, \quad (3.19)$$

which converges to the ideal Donnan potential (in the limit of  $\epsilon_r \rightarrow \infty$ , where electric fields vanish). Compare Section 2.6.2, where we investigated an ideal Donnan-partitioned system.

The point to remember is that forcing the potential  $\psi(R_{\text{out}})$  to the reservoir potential  $\psi^{\text{res}} = 0$  is an incompatible boundary condition for a PB system in contact with a salt reservoir.

#### 3.5.1 Pressures in the Poisson-Boltzmann Model

In the PB model the pressure has two contributions: 1) the combined Maxwell and kinetic pressure and 2) the stretching pressure. For the standard PB theory the first contribution is given by [28]:

$$P_{\text{side}}^{\text{ions}} = k_B T \sum_i c_i(R) \quad (3.20)$$

$$P_{\text{cap}}^{\text{ions}} = k_B T \sum_i \langle c_i \rangle_z + \frac{\epsilon_0 \epsilon_r}{2} \langle E_r^2 \rangle_z, \quad (3.21)$$

where  $E_r = -\partial_r \psi(r)$  is the radial component of the electric field,  $\epsilon_0$  is the vacuum permittivity,  $\epsilon_r$  the relative permittivity and where  $\langle \mathcal{A}(r) \rangle_z = \frac{2\pi}{\pi R_{\text{out}}^2} \int_0^{R_{\text{out}}} r \mathcal{A}(r) dr$  is average value of observable  $\mathcal{A}$  across the cap. The side pressure is given by  $k_B T$  times the sum of the ion densities at the outer cylinder wall. This result is

in agreement with the contact value theorem [31]. We want to note that the densities at the outer cylinder wall do not have to coincide with the densities in the reservoir.

The second contribution is the stretching pressure which only acts on the cap. The stretching behavior of linear macromolecules under confinement is a delicate problem on its own and we refer the reader to further literature [104]. The simple stretching term which we use is motivated in the following. The stretching pressure is given as a volume derivative of a stretching free energy  $F_{\text{str}}$ :

$$P_{\text{cap}}^{\text{str}} = - \frac{\partial F_{\text{str}}(R_e)}{\partial V_{\text{chain}}} \quad (3.22)$$

$$= - \frac{\partial F_{\text{str}}}{\partial L} \underbrace{\frac{\partial L}{\partial V_{\text{chain}}}}_{1/(\pi R_{\text{out}}^2)} = - \frac{\partial F_{\text{str}}}{\partial R_e} \underbrace{\frac{\partial R_e}{\partial L}}_1 \frac{1}{\pi R_{\text{out}}^2}. \quad (3.23)$$

Since the stretching free energy needs to contain a confinement contribution  $F_{\text{conf}}$  and a tensile chain contribution  $F_{\text{chain}}$  it consists of two terms:  $F_{\text{str}} = F_{\text{chain}} + F_{\text{conf}}$ . Therefore one obtains:

$$P_{\text{cap}}^{\text{str}} = - \frac{1}{\pi R_{\text{out}}^2} \left( \frac{\partial F_{\text{chain}}}{\partial R_e} + \frac{\partial F_{\text{conf}}}{\partial R_e} \right). \quad (3.24)$$

The first term is given by the force extension curve of a freely jointed chain  $-\frac{\partial F_{\text{chain}}}{\partial R_e} = \frac{k_B T}{b} \mathcal{L}^{-1} \left( \frac{R_e}{R_{\text{max}}} \right)$  (with the inverse Langevin function  $\mathcal{L}^{-1}$  or a numerical approximation [105] and the maximal contour length [58]  $R_{\text{max}} = (N - 1)b$ ).

For the second term, the confinement free energy, we use the result for a free, ideal polymer:  $F_{\text{conf}} = B k_B T \frac{N b^2}{R_e^2}$  [58, p. 115]. We choose the proportionality constant  $B$  such that the stretching

force is zero at the equilibrium extension:  $\left. \frac{\partial F_{\text{str}}}{\partial R_e} \right|_{R_0} + \left. \frac{\partial F_{\text{conf}}}{\partial R_e} \right|_{R_0} = 0$

yielding  $B = \frac{R_0^3}{2Nb^3} \mathcal{L}^{-1}\left(\frac{R_0}{R_{\text{max}}}\right)$ . The final expression for the stretching pressure is:

$$P_{\text{cap}}^{\text{str}} = \frac{1}{\pi R_{\text{out}}^2} \frac{k_B T}{b} \left( \frac{R_0^3}{R_e^3} \mathcal{L}^{-1}\left(\frac{R_0}{R_{\text{max}}}\right) - \mathcal{L}^{-1}\left(\frac{R_e}{R_{\text{max}}}\right) \right) \quad (3.25)$$

The equilibrium extension  $R_0$  is a free parameter, and we use the relation  $R_0 = 1.2bN^{0.588}$  which was found for a system of neutral chains interacting via a WCA potential [3].

In total, the cap pressure is given by  $P_{\text{cap}} = P_{\text{cap}}^{\text{str}} + P_{\text{cap}}^{\text{pions}}$ , and together with eq. (3.7) one obtains the pressure in the gel model  $P_{\text{in}}$ . The PB model is expected to work well in aqueous solutions if there are no multivalent ions, high charge densities (e.g. at high compression of the gel), or high ionic concentrations present [26, 27]. Problems in PB theories arise due to neglecting ionic correlations as well as excluded volume interactions. Also, the simplistic stretching pressure  $P_{\text{cap}}^{\text{str}}$  (which is independent of the charge fraction and the salt concentration) adds a source of inaccuracy. These limitations are not present in our single-chain CGM.

## 3.6 Strong Polyelectrolyte Gels

### 3.6.1 Pressure-Volume Curves

All models which were described in the previous sections give pressure-volume curves (similar to stress-strain curves), see Fig-

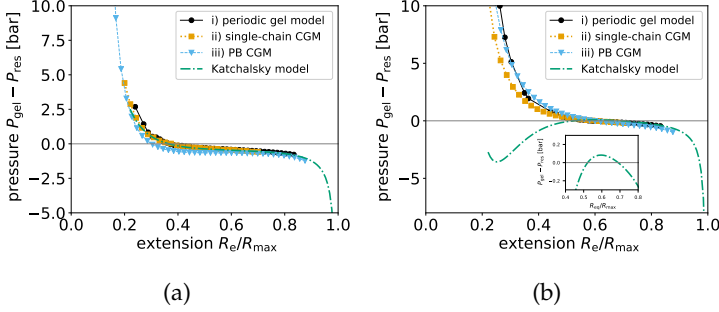


Figure 3.4:  $P(R_e)$  curves for a)  $f=0.125$  and b)  $f=1$ , both for  $N=64$ ,  $c_{\text{salt}}^{\text{res}} = 0.01 \text{ mol/L}$ ,  $\lambda_B = 2\sigma$  (corresponds to  $\epsilon_r = 80$ ). The inset in figure b) shows the Katchalsky model data from figure b) enlarged. In the inset two zero crossings are visible. The abscissa is the equilibrium end-to-end distance divided by the maximum elongation of the chain and therefore parametrizes the volume per chain via eq. (3.4). As the end-to-end distance can be easily converted to a volume via Equation (3.4) we refer to the  $P(R_e)$  as  $PV$  curve.  $PV$  curves for other parameters can be found in the supporting information of reference [2].

ure 3.4. In addition, we included  $PV$  curves from the Katchalsky model which is a simple free energy model, for details please consult the papers authored by [3] and [63].

Compared to the Katchalsky model, our new models work for all charge fractions. At high charge fractions ( $f > 0.5$  [3]) the Katchalsky model produces non-physical  $PV$  curves, which is obvious because: a) the Katchalsky  $PV$  curves have multiple zero crossings (see Figure 3.4) and b) the Katchalsky  $PV$  curves do not have a form compatible with the  $PV$  curves of the periodic gel model. At those charge fractions the Katchalsky model fails due to the used electrostatic energy functional which is derived from a linearization of the PB equation [63]. Since the model is

only applicable for gels with low charge fractions, it can only be used for the prediction of desalination energy costs of weakly charged gels [106]. In contrast to the Katchalsky model, our new PB CGM gives monotonic  $PV$  curves even for highly charged gels ( $f > 0.5$ ). Additionally, our PB CGM also shows better agreement with the periodic gel model than the self-consistent field theory presented in Ref. [90, Figure 2]. Hence, the  $PV$  curves could be used for an improved prediction of the energy costs for desalinating seawater using highly charged gels [106].

From Figure 3.4, the swelling equilibrium for the corresponding gel can be obtained by identifying the zero crossing (where the reservoir pressure and the pressure in the gel balance). The dependence of the swelling equilibria on experimental conditions, like the salt concentration, or gel parameters, like the charge fraction of the monomers, are examined in the next section.

#### 3.6.2 Swelling Equilibria

In Figure 3.5, the scaled equilibrium extension  $R_{eq}/R_{max}$  is shown as a function of the salt concentration in the reservoir ( $c_{salt}^{res}$ ) and the charge fraction ( $f$ ). In agreement with literature [64, 65, 68, 69, 70, 71, 72, 73, 74, 75, 76, 3], we find, that the gel swells a) more with increased charge fraction  $f$  and b) less with higher salt concentration in the reservoir.

In both subfigures of Figure 3.5 we observe that the single-chain CGM and the periodic gel model agree very well. However, the single-chain CGM is more efficient and saves about an order of magnitude in CPU time. The PB CGM shows deviations from our reference data which depend on the chosen parameters, but

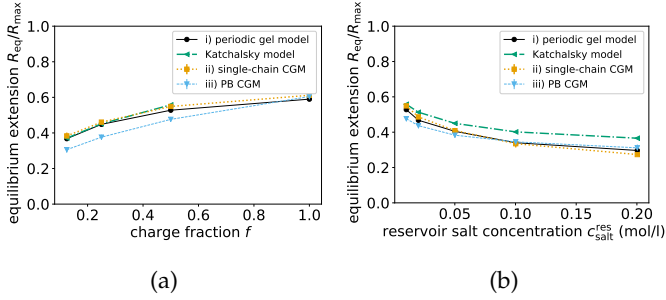


Figure 3.5: Comparison of swelling predictions of the periodic gel model i), the two new CGMs ii-iii) and the Katchalsky model for a polymer of chain length  $N = 64$  in aqueous solution ( $\epsilon_r = 80$ ). The equilibrium swelling  $R_{eq}$  as a) a function of the charge fraction  $f$  for  $c_{salt}^{res} = 0.01 \text{ mol L}^{-1}$  and b) as a function of the reservoir salt concentration  $c_{salt}^{res}$  for  $f = 0.5$ . The equilibrium volume is determined by locating the volume where  $P_{in}(V_{eq})$  and  $P_{res}$  are equal by using a linear interpolation. The error bar is the width of the interval at which the intersection happens. The error bar is typically smaller than the symbol size. Note that in the first plot the points for the Katchalsky model do not cover the whole plot range. This is due to the fact that the Katchalsky model fails for these parameters [3].

in general the trend is reproduced. We find that the PB CGM also works for gels which are highly charged (where the Katchalsky model fails). In agreement with [3] we find, that the Katchalsky model offers very good gel swelling predictions for gels with low charge fraction. The exact quantification of inaccuracies of the different models is, however, a difficult problem. This arises from two facts:

- The PB model predictions can only be compared to a finite set of reference data which are computationally expensive to generate.
- The high dimensionality of the parameter space: predictions for gel swelling  $R_{eq}$  are made for different chain lengths, charge fractions, salt concentrations and dielectric permittivities. We observe that the PB and the Katchalsky model show differing suitability in predicting the swelling equilibrium in various parts of the parameter space.

For completeness, we include the swelling equilibria which were determined for all parameter combinations in the appendix. This data, reveals that, compared to the periodic gel model, the PB CGM predicts too low swelling equilibria at low salt concentrations (compared to the periodic gel MD data) and too large swelling equilibria for highly charged gels  $f \rightarrow 1$ . In the following, we explicitly name some simplifying assumptions made in the PB model which could cause these deviations:

- The polymer charge density  $\rho_f(\vec{r})$  in the PB model is, for simplicity, not dependent on the salt concentration or the charge fraction which are imposed in the model. In principle, it would be possible to obtain  $\rho_f(\vec{r})$  from the



single-chain CGM, making use of multi-scale modeling, for all parameter combinations  $c_{\text{salt}}^{\text{res}}, f, N$ . This would however greatly increase the model complexity.

- The stretching contribution  $P_{\text{cap}}^{\text{str}}$  is independent of the salt concentration and the charge fraction  $f$ . For a charged polymer, we would expect a different stiffness depending on a) the salt concentration and b) the charge fraction. At low salt concentrations or high charge fractions the stiffness (or persistence length) should increase, resulting in a higher extension. Therefore, the force-extension of a polyelectrolyte should favor more stretched states at low salt concentrations or high charge fractions. To obtain better suited stretching pressures is not straightforward and would be a research topic on its own.

As mentioned above, the Katchalsky model does not provide valid predictions for high charge fractions, which can be seen in the missing points in Figure 3.5a. Another tendency, which can be seen for some parameter combinations (e.g. in figure 3.5b), is that the Katchalsky model exhibits bigger deviations from the periodic gel model for higher salt concentrations. This could be related to the fact that the Debye-Hückel approximation works only well for low ion concentrations (below 0.01 mol/L for 1:1 electrolytes [107] when used for predicting the ionic activity coefficient). Another possible reason could be that the elastic pressure contribution in the Katchalsky model is independent of charge fraction and salt concentration (similar to the PB model above).

Our new PB CGM also allows to obtain predictions for the equilibrium extension of long chains in a gel which were previously

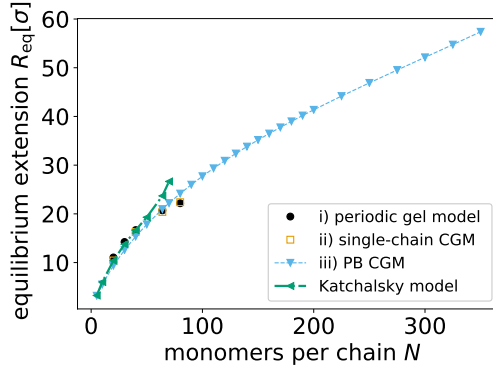


Figure 3.6: Predictions for the equilibrium end-to-end distance of monodisperse gels of different chain length  $N$  for  $f = 0.5$ ,  $\epsilon_r = 80$  and  $c_{\text{salt}}^{\text{res}} = 0.1 \text{ mol/L}$ .

too expensive to simulate. For one set of parameters we show this prediction in Figure 3.6 where the equilibrium end-to-end distance is plotted as a function of the chain length  $N$ . Additionally, we also show the predictions of the single-chain CGM, the periodic gel model and the Katchalsky model. As one would expect, the equilibrium end-to-end distance increases with chain length. The exact results in Figure 3.6 are important for the later treatment of polydisperse gels (as explained in Section 3.6.6). At this point, we want to note that the Katchalsky model fails for chain lengths  $N \gtrsim 80$  (at  $f = 0.5$ ) and already shows significant deviations to the periodic gel model at  $N = 80$ . As reported by Richter [1, Figure 70.] the electrostatic pressure contributions of the Katchalsky model are too negative for  $f = 0.5$  compared to the periodic gel model. These negative pressure contributions also introduce multiple zero-crossings in the  $PV$  curve of the Katchalsky model for  $N \gtrsim 80$  where the model fails.

The overall agreement between the two new models and the expensive periodic gel simulations is evaluated in figure 3.7 which is a parametric plot with the periodic gel data on the abscissa and the data of the other models on the ordinate. A straight line with slope one would indicate perfect agreement with the periodic gel simulations (this “ideal line” is indicated with the label “linear” in Figure 3.7). The single-chain CGM fits the periodic gel data very well in the whole parameter space and therefore lies close to the “ideal line” (a fitted line  $y(x) = mx$  through the single-chain CGM data has the slope  $m = 1.01$  and a coefficient of determination  $R^2 = 0.998$ ). The PB CGM in general has a similar trend as the periodic gel data but has deviations to the periodic gel data (a fitted line through the PB CGM data has slope  $m = 0.968$  and  $R^2 = 0.98$ ). As outlined above, the data points where the swelling is below the “ideal line” are, in tendency, data at low salt concentration. PB CGM data which are above the “ideal line” are in tendency data at high charge fraction  $f$ . In contrast to the Katchalsky model our new models can be applied even at high charge fractions and high salt concentrations. The Katchalsky model data above the ideal line are due to deviations at high salt concentrations, while Katchalsky model data below the ideal line are due to deviations at high charge fraction. A fitted line to the Katchalsky model data including the outliers (excluding the outliers at  $f = 1$ ) has a slope  $m = 0.74$  ( $m = 1.07$ ) and a coefficient of determination  $R^2 = 0.72$  ( $R^2 = 0.992$ ).

As we see in Figure 3.7 there seems to be “scattering” around the predicted periodic gel data which serve as benchmark. The “scattering” of the different model data around the periodic gel data in Figure 3.7 is due to the models not working perfectly and

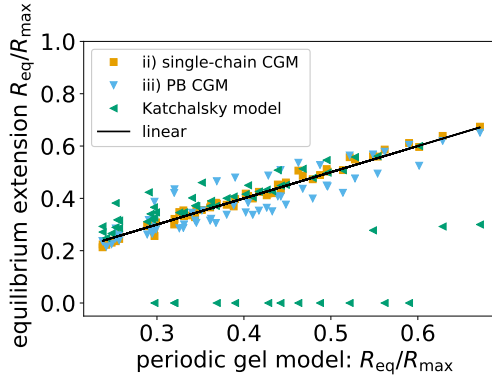


Figure 3.7: Swelling equilibria of the single-chain CGM and the PB CGM compared to the more detailed periodic gel model. The results are presented for a wide set of parameter combinations with  $\epsilon_r = 80$ ,  $N \in \{40, 64, 80\}$ ,  $f \in \{0.125, 0.25, 0.5, 1\}$  and  $c_{\text{salt}}^{\text{res}} \in \{0.01, 0.02, 0.05, 0.1, 0.2\} \text{ mol L}^{-1}$ . The linear function has the form  $y(x) = x$  and is termed “ideal (prediction) line”. Note that the Katchalsky model produces outliers at high charge fractions which go hand in hand with high degrees of swelling in the periodic gel model. To show the failure of the Katchalsky model we included data points for which the Katchalsky model failed to give a prediction. For illustration purposes we assign those data points to  $R_{\text{eq}}/R_{\text{max}} = 0$ . We want to note that our comparison includes more charge fractions below  $f = 0.5$  than above. This might lead to the wrong impression that the Katchalsky model works in most of the charge fraction although it does not work for  $f > 0.5$ .

projecting the results obtained in a three-dimensional parameter space:  $\{c_{\text{salt}}^{\text{res}}, N, f\}$  onto a one dimensional abscissa. While there is no “scattering” (in the sense of a strongly non-monotonic behavior) of the data around the ideal line for a single parameter set (e.g.  $R_{\text{eq}}(\{c_{\text{salt}}^{\text{res}}\}, N = \text{fix}, f = \text{fix})/R_{\text{max}}$ ) there is apparent “scattering” when plotting two data sets (e.g.  $R_{\text{eq}}(\{c_{\text{salt}}^{\text{res}}\}, N = 40, f = 0.125)/R_{\text{max}}$  and  $R_{\text{eq}}(\{c_{\text{salt}}^{\text{res}}\}, N = 80, f = 1)/R_{\text{max}}$ , see appendix) from separate regions of the parameter space together in Figure 3.7. This “scattering” does not mean that predictions of the models vary in a strongly non-monotonic when only varying one parameter.

Deviations between the simplified models and the periodic gel model are either due to simplified descriptions of the interactions (as discussed above) or at least in part due to the fact that the parameter  $A$  is not a constant but rather a function of the end-to-end distance [3]. This non-affine behavior exists in the periodic gel model and probably in real polymer networks [108]. Therefore, a refined theory would also take into account that the compression of a gel is not affine and would deal with  $A(R_e)$ . In the Section 3.6.8 we investigate the effect of changing  $A$  on the predicted end-to-end distance in the PB CGM and find, however, that the influence is small.

#### 3.6.3 Bulk Modulus

Mechanical properties are important, for example, when evaluating the energetic costs for desalination with polymer gels [106]. One mechanical property of interest is the isothermal bulk mod-

ulus  $K$  of a gel as a measure for the mechanical strength:

$$K = -V \frac{\partial P_{\text{gel}}}{\partial V} \approx -V \frac{\Delta P_{\text{gel}}}{\Delta V}. \quad (3.26)$$

In the case of the single-chain CGMs we use  $V_{\text{chain}}$  instead of  $V$ . The volume derivative of the pressure curve is approximately calculated via the finite difference quotient of the points which are at the intersection of the reservoir and system pressure.

The scaling behavior of the shear modulus is connected to the scaling of the bulk modulus  $K$  via<sup>4</sup> the Poisson ratio [109]  $\nu$ :

$$K = \frac{2(1 + \nu)}{3(1 - 2\nu)} G. \quad (3.27)$$

The scaling analysis by Barrat et al. [101] (which is also based on the pressure balance of the osmotic and the elastic pressure using the ideal Donnan equilibrium) predicts that in swelling equilibrium the shear modulus of a polymer gel is given by  $G = k_B T \left( \frac{c_0}{N} \right) \left( \frac{R_{\text{eq}}^2}{Nb^2} \right)$ , where  $c_0 = N/R_{\text{eq}}^3$  is the monomer concentration in the gel in equilibrium [101],  $N$  the number of monomers per chain, and  $b$  the size of the monomer. The equilibrium end-to-end distance scales with the number of monomers per chain  $R_{\text{eq}} \propto N^{\nu_{\text{gel}}}$ , where  $\nu_{\text{gel}}$  is a Flory exponent. Note that the Flory exponent of a free chain and the Flory exponent  $\nu_{\text{gel}}$  do not agree

---

<sup>4</sup>We note that our single-chain CGM and the PB CGM have a Poisson ratio  $\nu = -\frac{\Delta R_{\text{out}}}{R_{\text{out}}} \frac{L}{\Delta L} = -1$  and therefore the two models itself are auxetic ( $\nu < 0$ ) - i.e. stretching the chain enlarges the volume in the dimension perpendicular to the applied force. However, real gels are not auxetic materials. It is, therefore, important to remember that the single-chain CGM and the PB CGM are models for a gel under isotropic compression: Compressing the gel reduces the volume which is available per chain and reduces the end-to-end distance of the chains in the gel.

in general (compare Barrat et al. [101]). Using this we obtain  $G \propto N^{-(\nu_{\text{gel}}+1)}$ . In salt free solution, we further have the relation for the equilibrium end-to-end distance in a gel [101]  $R_{\text{eq}} \propto Nb$ . Therefore, we expect  $K \propto G \propto 1/N^2$ . For a gel in contact with a saline solution and in a good solvent we expect [101]  $R_{\text{eq}} \propto bN^{3/5}$ , which alters the scaling prediction  $K \propto G \propto N^{-8/5} = N^{-1.6}$ .

The bulk modulus obtained by the PB CGM is displayed in Figure 3.8 together with values obtained from the single-chain CGM, the periodic gel model, and the Katchalsky model. For the two particle-based models the  $PV$ -curve and the errors in the pressure are recorded during the simulation. The resulting error in the bulk modulus is then calculated according to error propagation in the volume  $V$  and the slope  $\partial P_{\text{gel}}/\partial V$ . The used formula is:

$$\Delta K = \left| \left( \frac{\partial P_{\text{gel}}}{\partial V} \right)_{\text{eq}} \right| \Delta V_{\text{eq}} + V_{\text{eq}} \Delta \left( \frac{\partial P_{\text{gel}}}{\partial V} \right)_{\text{eq}}, \quad (3.28)$$

where the symbol  $\Delta$  denotes that the error margin is positive. The error margins  $\Delta V_{\text{eq}}$  and  $\Delta \left( \frac{\partial P_{\text{gel}}}{\partial V} \right)_{\text{eq}}$  are determined using the error bars of the pressure next to the equilibrium point.

In our PB CGM, we find scaling exponents  $K \propto N^{-1.54 \pm 0.06}$  (for  $f = 0.125$ ),  $K \propto N^{-1.55 \pm 0.03}$  (for  $f = 0.5$ ) or  $K \propto N^{-1.87 \pm 0.06}$  (for  $f = 1$ ) via fitting<sup>5</sup> to data  $N > 5$ . The PB CGM data for the bulk modulus do not follow a perfect power law as predicted by Barrat [101], there are deviations at very small chain lengths and large chain lengths. Therefore, the scaling exponents for the  $N$

---

<sup>5</sup>The errors ( $\pm$ ) are the standard deviations of the slope obtained from the square root of the corresponding entry in the covariance matrix of the fit. For fitting a line in the log-log plot the Levenberg-Marquardt algorithm was used.

### 3 Improved Gel Models: Cell-Gel Models

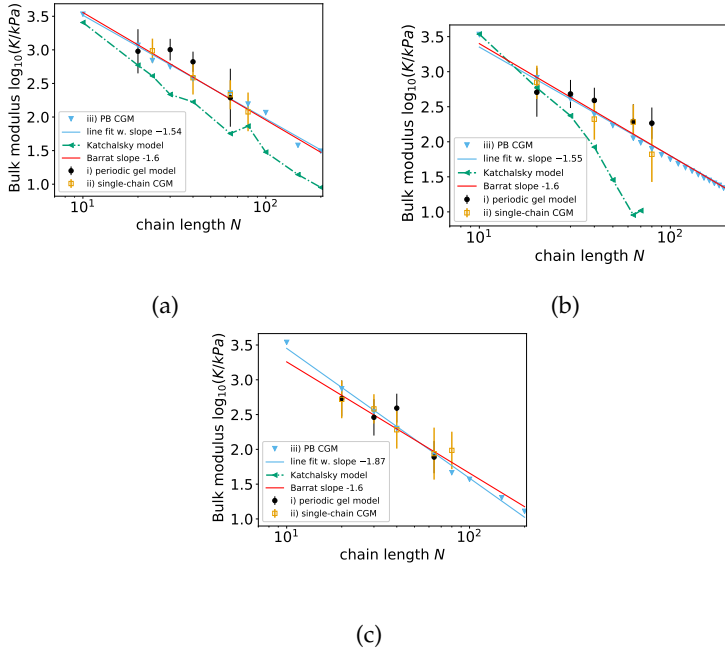


Figure 3.8: Predictions of periodic gel model i), the two single-chain CGMs ii-iii) and the Katchalsky model for the bulk moduli  $K$  of monodisperse gels of different chain length  $N$  for a)  $f = 0.125$ , b)  $f = 0.5$  and c)  $f = 1$  at  $\epsilon_r = 80$  and  $c_{\text{salt}}^{\text{res}} = 0.1 \text{ mol/L}$ . For  $f = 1$  the Katchalsky model [3] fails.



dependence of the bulk modulus should be taken with care. We observe that the scaling exponents of the bulk modulus with  $N$  are close to the scaling prediction  $K \propto G \propto N^{-1.6}$  when the gels carry a low charge fraction. We also find that the PB CGM, the single-chain CGM, and the periodic gel model agree within error bars. The Katchalsky model, on the other hand, shows significant deviations to the periodic gel model, it deviates from the particle-based model predictions both at charge fraction  $f = 0.125$  and  $f = 0.5$  or even fails at  $f = 1$  (where we have no Katchalsky model prediction). For low charge fractions the slope of the Katchalsky data is still compatible with Barrat's scaling prediction while for charge fraction  $f = 0.5$  the deviation to Barrat's scaling prediction and the periodic gel data is already significant. We conclude that our new models provide an improved description of the mechanical properties of gels at intermediate or high charge fractions ( $f \geq 0.5$ ) when compared to the Katchalsky model.

We also want to note that the error bars on the bulk modulus for the particle-based models (obtained via propagation of error) are big. Because of this fact, we do not fit scaling exponents to the particle-based model data. It seems that in Figure 3.8 b) the periodic gel model would have a different best fit line than the PB CGM. One possible reason for this could be that the PB CGM uses a stretching pressure which is derived from an ideal model, neglecting a possible salt dependence or charge fraction dependence of this pressure contribution. A chain length dependent correction to the ideal behavior would also change the bulk modulus predicted with Equation (3.26).

In Figure 3.9 we also display the volume at swelling equilibrium as a function of  $N$ . Like Barrat, we assume that the volume of the

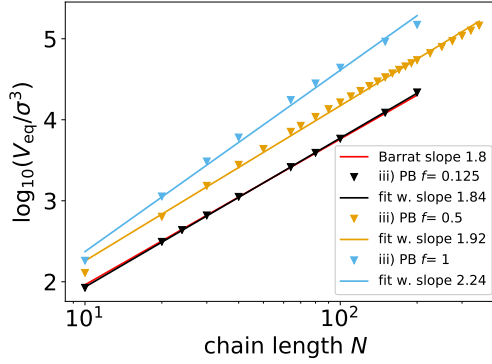


Figure 3.9: PB CGM predictions for the chain length ( $N$ ) dependence of the volume per chain of monodisperse gels at  $\epsilon_r = 80$  and  $c_{\text{salt}}^{\text{res}} = 0.1 \text{ mol/L}$ . The different charge fractions  $f$  are encoded via color as indicated in the legend. The volume is calculated according to eq. (3.4) using the equilibrium end-to-end distance. The scaling prediction by Barrat is shown in red (with fitted y-intercept to the PB model data for  $f = 0.125$ ). We expect the idealized model by Barrat [101] to work best for low charge fractions.

gel is proportional to the end-to-end distance cubed [101]. We expect the following scaling behavior in swelling equilibrium  $V_{\text{eq}} \propto N^3$  (in the salt free case) and  $V_{\text{eq}} \propto N^{9/5} \approx N^{1.8}$  (in the case of added salt) [101]. As one can see in Figure 3.9 the PB CGM predicts a scaling of  $V_{\text{eq}} \propto N^{2.24 \pm 0.065}$  (for  $f = 1$ ),  $V_{\text{eq}} \propto N^{1.92 \pm 0.03}$  (for  $f = 0.5$ ) and  $V_{\text{eq}} \propto N^{1.84 \pm 0.01}$  (for  $f = 0.125$ ) which is close to Barrat's prediction for added the salt ( $V_{\text{eq}} \propto N^{9/5} = N^{1.8}$ ). In the case of high charge fraction  $f = 1$  we do not expect the model by Barrat to work anymore since ions are treated on the ideal level [101]. Therefore, the scaling exponent in the PB model is different than the prediction by Barrat [101]. Because  $V_{\text{eq}} \propto R_{\text{eq}}^3 \propto N^{3\nu_{\text{gel}}}$ , we find “effective” Flory exponents

$\nu_{\text{gel}} = 0.613 \pm 0.01$  (for  $f = 0.125$ ),  $\nu_{\text{gel}} = 0.64 \pm 0.01$  (for  $f = 0.5$ ) or  $\nu_{\text{gel}} = 0.75 \pm 0.03$  (for  $f = 1$ ). For highly charged gels the electrostatic interactions stretch the gel more and the swelling increases (resulting in a higher  $\nu_{\text{gel}}$ ).

### 3.6.4 Influence of the Relative Permittivity

The relative permittivity  $\epsilon_r$  controls the strength of the electrostatic interaction in the implicit solvent approach. At  $\epsilon_r \approx 80$ , both, the single-chain CGM and the PB CGM, agree well in their prediction for the swelling equilibrium (see figure 3.10). The results for the PB CGM and the single-chain CGM are shown in figure 3.10. For lower values of  $\epsilon_r$  the electrostatic interactions become so strong that ion correlation effects occur [110]. These correlation effects cannot be captured by the mean-field Poisson-Boltzmann approach [110] and produce a stronger collapse of the gel than predicted by the PB CGM.

The effect of varying  $\epsilon_r$  was previously investigated (for periodic gel model) by Schneider et al. [111] who observed a similar trend. We also confirm the accuracy of the single chain CGM by comparing our data to those of periodic gel simulations at  $\epsilon_r = 80$  and  $\epsilon_r = 20$ .

At larger relative permittivities, electrostatic interactions diminish. In the limit of  $\epsilon_r \rightarrow \infty$  the electrostatic interaction energy approaches zero, and the salt is partitioned according to the ideal Donnan prediction [3]:

$$c_{\text{salt}}^{\text{gel}} = \sqrt{\left(\frac{fc_0}{2}\right)^2 + c_{\text{salt}}^{\text{res}2}} - \frac{fc_0}{2}. \quad (3.29)$$

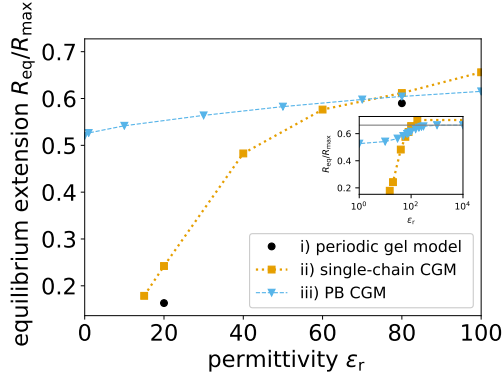


Figure 3.10: PB CGM and single-chain CGM predictions for the equilibrium end-to-end distance of monodisperse gels for  $N = 64$ ,  $f = 1$  and  $c_{\text{salt}}^{\text{res}} = 0.01 \text{ mol/L}$  at various different relative permittivities  $\epsilon_r$ . Additionally, we confirm the accuracy of the single-chain CGM simulations by providing two periodic gel data points for the swelling equilibrium at  $\epsilon_r = 80$  and  $\epsilon_r = 20$ . The inset shows the limiting behavior of the PB CGM and the single-chain CGM for large relative permittivities. In this limit salt is partitioned according to the ideal Donnan behavior (gray line) for the PB CGM. The data point at  $\epsilon_r = \infty$  for the single-chain CGM is obtained by switching the electrostatic interactions off.

Here  $c_{\text{salt}}^{\text{gel}}$  is the salt concentration inside the gel,  $c_{\text{salt}}^{\text{res}}$  the salt concentration in the reservoir and  $c_0$  the concentration of monomers in the gel.

This salt partitioning allows to predict the behavior in the limit  $\epsilon_r \rightarrow \infty$  since then ions can be treated as an ideal gas and the pressure contributions  $P_{\text{cap}}$  and  $P_{\text{side}}$  can be evaluated easily via the homogeneous densities (the electric field goes to zero for  $\epsilon_r \rightarrow \infty$ ). The Donnan-partitioning is used for calculating the cell model pressures and yields the gray line in the inset in Figure 3.10. In figure 3.10 it is visible that the PB CGM and the single-chain CGM swell slightly different for  $\epsilon_r \rightarrow \infty$ . This difference of roughly 6 % in  $R_e/R_{\text{max}}$  appears due to different stretching pressures in both models and possibly due to the neglect of excluded volume interactions in the PB model.

We want to point out that the strong collapse in solvents with low dielectric constant cannot be accurately represented by theories which treat the electrostatic interactions only on an approximate ideal level (ensuring electroneutrality via the Donnan equilibrium) or on a Debye-Hückel level, as is done for example in the approaches by Katchalsky [63], Tanaka [112], Khokhlov [82], or the model by Barrat [101].

#### 3.6.5 Mass-Based Degree of Swelling (for Monodisperse Gels)

For better comparison with experimental results on swelling equilibrium, it is instructive to introduce a mapping from the predicted end-to-end distances  $R_{\text{eq}}$  to the mass of the solvent taken

up. This facilitates the comparison of experimental results where the swelling equilibrium is often [113, 114, 115, 12, 116] reported as a fraction of the mass of the solvent in the swollen state divided by the mass of the dry state of the gel  $Q_m = m_{\text{solvent uptake}}/m_{\text{dry}}$ . This mapping requires some modeling assumptions. First, the mass of the dry state is determined by the number of monomers  $N$  per chain, the total number of chains  $N_{\text{chains}}$  in the gel and the mass of the monomers  $m_0$ :

$$m_{\text{dry}} = m(N)N_{\text{chains}}, \quad (3.30)$$

where  $m(N) = Nm_0$  is the mass of one chain with  $N$  monomers. The monomer mass depends on the experimental preparation and we choose  $m_0 = 94 \text{ u}$  so that the monomers represent sodium acrylate. The second modeling assumption is that we can measure the mass of the solvent in the swollen gel via its volume<sup>6</sup> and an approximate density  $\rho_w \approx 1 \text{ kg/l}$  which is close to that of pure water:

$$m_{\text{solvent uptake}} = V_{\text{chain}}(N)\rho_w N_{\text{chains}}, \quad (3.31)$$

where  $V_{\text{chain}}(N)$  is the volume per chain given by eq. (3.4). This volume per chain is predicted, e.g., by the single-chain CGM or the PB CGM (compare Figure 3.6). The volume of the gel is obtained by multiplying  $V_{\text{chain}}$  with the number of chains  $N_{\text{chains}}$  (which cancels in the calculation of  $Q_m$ ).

This simple mapping allows for the prediction of mass-based degrees of swelling. The results for monodisperse gels are

---

<sup>6</sup>Being exact one would need to subtract the volume which is occupied by the gel monomers from  $V(N)$ . For swollen gels the excluded volume by the gel is, however, negligible.

shown in Figure 3.12 as a black curve. In the following, we generalize our mapping of the (mass based) degree of swelling and introduce polydispersity effects.

#### 3.6.6 Chain Length Polydispersity

So far we have only treated monodisperse macroscopic gels. In reality, however, most gels are highly polydisperse [117, 92, 91, 118]. Properties of polymeric systems typically depend on the chain length polydispersity and in many applications this feature may be used to improve material properties for a given application [59, p.10]. Nevertheless, polydispersity is often neglected in theoretical considerations and a monodisperse molar mass distribution is assumed.

Chain length heterogeneity is a parameter for which data for comparison cannot easily be obtained via MD/MC simulations of periodic charged gels: A simulation of a heterogeneous gel would require prohibitively time-consuming simulations with a huge simulation box to realize a representative distribution of the chain length distribution. Additionally, a strict comparison to experiments is difficult because the exact chain length distribution in typical experiments is unknown due to the insufficient characterization of the topology of real gels. We employ a simple approach where we assume that a polydisperse macroscopic gel can be described by partitioning the total volume into subcells which contain chains of possibly different length in each cell. Given that we know the probability mass function (pmf) for the polymer length in a gel  $p(N)$  (see e.g. Panyukov and Rabin [117])

we can then easily obtain the degree of swelling for a polydisperse gel. In the studies by [91] and [92] the strand length distribution is exponential or close to exponential and therefore very broad. As outlined by [118] random cross-linking gives a Flory-Schulz distributed chain length polydispersity, i.e. a geometrical distribution or in good approximation an exponential distribution [118].

#### Note 8

A typical chain length distribution in polymers is the Flory Schulz distribution [119]. The probability to find an N-mer (i.e. a polymer made up from N monomers) was derived by Flory based on the assumption that  $p$  is the probability for a reaction which elongates the polymer and  $1 - p$  is the probability for a chain termination: In this case the probability of finding a N-mer is equal to  $N - 1$  successful reactions and one chain termination reaction:

$$p(N) = p^{N-1}(1 - p) \quad (3.32)$$

This is geometric distribution is referred to as Flory-Schulz distribution. Sometimes  $a = 1 - p$  is introduced, resulting in Equation (3.33).

For simplicity, we assume that the chain length is distributed<sup>7</sup> according to this geometric or Flory-Schulz distribution [119, 22]:

$$p_a(N) = a(1 - a)^{N-1}, \quad (3.33)$$

---

<sup>7</sup>The monodisperse case for a gel with chain length  $\tilde{N}$  is simply given by the pmf  $p(N) = \delta_{N,\tilde{N}}$ , where  $\delta_{i,j}$  is the Kronecker delta.



where  $0 < a < 1$  is a fit parameter for a given gel and  $N \in \mathbb{N}$  is the number of monomers per chain. An illustration of the corresponding probability mass function can be found in Figure 3.11.

For demonstration purposes we also investigate a Poisson distribution  $p_\mu(N) = \exp(-\mu) \frac{\mu^N}{N!}$ , where  $\mu > 0$  is the average value  $E(N) = \mu$  and the variance  $\text{Var}(N) = \mu$ . This narrow distribution of chain lengths is for example obtained via chain polymerizations [59]. Finally, we also investigate the distribution that was used by [93]:

$$p_{N_{\text{short}}, N_{\text{medium}}, N_{\text{long}}}(N) = \begin{cases} 1/8 & \text{if } N=N_{\text{short}} \\ 3/4 & \text{if } N=N_{\text{medium}} \\ 1/8 & \text{if } N=N_{\text{long}} \\ 0 & \text{else.} \end{cases} \quad (3.34)$$

For the different chain lengths which occur in this probability mass function, we have the restriction  $\frac{1}{2}(N_{\text{short}} + N_{\text{long}}) = N_{\text{medium}}$  [93]. We always choose  $N_{\text{short}} = 0.5N_{\text{medium}}$  and  $N_{\text{long}} = 1.5N_{\text{medium}}$  like Edgecombe et al.

Using the geometrical pmf, the Poisson pmf or the Edgecombe pmf we weight the contributions of cells with different polymer chain lengths to predict the (mass-based) degree of swelling of the gel: The degree of swelling for a polydisperse gel is given via the following ratio

$$\langle Q_m \rangle_N = \frac{\langle m_{\text{solvent uptake}} \rangle_N}{\langle m_{\text{dry}} \rangle_N}, \quad (3.35)$$

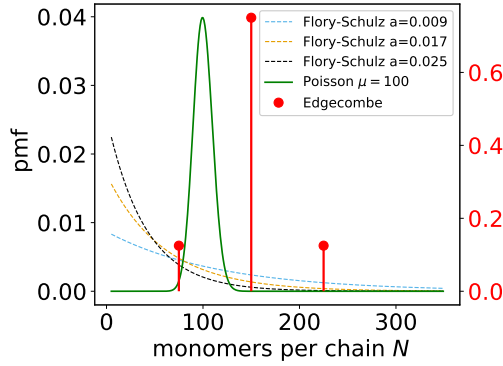


Figure 3.11: Different probability mass functions which we use in this thesis: the geometrical distribution (Flory-Schulz), the Poisson distribution and the distribution in accordance with Edgcombe [93]. The Flory-Schulz distribution is shown for different parameters  $a$ . The pmfs are only defined for integer values  $N$ , the lines serves only as a guide to the eye. The three shown values of the parameter  $a$  are the minimally used  $a$ , the maximally used  $a$  and the median of the used values of  $a$ . The values of  $a$  which we chose, all guarantee that at least 90 % of the chains have a chain length between  $N = 5$  and  $N = 350$  for which we have data  $R_{eq}(N)$  (see Figure 3.6). This means we choose values of  $a$  such that  $\sum_{N=5}^{350} p_a(N) > 0.9$ . Note that the distribution from Edgcombe is only nonzero for three values of  $N$  and therefore the probability for those values is larger than usual compared to the other distributions. Therefore, the pmf of Edgcombe has its own ordinate axis in red.

where the dry mass of the gel is:

$$\langle m_{dry} \rangle_N = \sum_N p_a(N) m(N) N_{chains},$$

where  $m(N) = N \cdot m_0$  and  $N_{chains}$  are as before. The mass of the

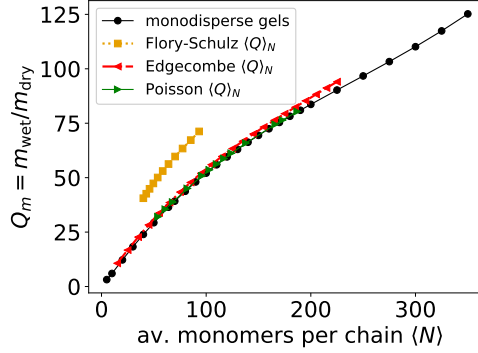


Figure 3.12: PB CGM prediction (for  $f = 0.5$ ,  $c_{\text{salt}}^{\text{res}} = 0.1 \text{ mol/L}$ ,  $\epsilon_r = 80$ ): The figure shows the (mass-based) degree of swelling  $Q_m$  as a function of the average chain length  $\langle N \rangle$ . The results for different monodisperse gels are shown in black. For the same charge fraction and reservoir salt concentration, the plot also shows the average mass-based degree of swelling  $\langle Q_m \rangle_N$  for polydisperse gels (orange, red, green curves) plotted over the average chain length  $\langle N \rangle_N$ .

solvent in the swollen state of the gel is similarly calculated:

$$\langle m_{\text{solvent uptake}} \rangle_N = \sum_N p_a(N) V_{\text{chain}}(N) \rho_w N_{\text{chains}},$$

where again  $\rho_w \approx 1 \text{ kg/l}$  and  $V_{\text{chain}}(N)$  is given by eq. (3.4) (see Figure 3.6 for values of  $R_{\text{eq}}(N)$ , for other values of  $N$  we use the linear interpolation in between those points). As before,  $N_{\text{chains}}$  cancels from the calculation of  $\langle Q_m \rangle_N$ .

In Figure 3.12 we compare the degree of swelling of monodisperse gels to polydisperse gels with the same average chain length. We find that the swelling of polydisperse gels highly depends on the chain length distribution. We observe an in-

creased degree of swelling for polydisperse gels which have a geometric chain length distribution. The fact that the introduced Flory-Schulz polydispersity increases the degree of swelling can be understood as an effect of the tail of the pmf: gels with longer chains swell more. Close to no increase in the degree of swelling is observed for a gel with a chain length distribution which is of Poisson type or follows the distribution by Edgecombe [93]. Because the Poisson distribution is rather sharp, it is expected [59] and observed in our simple model, that the polydispersity has only little influence on the mass based degree of swelling. We want to emphasize that [93] reported a decrease in the swelling of his polydisperse gel model compared to the monodisperse gel in contrast to our approach. This difference could be a result of strong correlations in their gel model originating basically from the small unit cell they consider - interchain correlations are overestimated. Additionally, it is not clear how different chain length heterogeneities like e.g. a Flory-Schulz distribution would impact the results reported by [93]. Representing a broad chain length distribution requires to simulate many chains in a unit cell, hence a huge computational effort. In contrast to the simulations of Edgecombe, our simplistic model for accounting chain length polydispersity lacks inter-chain correlations which seem to play an important role [108]. Measuring the correlations and accounting for them in simulations remain an open task for theorists as well as experimentalists [108]. We conclude that there is a discrepancy between the reported decrease in swelling by Edgecombe et al. for polydisperse gels and the data shown in Figure 3.12 for the chain length distribution of Edgecombe in our simple model. Our simplistic model for accounting chain length polydispersity lacks inter-chain correlations (in contrast

to the simulations of Edgecombe). Therefore, correlations between the stretching state of different chains in the gel seem to play an important role [108]. Correlations and special topological conditions in the gel cannot be taken into account in our simple model of polydispersity since we assume independent chains. Measuring the correlations and accounting for them in simulations remains an open task for theorists as well as experimentalists [108]. Please note that a non-affine deformation of the gel alters the equilibrium volume which is predicted by Equation (3.4). In the case of a non-affine deformation  $A$  is a function of the end-to-end distance. Therefore, non-affine deformations of the gel alter the prediction of the mass-based degree of swelling for monodisperse gels, as well as for polydisperse gels.

#### 3.6.7 Influence of the Different Imposed Charge Densities in the PB CGM

We now investigate the influence of the imposed charge densities in the PB CGM and exchange the rectangular monomer density with an approximately Gaussian monomer density with compact support. The choice of the monomer density affects the charge density  $\rho_f$  which is input to the PB equation.

If the probability density to find a monomer in a given distance  $r$  from the end-to-end vector is approximately Gaussian, then it is given via the following formula:

$$p(\vec{r}) = \mathcal{N}_2(1 + \cos(\omega r))H(-(r - \pi/\omega)). \quad (3.36)$$

$\mathcal{N}_2$  is a normalization constant such that  $p(\vec{r})$  is a probability

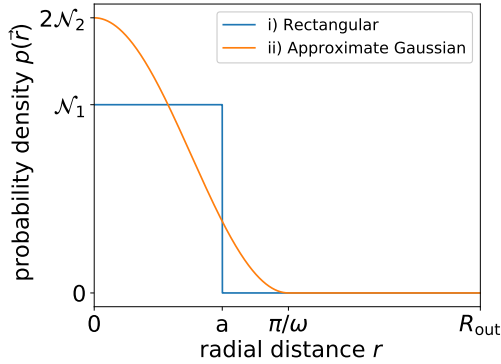


Figure 3.13: Different probability densities to find a monomer in distance  $r$  from the end-to-end vector which are used in the PB CGM. The figure shows i) the rectangular probability density and ii) the approximately Gaussian probability density.

density ( $\int_{V_{\text{chain}}} dV p(\vec{r}) = 2\pi L \int_0^R dr r p(\vec{r}) = 1$ ). This normalization criterion yields  $N_2 = \frac{2\omega^2}{-4+\pi^2} \frac{1}{2\pi L}$ . The parameter  $\omega$  is chosen such that  $\langle r \rangle \stackrel{!}{=} \langle r \rangle_{\text{MD}}$  is matched to the average distance of the monomers from the end-to-end vector. This condition yields  $\omega = \frac{2(-6\pi+\pi^3)}{3(-4+\pi^2)\langle r \rangle_{\text{MD}}}$  which determines the width of the probability density. A comparison between the approximately Gaussian probability density and the rectangular probability density to find a monomer in distance  $r$  can be seen in Figure 3.13.

Imposing this alternative monomer density and solving the PB CGM again for the resulting alternative choice of  $\rho_f(\vec{r}) = -Nf p(\vec{r})$ . We obtain only marginally changed swelling equilibria when imposing different monomer densities, see Figure 3.14 which barely allows to distinguish the resulting swelling equilibria.

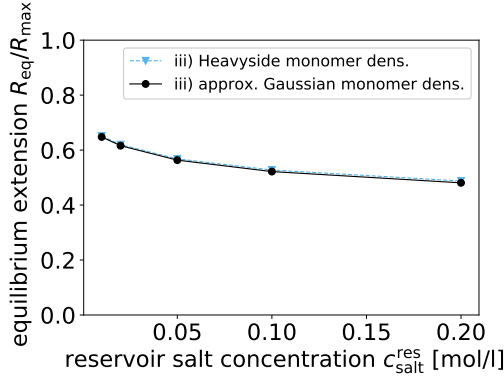


Figure 3.14: Comparison of the swelling for different monomer densities (rectangular or approximate Gaussian density) in the PB model. The equilibrium swelling length  $R_{\text{eq}}$  as a function of the reservoir salt concentration  $c_{\text{salt}}^{\text{res}}$  for  $f = 1$ ,  $\epsilon_r = 80$  and  $N = 40$ .

### 3.6.8 Influence of the Different Imposed Values of $A$

Košovan et al. [3] investigated the relation between the end-to-end distance and the volume per chain. They found (their figure 10) in MD simulations of periodic gels that the ratio  $A = R_e^3/V_{\text{chain}}$  varies between roughly 1.8 and 1.5 and depends on the compression state of the gel, the charge fraction of the gel and the salt concentration of the reservoir. This fact is in contrast to our two new models where  $A = \sqrt{27}/4 \approx 1.3$  is fixed.

The easiest approach to test the influence of  $A$  on our models is to impose a value of  $A = 1.8$  and compare it to results where  $A$  was chosen to be  $\sqrt{27}/4$ . The absence of a significant change of

the predicted swelling equilibria when a changing the value of  $A$  be seen in Figure 3.15.

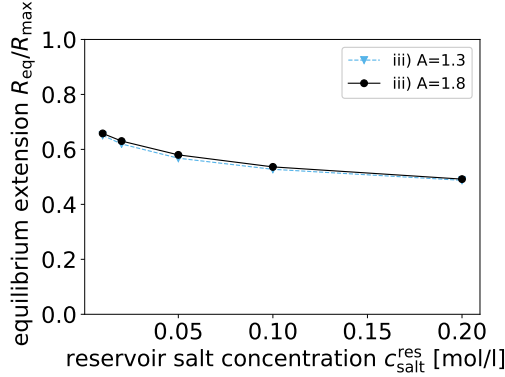


Figure 3.15: Comparison of different values of  $A$  in the PB model (for the rectangular charge distribution). The equilibrium swelling length  $R_{\text{eq}}$  as a function of the reservoir salt concentration  $c_{\text{salt}}^{\text{res}}$  for  $f = 1$ ,  $\epsilon_r = 80$  and  $N = 40$ .

We conclude that the value of the end-to-end distance  $R_{\text{eq}}$ , predicted by the PB CGM, is not sensitive to a change of the exact value of the ratio  $A$ : The predicted swelling equilibria barely change on a change of  $A$ . However, the predicted volume per chain is quite sensitive to the value of  $A$  through Equation (3.4):

## 3.7 Summary

In summary, we have presented two successive mean-field models aimed at describing gel swelling and the elastic moduli of polyelectrolyte gels: the single-chain CGM and the Poisson-Boltzmann CGM. We find that the single-chain CGM provides



an excellent agreement with the periodic gel model. Since it is particle-based, we can use exactly the same interactions as in the periodic gel model, and hence also investigate specific ion effects (modeled via different short range interactions), poor solvent conditions, or the influence of multivalent ions. The single-chain CGM provides about one order of magnitude reduction of the computational cost due to the smaller number of particles that need to be simulated.

In the next model we replaced the charged single-chain and all ions by suitable charge distributions and use the PB framework to derive the equilibrium cylindrical cell length. The PB CGM and the Katchalsky model provide several additional orders of magnitude in speed-up compared to the single chain model. On one hand, this speed-up comes at the cost of reduced accuracy. On the other hand, computationally cheaper models allow to screen the possible parameter space, needed for optimizing real-world applications, more efficiently. While the Katchalsky model fails for charge fractions  $f > 0.5$ , our new PB CGM still works for highly charged gels. The results for the bulk modulus of the single-chain CGM and the PB CGM are consistent with periodic gel results (within errorbars). Additionally, we explore gel swelling as a function of solvent permittivity. For large relative permittivities the ideal Donnan prediction is recovered, while for lower relative permittivities electrostatic correlations lead to the expected deviations between the PB CGM and the periodic gel model. Nevertheless, our single-chain CGM can still capture these correlation effects correctly. In addition, we demonstrated a simplistic approach of introducing chain length heterogeneity by assuming a mean-field factorization of the gel into uncorrelated single chain cells. In Chapter 6, the periodic

gel model, the single-chain CGM and the PB CGM are further generalized to also describe polyelectrolyte gels containing weak acidic or basic groups.

---

## 4 Comparison with Experiment

The work detailed in this chapter was published earlier. The results are part of the following publication:

L. Arens, D. Barther, **J. Landsgesell**, C. Holm, M. Wilhelm.  
“Poly (sodium acrylate) hydrogels: Synthesis of various network architectures, local molecular dynamics, salt partitioning, desalination and simulation” In: *Soft Matter* (2019)  
URL: [https://dx.doi.org/ 10.1039/C9SM01468C](https://dx.doi.org/10.1039/C9SM01468C)

The aim of the work presented in this chapter is to compare the swelling properties of single and interpenetrating gels to the PB cell-gel model (see Section 3.5) and periodic gel MD simulations. Interpenetrating networks (IPNs) can be produced via swelling a single network (SN) in a solution of monomers and then initializing a second cross-linking process. An example for such an interpenetrating network is depicted in Figure 4.2. IPNs show modified mechanical properties, which makes them e.g. interesting for mechanical actuators [120] like the osmotic engine [12]. Comparing our simulations to experiments helps to evaluate their validity.

## 4.1 Experiments

The synthesis of the SN and IPN polyacrylic acid gels as well as the experiments were performed by Lukas Arens at the Karlsruhe Institute of Technology. As outlined in [116], various IPNs and SNs were synthesized with varying degrees of cross-linking (DC). These gels were then used in the experiments as depicted in Figure 4.1:

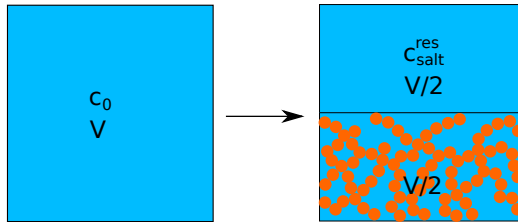


Figure 4.1: In the experiments dry gel is added to the solution with initial salt concentration  $c_0$  until the gel takes half the volume  $V$  of the chamber. Then the salt concentration in the supernatant phase is  $c_{\text{salt}}^{\text{res}}$  and the salt concentration in the gel phase is  $c_{\text{salt}}^{\text{gel}}$ .

A salt solution of given (initial) salt concentration  $c_0$  is placed in a chamber of volume  $V$ . Then additional dry polymeric gel is added until the gel volume  $V^{\text{gel}}$  and the volume of the supernatant salt solution  $V^{\text{res}}$  are half the volume of the chamber  $V^{\text{gel}} = V^{\text{res}} = V/2$ . The relative increase in salt concentration (“salt rejection”) in the supernatant solution and the gel swelling is recorded.

## 4.2 Simulations

We use the Poisson-Boltzmann cell-gel model (CGM), previously presented in chapter 3, for the prediction of the salt partitioning and the swelling equilibrium of SN. The basic simulation protocol is the same as in Chapter 3.

For IPNs, it is not directly obvious how to apply the PB CGM to the problem. However, it is straight forward to perform MD simulations of IPNs: we first set up a single, diamond-like gel and then replicate it, shifted by half the box length in each Cartesian direction. A screenshot of the resulting interpenetrating gels can be found in Figure 4.2, which are similar to the ones previously investigated by Edgecombe et al. [121].

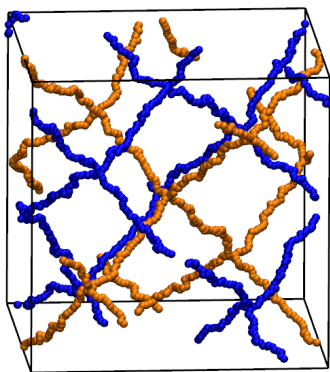


Figure 4.2: Simulation setup of two interpenetrating diamond-like gels (first gel is in orange the second gel is in blue).

The simulation protocol is equivalent to the one given previously for the MD simulations of (single) periodic gels in Section 2.5.4.

Because we simulated Poly(acrylic) acid in contact with an aqueous solution at  $\text{pH} = 7$  we choose the gel monomers to be fully negatively charged ( $f = 1$ ). At  $\text{pH} = 7$  the  $\text{H}^+$  and  $\text{OH}^-$  concentrations are very low and can, therefore, be safely neglected in our simulations.

The single and interpenetrating gels are simulated for a fixed chain length of  $N = 40$  and various salt concentrations in the supernatant phase  $c_{\text{salt}}^{\text{res}} \in \{0.01, 0.02, 0.05, 0.1, 0.2\} \text{mol/L}$ . These salt concentrations are imposed grand-canonically [102, 122, 3]. The initial salt concentrations  $c_0$  are calculated using Equation (4.5), making use of the resulting salt concentrations inside the gel  $c_{\text{salt}}^{\text{gel}}$ . At each imposed volume  $V^{\text{gel}}$  we then record the virial pressure inside the gel  $P_{\text{in}}(V^{\text{gel}})$ . In order to find the swelling equilibrium of the gel we simulate the gel at different volumes and record pressure volume curves. We then find the equilibrium swelling via balancing the pressure in the gel with the pressure of the bath, see Equation (3.2).

### 4.3 Mapping of Simulations to Experiments

The two experimental observables measured by Arens et al. [116] which we want to reproduce in simulations are the following:

- The mass-based degree of swelling  $Q_m$  as a measure for the degree of swelling. It is defined as the mass of the solvent in the swollen gel (in free swelling equilibrium) divided by

the mass of the dry gel:

$$Q_m = m_{\text{swollen}}/m_{\text{dry}} \quad (4.1)$$

- The salt rejection:

$$\text{SR} = \frac{c_{\text{salt}}^{\text{res}} - c_0}{c_0}, \quad (4.2)$$

where  $c_{\text{salt}}^{\text{res}}$  is the salt concentration in the supernatant phase and  $c_0$  the initial salt concentration prior to inserting dry polymer into the solution.

### Mapping of the Mass-Based Degree of Swelling

For comparison with experimental results, we need to introduce a mapping from the predicted end-to-end distances  $R_{\text{eq}}$  to the mass the gel has in swelling equilibrium. This is important since the experiments report the degree of swelling  $Q_m$  as a fraction of the mass of the water in the swollen state divided by the mass of the dry polymer. As before, in Section 3.6.5, we have to introduce some assumptions for mapping our simulation results to the mass based degree of swelling. First, the mass of the gel in the dry state is determined by the number of monomers  $N$  in the gel and the mass of the sodium acrylate monomers  $m_0 = 94$  u:

$$m_{\text{dry}} = N \cdot m_0, \quad (4.3)$$

We can measure the mass of the water in the swollen gel via the volume of the gel and an approximate density which is close to

that of pure water  $\rho_w \approx 1 \text{ kg/l}$ :

$$m_{\text{swollen}} = V_{\text{eq}}(N)\rho_w, \quad (4.4)$$

where  $V_{\text{eq}}(N) = (R_{\text{eq}}(N) + b)^3/A$  is the volume of the gel which is predicted by the PB CGM.

### Mapping of Initial Salt Concentrations

An important difference to the experiment is that we cannot directly obtain information about the gel swelling for a given initial salt concentration of the salt solution  $c_0$  because our models always take  $c_{\text{salt}}^{\text{res}}$  as input parameter: we impose the concentration of the supernatant solution  $c_{\text{salt}}^{\text{res}}$  when the gel is swollen. In order to make contact with the experiment, we need to find a mapping of salt concentration in the supernatant solution  $c_{\text{salt}}^{\text{res}}$  and the initial salt concentration prior to inserting the gel  $c_0$ : Key to relate both concentrations with each other is the law of particle number conservation. The number of salt ion pairs in the initial salt solution (in the volume  $V$ ) is given by  $N_{\text{salt}} = c_0 V$ , and it needs to be conserved in the whole process of adding dry gel to the initial volume<sup>1</sup>. Therefore, the number of salt ion pairs in the supernatant phase  $N_{\text{salt}}^{\text{res}}$  and the number of salt ion pairs in the gel phase  $N_{\text{salt}}^{\text{gel}}$  sum up to the total number of ion pairs  $N_{\text{salt}} = N_{\text{salt}}^{\text{gel}} + N_{\text{salt}}^{\text{res}}$ . The numbers in the respective gel or supernatant phase can again be calculated from the respective salt concentrations and volumes of these phases:  $N_{\text{salt}}^{\text{gel}} = c_{\text{salt}}^{\text{gel}} V_g = c_{\text{salt}}^{\text{gel}} V/2$  and  $N_{\text{salt}}^{\text{res}} = c_{\text{salt}}^{\text{res}} V^{\text{res}} = c_{\text{salt}}^{\text{res}} V/2$ . Plugging

---

<sup>1</sup>We assume that the change in volume  $V$  is negligible  $\Delta V \approx 0$  in the process of adding the dry gel to the initial salt solution.



these particle numbers in the equation for the particle number conservation gives:

$$N_{\text{salt}} = c_0 V = \frac{c_{\text{salt}}^{\text{gel}} V}{2} + \frac{c_{\text{salt}}^{\text{res}} V}{2} \Leftrightarrow c_0 = \frac{c_{\text{salt}}^{\text{gel}} + c_{\text{salt}}^{\text{res}}}{2}. \quad (4.5)$$

We use the formula above for calculating the initial salt concentration  $c_0$  based on  $c_{\text{salt}}^{\text{gel}}$  and  $c_{\text{salt}}^{\text{res}}$ . Therefore we calculate the salt rejection via:

$$SR(c_0) = \frac{c_{\text{salt}}^{\text{res}} - c_{\text{salt}}^{\text{gel}}}{c_{\text{salt}}^{\text{res}} + c_{\text{salt}}^{\text{gel}}}. \quad (4.6)$$

The salt concentration inside a negatively charged gel is the number of negatively charged mobile ions<sup>2</sup> per volume:

$$c_{\text{salt}}^{\text{gel}} = \frac{1}{V} \int_V d^3 r c_{-}(\vec{r})$$

Since we want to simulate at a fixed initial salt concentration, we vary the supernatant salt concentration  $c_{\text{salt}}^{\text{res}}$  imposed in the model until we conserve  $c_0$  at each point in the PV curve. The swelling equilibrium is then given by the point where the pressure of the supernatant phase equals the pressure of the gel phase [102, 2].

---

<sup>2</sup>We use the concentration of the negatively charged ions (instead of the concentration of positively charged ions), in order to not count the positively charged counterions, which we do not count as salt.

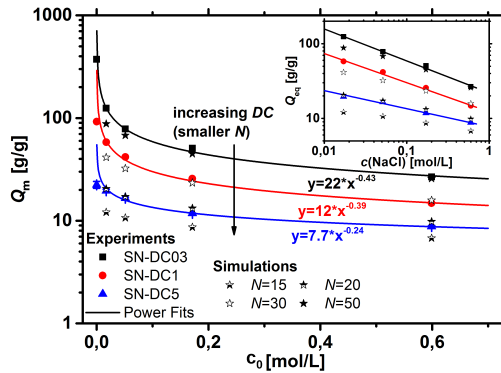


Figure 4.3: The dependency on the initial NaCl concentration of the degree of swelling is shown for three differently crosslinked SN hydrogels. Power functions describe this behavior well, as seen in the double logarithmic plot in the inset. Additionally, data from the PB CGM simulations with various chain lengths are shown as stars. The comparison of both data sets is given in the text. In the legend DC stands for degree of cross-linking. “DC03” means that the crosslinker density is 0.3 mol%. The higher the degree of cross-linking, the shorter the chains in the gel.

## 4.4 Single Networks

### 4.4.1 Salt Concentration Dependence of the Swelling Equilibrium

In Figure 4.3 the dependence of the swelling equilibrium on the initial salt concentration is shown. We find the known result that the degree of swelling decreases with increasing salt concentration (compare discussion of Figure 3.5b). This is explained by the increased electrostatic screening at higher salt concentrations. The trend predicted by the PB CGM agrees with

the experimental data. We give a discussion of possible deviations between experiment and simulations in Section 4.6. The inset in Figure 4.3 shows the same data in a double logarithmic plot. Both, the experimental data and the simulation data form lines in this plot, which means that they exhibit a power law behavior. For clarity, we added power law fits  $Q_m = A \cdot (c_0)^b$  with prefactor  $A$  and exponent  $b$  to the experimental data (solid lines). A power law behavior for the degree of swelling is expected for the dependence of the degree of swelling on the reservoir salt concentration [101, 123]. We observe different scaling exponents  $Q_m \propto c_0^b$ , with  $b \in \{-0.24, -0.39, -0.43\}$ . The theory on gel swelling by Barrat et al. [101, Eq. 3] predicts  $R_{eq} \propto c_{salt}^{res -1/5}$ , i.e.  $Q_m(c_{salt}^{res}) \propto V_{eq} \propto R_{eq}^3 \propto c_{salt}^{res -3/5}$ . Assuming validity of Equation (4.5) for the given experimental setup and using Equation (2.83), we can rewrite the initial salt concentration  $c_0$  as a function of  $c_{salt}^{res}$ .

$$c_0 = \frac{(\alpha + 4)}{2(\alpha + 2)} c_{salt}^{res}$$

For a fully charged gel we have a degree of dissociation  $\alpha = 1$  and the equation further simplifies to

$$c_0 = \frac{5}{6} c_{salt}^{res}.$$

Based on Barrat's theory we, therefore, expect  $Q_m \propto c_{salt}^{res -3/5} \propto c_0^{-3/5}$ , i.e. a scaling exponent of  $-3/5 = -0.6$ . On the other hand, Mussel et al. [123] reported that the degree of swelling scales with salt concentration with an exponent  $-0.47 \pm 0.03$ . Comparing the scaling exponents reported in Figure 4.3 to the ones reported by Barrat or Mussel, we observe deviations. Regarding Barrat's theory we want to remark that the scaling of  $R_{eq} \propto c_{salt}^{res -1/5}$  is not

always reproduced in our periodic gel MD simulations presented in Chapter 3 which we expect to be quite reliable: Fitting a power law to the periodic gel MD data underlying Figure 3.5b, we obtain  $R_{\text{eq}}(c_{\text{salt}}^{\text{res}}, N = 64, f = 0.5) \propto c_{\text{salt}}^{\text{res} - 0.19}$ , however, fitting a power law to the periodic gel MD data of a gel with shorter chains, we obtain for example  $R_{\text{eq}}(c_{\text{salt}}^{\text{res}}, N = 40, f = 0.125) \propto c_{\text{salt}}^{\text{res} - 0.12}$ . It therefore, seems adequate to not expect Barrat's scaling law to hold strictly — in the end it is an idealized model. In the light of the periodic gel MD data the reported variation in the scaling exponents in Figure 4.3 seems possible.

### 4.4.2 Chain Length Dependence of the Salt Rejection

The salt partitioning of three SN hydrogels with different degree of cross-linking (DC) was studied in differently concentrated NaCl solutions (in the range of  $c_0 \in [0.017 \text{ mol/L}, 0.6 \text{ mol/L}]$ ). The results are displayed in Figure 4.4, where we show the parametric plot of the salt rejection  $SR(N)$  as a function of the degree of swelling  $Q_m(N)$  (for different initial salt concentrations  $c_0$ ). There are two main trends observed in the PB CGM simulations and the experiments:

- the gels have a higher salt rejection at lower salt concentration  $c_0$
- the the gels have a higher salt rejection for shorter chains, i.e. increasing degree of cross-linking.

The simulations show qualitatively the same trend as the experimental data. Quantitatively, however, the simulations deliver

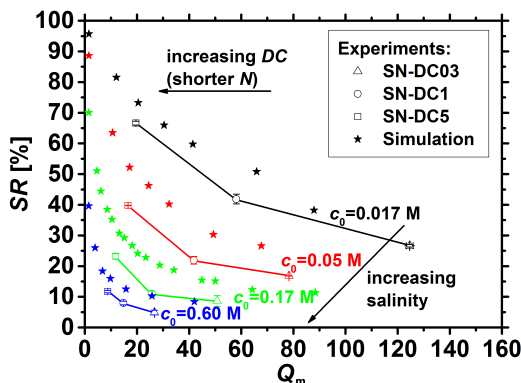


Figure 4.4: Comparison of the salt rejection SR of three SN hydrogels with varying degree of cross-linking (open symbols) in differently concentrated NaCl solutions as a function of the degree of swelling. The simulation data are shown as stars and overestimate the SR, possible reasons are given in Section 4.6.

always higher SR values compared to the other data points, where the deviations become larger at low polymer concentrations and high initial salt concentrations. For a list of possible explanations for the deviations we refer to Section 4.6.

## 4.5 Interpenetrating Networks

The degree of swelling of a fully charged polyacrylic acid SN and IPN was studied for different initial salt concentrations. The molar ratio of the first to the second network in the IPN is about 1:1.

The water uptake of the IPNs decreases compared to the precursor

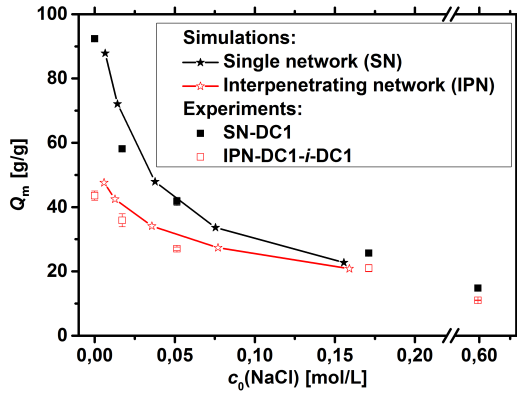


Figure 4.5: The degrees of swelling of (fully charged) simulated double and single networks are shown for different initial NaCl concentrations as stars. The water absorbency of the SN is much higher at low concentrations, whereas the difference in the swelling behavior becomes smaller for higher salt concentrations. The MD simulations are qualitatively in good agreement when compared with the experimental data which are shown as squares

single networks (SN), since the incorporation of the second polymer causes more constraints of the chains due to additional network entanglements. This is the case for the IPN in the experiment as well as in the MD simulations: Gel nodes within one network are restricted in their freedom to move due to the presence of the other network. The difference of the water absorbency is very pronounced in deionized water (the IPN swells about a factor of 2.5 less), while the degrees of swelling become very similar in higher concentrated solutions as seen in Figure 4.5. This trend is consistent across all charge fractions  $f \in \{0.125, 0.25, 0.5, 1\}$  (see appendix 8.4).

## 4.6 Possible Reasons for Deviations Between Experiments and Simulations

In figures 4.3, 4.4, 4.5 we observe various deviations between simulation data and experimental data. There are multiple reasons why these deviations occur.

- The simulations are based on a monodisperse network, where all chains have the same length and where the crosslinker is not explicitly modeled. However, the experimental samples were synthesized by free radical polymerization and thus have a broad distribution of monomer units between two cross-linking points. Simulation results in Section 3.6.6 indicate that a broader distribution of chain lengths could lead to a higher degree of swelling when an asymmetric distribution with a positive skewness is present in the gel.
- The average chain length in the gel is expected to be  $N = (1 - 1/f_c) \frac{1}{DC \cdot k}$ , where  $f_c = 4$  is the crosslinker functionality,  $DC$  the crosslinker density and  $k$  the crosslinker efficiency which varies between 15% and 78%. Since the crosslinker efficiency is unknown, it is not clear what average chain length should be used in the simulations. Determining the crosslinker efficiency is still an open problem.
- Different side reactions, e.g. chain transfer, lead to additional chemical cross-linking points reducing the effective chain length of the gels.

- Intermolecular entanglements between chains can act as additional non-fixed cross-linking points, further reducing the effective number of monomer units per chain. This effect becomes more pronounced if more monomers are present between two cross-linking points. Entanglements (uncaptured in the PB CGM) would result in a reduced degree of swelling compared to the PB CGM prediction.
- In the simulations, the dielectric constant of water was assumed to be constant at  $\epsilon_r = 80$ . However, the dielectric constant changes with the salt concentration and especially with the degree of swelling, as the electric environment in a charged hydrogel depends strongly on its charge density. Thus, each data point has a slightly different dielectric constant depending on  $Q_m$  and the initial salt concentration. Furthermore, water molecules in the hydrogel might orient close to the charges, which results in different local dielectric constants on a microscopic level. A reduced local dielectric constant would in tendency increase the number of condensed ions, therefore collapsing the gel.
- The PB CGM assumes affine deformation of the gel. It was reported that already periodic gels in MD simulations do not deform affinely, which results [1, p. 83] in  $A(R_e) \in [1.5, 1.8]$ . This would mean that the PB CGM predicted gel volume (assuming  $A = \sqrt{27}/4 \approx 1.3$ ) could be too high by factor  $1.8/1.3 \approx 1.4$  (i.e. 40%)
- The degree of swelling  $Q_m$  was determined in an experiment which was different from the experiment which was used for determining the supernatant salt concentration  $c_{\text{salt}}^{\text{res}}$  (for determining the salt rejection  $SR$ ). It is possible



that the condition  $V^{\text{gel}} = V^{\text{res}} = V/2$  was not exactly obeyed. An error in the experiment would affect the results reported in figures 4.3, 4.4, 4.5. If the volume  $V^{\text{gel}}$  is smaller than  $V^{\text{res}}$  (and therefore  $V^{\text{gel}} \neq V^{\text{res}} = V/2$ ) in the swelling experiments, then the gel is swelling more than expected from simulations: The actually present salt concentration in the supernatant phase then increases less from the initial salt concentration  $c_0$  compared to the simulations. Therefore, the gel was in contact with a supernatant solution with lower salt concentration than assumed in the simulations. Therefore, the gels would swell more than expected from the simulation. If this error was present in the experiments, the obtained experimental data in Figure 4.3 are shifted to higher  $Q_m$ , a correction would shift the data down, towards the simulation data.

- The degree of swelling was experimentally determined by the ratio of absorbed water to dry polymer mass. However, the polyelectrolyte hydrogels are very hydrophilic and contain typically about 10 wt% of moisture. Therefore, the experimentally determined  $Q_m$  is about 10% too low (because it accounts for residual water). Instead the experimentally determined  $Q_m$  should be higher and all experimental data points in Figure 4.3 and 4.5 would be shifted upward by 10% if one accounted for the real dry polymer mass. Also in Figure 4.4 the experimental data would be shifted to higher  $Q_m$ .

In summary, there are multiple reasons for simulations and experiments not agreeing perfectly. An open problem is that the crosslinking structure of the gel used in the experiments is

random and a representative, average chain length is unknown. This problem can only be solved with better analysis of the experimentally realized crosslinking structure or crosslinkers which result in less random structures. On top of this uncertainty, it seems possible that a repeated, more controlled experiment for determining  $Q_m$  (where  $V^{\text{gel}} = V/2$  is strictly obeyed) could improve agreement with the simulations significantly. It seems, however, more reasonable to report the gel swelling  $Q_m$  as a function of the salt concentration in the supernatant solution. These data are straightly available from simulations but, unfortunately, not from the experiments as they were performed in [116]. Despite all these possible reasons for deviations our gel models can reproduce significant trends in the experimental data. Therefore, we conclude that the basic physical driving forces of gel swelling are incorporated in the models.

### 4.7 Summary

We have compared the periodic gel model and the PB CGM to experiments with poly(sodium acrylate) hydrogels with different network topologies such as single networks (SN) and interpenetrating double networks (IPN). The comparison was performed at  $\text{pH} = 7$  such that the gels can be treated as strong polyelectrolyte gels with charge fraction one. The swelling capacity of the gels in deionized water and sodium chloride solutions have been studied, where the absorbency  $Q_m$  decreased with higher salinities and more entanglements in the network caused by a higher degree of cross-linking or the incorporation of a second network. Simulations based on a PB cell model were used to describe

qualitatively the swelling behavior for differently crosslinked SN hydrogels. In general, the simulations overestimated  $Q_m$ , which can be ascribed to several simplifications that were made and to the rather undefined structure of the hydrogels synthesized via free radical polymerization. Furthermore, MD simulations showed in agreement with the experiments that the water absorbency of an IPN is much smaller at low salinities compared to its related SN, whereas the differences between both network types vanish at higher salt concentrations.



---

## 5 Grand-Reaction Method

The work detailed in this chapter is in part submitted as:

**J. Landsgesell**, P. Hebbeker, O. Rud, R. Lunkad, P. Košovan, C. Holm. “Grand-Reaction Method for Simulations of Ionization Equilibria and Ion Partitioning in a Broad Range of pH and Ionic Strength” In: *ChemRxiv* (2019)

URL: <https://doi.org/10.26434/chemrxiv.9741746.v2>

Reacting systems in contact with a supernatant solution (i.e. a reservoir) are ubiquitous in chemical research, especially in colloid and polymer science. Such a setup is widely used in applications to separate or purify substances [124], like in medicine [125, 126, 127] or water purification [128, 129, 130]. Other applications are osmotic motors [12], sensors [131] or simply *weak polyelectrolyte gels* (which we investigate in chapter 6). A schematic view of the systems we want to investigate is depicted in Figure 5.1.

The equilibrium state of the ionization reaction in such systems is determined by the pH and by the concentration of other ions in the system. The presence of charged polymers affects the partitioning of small ions between the system and the reservoir. The change in ion concentrations affect the reaction equilibrium,

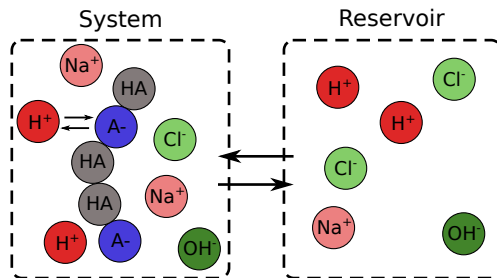


Figure 5.1: A system exchanging small ions with a reservoir. The macro-molecules inside the system take part in chemical reactions. Different colors represent different particle types. In total, the problem requires describing at least six particle types: four for the ionic species in the reservoir ( $\text{H}^+$ ,  $\text{OH}^-$ ,  $\text{Na}^+$ ,  $\text{Cl}^-$ ) and two additional types for the different ionization states of the monomers in the system ( $\text{HA}$ ,  $\text{A}^-$ ).

which in turn affects the ion partitioning in a non-trivial feedback loop.

This feedback loop cannot be captured using the constant pH method [48] or the reaction ensemble in its original formulation. The constant pH method cannot be applied due to the fact that it would need to be used with the pH value in the system containing an unknown Donnan-partitioning contribution  $\Delta$  (see Equation (5.8)). The reaction ensemble on the other hand needs to be enhanced by a grand-canonical simulation protocol and it turns out that this is not straight forward. We, therefore, introduce the grand-reaction method for coarse-grained simulations of acid-base equilibria in a system coupled to a reservoir at a given pH and concentration of added salt.

To perform a coarse-grained simulation of a reactive phase in equilibrium with a multi-component solution phase, we need to

solve two strictly separated tasks:

1. Prescribing the exact composition of the *reservoir*
2. Incorporating chemical reactions in the simulation of the *system*

The first task has its own challenges, related to the definition of pH, which is why we devote Section 5.1 to defining pH and describing the ionic strength in an aqueous solutions. In Section 5.2, we introduce an idealized Donnan model which allows to understand the main consequences of coupling a reactive system to a reservoir. In Section 5.3, we present how to faithfully represent a reservoir (defined by a pH value and reservoir salt concentration) with interacting particles. Using this reservoir, we can then impose chemical reactions in the system, which is done in Section 5.4. The approach we present there is aimed at avoiding sampling problems. Finally, the results for an example system of a weak polyelectrolyte solution, separated from the reservoir by a semipermeable membrane, are shown in Section 5.6. In the Chapter 6 we use the grand-reaction method, presented here, for describing weak polyelectrolyte gels.

## 5.1 pH and Ionic Strenght

pH is a measure for the chemical potential  $\mu_{\text{H}^+}$  of  $\text{H}^+$  and is defined by IUPAC [22] using the relative activity  $a_{\text{H}^+}$ :

$$\text{pH} = -\log_{10}(a_{\text{H}^+}) = -\log_{10}(c_{\text{H}^+} \gamma_{\text{H}^+} / c^\ominus), \quad (5.1)$$

with the mean activity coefficient<sup>1</sup>  $\gamma_{\text{H}^+} = \exp(\beta\mu_{\text{H}^+}^{\text{ex}})$ . The chemical potential of  $\text{H}^+$  and  $\text{OH}^-$  ions are coupled in aqueous solution via the auto-dissociation of water:

$$K_w = a_{\text{H}^+}a_{\text{OH}^-} = \frac{c_{\text{H}^+}\gamma_{\text{H}^+}c_{\text{OH}^-}\gamma_{\text{OH}^-}}{c^\ominus{}^2} = 10^{-14},$$

The variation of ionic strength with pH is depicted in Figure 5.2. The impact of pH on the ionic strength implies that even strong polyelectrolytes react to changes in pH due to a modified electrostatic screening. Therefore, a strong polyelectrolyte is more collapsed at extreme pH than around  $\text{pH} = 7$ , where the ionic strength is minimal.

In contrast to simulations of strong polyelectrolytes, where the species of particles are not important, the information about the species of a particle has to be resolved in simulations involving chemical reactions: Chemical reactions are by definition sensitive to the chemical potential of specific particle species (see the defining equation for the equilibrium constant (2.12)). An important part of the chemical potential of a species is the ideal part, mainly described by the concentration of the species. Therefore, this information has to be represented in simulations of weak polyelectrolyte solutions.

---

<sup>1</sup>If the mean activity coefficient is used in the definition of pH, then we use that the activity of  $\text{H}^+$  is defined by  $a_{\text{H}^+} = \exp(\beta(\mu_{\text{H}^+} - \mu_{\text{H}^+}^\ominus))$ , where we use  $\mu_{\text{H}^+} = \bar{\mu}_{\text{H}^+} - z_{\text{H}^+}e_0\psi$ , i.e. the total (electro-)chemical potential with the (mean) electric potential contribution subtracted (compare [132, 133]). The reason for this is, that the mean activity coefficient  $\gamma_{\pm} = \sqrt{\exp(\beta(\mu_+^{\text{ex}} + \mu_-^{\text{ex}}))}$  is defined using a sum of the excess chemical potential of a positive and a negative ion and therefore the electric potential contribution to the excess chemical potential is canceled, compare Section 2.5.3



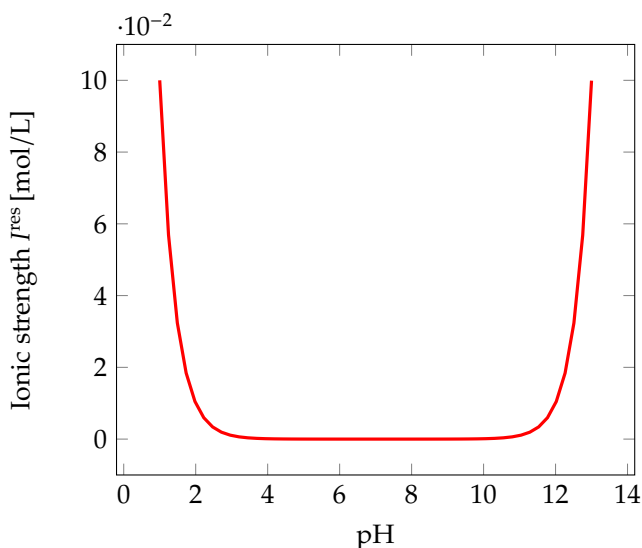


Figure 5.2: Schematic representation of ionic strength  $I^{\text{res}}$  in a salt free solution:  $I^{\text{res}}$  varies, when varying the pH of a solution by adding strong acid, to lower pH, or base, to increase pH.

#### Note 9

Note that it is always possible to distinguish whether a particle is of a given species or not. This is not in contradiction to the principle of indistinguishable particles: the principle just states that particles belonging to the same species cannot be distinguished.

In coarse-grained simulations it is common to neglect the chemical nature of a species if it has interactions which are, approximately, identical to another species. For example, when we deal with coarse-grained simulations of strong polyelectrolytes,

it is natural to ignore the fact that there is a certain amount of  $H^+$ ,  $Na^+$ ,  $OH^-$  and  $Cl^-$  ions, because the strong polyelectrolyte interacts with all ions of same charge in the same way. Therefore, only the resulting ionic strength is of importance. This insight allows to simplify the simulations and coarse grain the chemical nature of the ion species away so that one only has to speak about positive and negative ions.

## 5.2 Ideal Donnan Equilibrium in the Presence of Weak Acidic Groups

The Donnan model is the simplest model to understand dissociation equilibria in Donnan-partitioned systems since all particles are treated on an ideal level. We are interested in the pH response and, therefore, we have to deal with a reservoir containing at least four ion species (see Section 5.3 ). Compared to the system presented in note 2.6.2, the new system is more complicated: we need to prescribe the ion concentrations  $c_{Na^+}^{res}$ ,  $c_{Cl^-}^{res}$ ,  $c_{H^+}^{res}$ ,  $c_{OH^-}^{res}$ .

Additionally (as outlined in Note 10) the degree of dissociation of a weak polyelectrolyte gel depends on the  $H^+$  concentration in the gel (i.e. the ion partitioning) and the value of  $pK$ :

$$\alpha = \frac{1}{1 + 10^{pK} c_{H^+}^{sys}}. \quad (5.2)$$

### Note 10

Chemical equilibrium is determined by the equilibrium

## 5.2 Ideal Donnan Equilibrium in the Presence of Weak Acidic Groups

constant  $K$ . This has profound consequences which we want to discuss here. We start by recalling the definition (Equation (2.12)) of equilibrium constant  $K$  and the definition of the chemical potential in (ideal) Donnan-partitioned systems (Equation (2.82)):

$$K = \prod_i a_i^{\nu_i} = \prod_i \exp(\beta(\mu_i - \mu_i^\ominus)) \quad (5.3)$$

$$\mu_i = \mu_i^\ominus + k_B T \ln(c_i/c^\ominus) + z_i e_0 \psi. \quad (5.4)$$

The chemical potential is the same in the reservoir and the system (Equation (2.81)). For the example of a weak acid the dissociation constant equals:

$$K = \frac{c_{A^-}^{\text{sys}}/c^\ominus \exp(-\beta e_0 \psi^{\text{sys}}) c_{H^+}^{\text{sys}}/c^\ominus \exp(\beta e_0 \psi^{\text{sys}})}{c_{HA}^{\text{sys}}/c^\ominus} \quad (5.5)$$

$$= \frac{c_{A^-}^{\text{sys}} c_{H^+}^{\text{sys}}}{c_{HA}^{\text{sys}} c^\ominus}. \quad (5.6)$$

We now make use of the fact that the chemical potentials are equal in the system and the reservoir (Equation (2.81)) which allows us to rewrite  $c_{H^+}^{\text{sys}} = c_{H^+}^{\text{res}} \exp(-\beta e_0 \psi^{\text{sys}})$  (if the reservoir potential is set to zero per convention  $\psi^{\text{res}} = 0$ , in which case we also know  $\text{pH} = -\log_{10}(\exp(\beta(\mu_{H^+}^{\text{res}} - \mu_{H^+}^\ominus))) = -\log_{10}(c_{H^+}^{\text{res}}/c^\ominus)$ ). Therefore, we have  $c_{H^+}^{\text{sys}} = 10^{-\text{pH}} c^\ominus \exp(-\beta e_0 \psi^{\text{sys}})$ . Defining  $\Delta := \log_{10}(\exp(-\beta e_0 \psi^{\text{sys}}))$ , we have:

$$K = \frac{c_{A^-}^{\text{sys}} 10^{-\text{pH} + \Delta}}{c_{HA}^{\text{sys}}}. \quad (5.7)$$

We can rearrange for  $\alpha = c_{A^-}^{\text{sys}} / (c_{A^-}^{\text{sys}} + c_{HA}^{\text{sys}})$ , resulting in:

$$\alpha = \frac{1}{1 + 10^{pK - \text{pH} + \Delta}} = \frac{1}{1 + 10^{pK} c_{H^+}^{\text{sys}}}. \quad (5.8)$$

This means that the Donnan-partitioning creates a shift  $\Delta$  [134] in the dissociation behavior compared to equation 2.18. This shift  $\Delta$  can take values of several pH units — as an example with corresponding discussion we refer to Figure 5.4.

The main take away is, that it is not sufficient to know the pH of the reservoir to determine the dissociation behavior of the weak groups in the system. Equation (5.8) differs from Equation (2.18), which was obtained for an ideal solution of weak acids, i.e. without considering Donnan-partitioning.

The ion partitioning and the degree of dissociation (five variables) are obtained by solving the following five equations:

$$\text{Donnan-partitioning: } \frac{c_{Na^+}^{\text{sys}}}{c_{Na^+}^{\text{res}}} = \frac{c_{H^+}^{\text{sys}}}{c_{H^+}^{\text{res}}} = \frac{c_{Cl^-}^{\text{res}}}{c_{Cl^-}^{\text{sys}}} = \frac{c_{OH^-}^{\text{res}}}{c_{OH^-}^{\text{sys}}} \quad (5.9)$$

$$\text{Electroneutrality: } \alpha c_0 + c_{Cl^-}^{\text{sys}} + c_{OH^-}^{\text{sys}} = c_{H^+}^{\text{sys}} + c_{Na^+}^{\text{sys}} \quad (5.10)$$

$$\text{Chemical equilibrium: } \alpha = \frac{1}{1 + 10^{pK} c_{H^+}^{\text{sys}}}, \quad (5.11)$$

where  $c_0$  is the monomer concentration.

Note that the autodissociation constant of water is satisfied in the system due to the fact that we imposed this condition for the

## 5.2 Ideal Donnan Equilibrium in the Presence of Weak Acidic Groups

---

reservoir concentrations (similar to notes 11 and 12):

$$\frac{c_{\text{H}^+}^{\text{sys}} c_{\text{OH}^-}^{\text{sys}}}{c^{\ominus 2}} = \frac{c_{\text{H}^+}^{\text{res}} c_{\text{OH}^-}^{\text{res}}}{c^{\ominus 2}} = K_w. \quad (5.12)$$

This simple model already allows to investigate the influence of the Donnan-partitioning on the dissociation behavior of e.g. a weak gel. Especially, we can ask for:

- the influence of the reservoir salt concentration on the degree of dissociation or
- the Donnan-partitioning induced shift  $\Delta$  (compare Equation (5.8)).

### Influence of the Reservoir Salt Concentration on the Degree of Dissociation

The degree of dissociation  $\alpha(c_{\text{salt}}^{\text{res}})$  varies as a function of the reservoir salt concentration (at fixed reservoir pH and monomer concentration  $c_0$ ): for pH = 6 and a polymer concentration of  $c_0 = 0.1\text{mol/L}$  this behavior is shown in Figure 5.3a.

The polyelectrolyte releases  $\text{H}^+$  ions, which are confined in the system due to the electroneutrality constraint. Increasing the reservoir salt concentration  $c_{\text{salt}}^{\text{res}}$ , more  $\text{H}^+$  ions are exchanged with the salt cation [112]. This is reflected in Figure 5.3a showing a decrease in  $c_{\text{H}^+}^{\text{sys}}$  with increasing concentration  $c_{\text{salt}}^{\text{sys}}$ . Due to the decreased concentration of  $\text{H}^+$  the reaction equilibrium adapts and the dissociation increases (red curve in Figure 5.3a). We will see in Section 6.3 that the dissociation response of weak

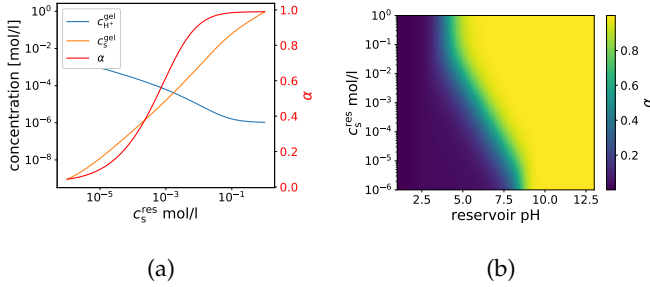


Figure 5.3: We show the response in the degree of dissociation of a system containing weak polyelectrolytes with fixed monomer concentration  $c_0 = 0.1$  mol/L. In figure a) concentrations  $c_{H^+}^{sys}$  and  $c_s^{sys}$ , as well as the degree of dissociation  $\alpha$  as a function of the reservoir salt concentration  $c_{salt}^{res}$  at fixed reservoir pH = 6 are shown. In figure b) the degree of dissociation as a function of pH and reservoir salt concentration  $c_{salt}^{res}$  is displayed.

polyelectrolytes on an increase in reservoir salt concentration gives rise to a non-monotonic swelling of gels.

The combined effect of pH and reservoir salt concentration on the degree of dissociation are shown in Figure 5.3b. From this figure, we also see that the degree of dissociation  $\alpha$  increases with increasing pH: Increasing the reservoir pH, reduces the reservoir concentration of  $H^+$  ions and due to the Donnan-partitioning (5.10) also the  $H^+$  concentration in the system. Due to Equation (5.2) this results in an increased degree of dissociation.

### Donnan-partitioning Induced Shift $\Delta$

Another interesting effect which can be studied using an ideal system is the Donnan-partitioning induced shift  $\Delta = \log_{10}(\exp(-\beta e_0 \psi^{sys}))$

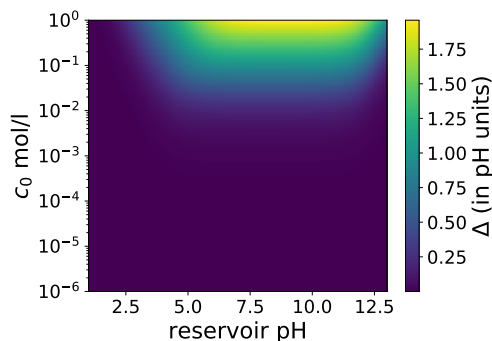


Figure 5.4: Numerical solution for the shift  $\Delta$  of an ideal Donnan-partitioned system with monomers having  $pK = 4$  and a reservoir salt concentration  $c_{\text{salt}}^{\text{res}} = 0.01 \text{ mol/L}$ .

(compare Equation (5.8)). Depending on the definition of  $pH$ ,  $\Delta$  could be interpreted as the shift in  $pH$  by which the  $pH$  in the system is lower than the reservoir  $pH$ . In Figure 5.4, we show this shift as a function of  $pH$  and monomer concentration  $c_0$  for monomers with  $pK = 4$  and reservoir salt concentration  $c_{\text{salt}}^{\text{res}} = 0.01 \text{ mol/L}$ . It is striking that this shift  $\Delta$  can be as big as several  $pH$  units. The Donnan-partitioning induced shift  $\Delta$  is always big when the charge density in the system is big compared to the ionic strength of the reservoir i.e. at  $pH > pK$  and at high monomer concentrations. At very high  $pH$  the reservoir ionic strength increases (due to the high amount of added base) and the Donnan shift decreases again.

Up till now we have only discussed the dissociation response of an ideal Donnan-partitioned system. Although discussing an ideal system helps to understand the general trends observed in interacting systems, we now elaborate how to perform simu-

lations of reacting interacting Donnan-partitioned systems. We start out with defining the reservoir in the case of an interacting system.

## 5.3 Reservoir with Interactions

In experiments the composition of the solution, which is in contact with the system, is typically specified by the dissolved amount of salt and the pH of the solution<sup>2</sup>. In this section we derive the chemical potentials of all particle species in the solution based on 1) the pH and 2) the salt concentration. As pointed out in note 1, there are two physical constraints our reservoir has to fulfill and two conditions with which we prescribe the reservoir composition:

1. macroscopic electroneutrality:  $\sum_i c_i z_i = 0$ .
2. water autodissociation:  $\text{H}_2\text{O} \xrightleftharpoons{K_w} \text{H}^+ + \text{OH}^-$ , with reaction constant<sup>3</sup>  $K_w := a_{\text{H}^+} a_{\text{OH}^-}$
3. pH which we want to observe in the reservoir
4.  $c_{\text{salt}}^{\text{res}}$  which we want to observe in the reservoir

Therefore, we have a set of four equations and four unknowns ( $c_{\text{H}^+}^{\text{res}}, c_{\text{OH}^-}^{\text{res}}, c_{\text{Na}^+}^{\text{res}}, c_{\text{Cl}^-}^{\text{res}}$ ) resulting in a unique solution.

---

<sup>2</sup>In controlled experiments the presence of carbon dioxide is excluded from the experiments [112, 135], since the reactions of carbon dioxide with water will create additional ionic species.

<sup>3</sup>The activity of water is almost always constant and therefore not accounted for in the reaction constant  $K_w$ .



### 5.3.1 Solving the Defining Equations for the Reservoir Composition

The four defining equations for the reservoir composition were presented above in the beginning of Section 5.3.

The second constraint in the enumeration given in Section 5.3 has profound implications. First, it states that in aqueous solutions  $H^+$  and  $OH^-$  ions are always present. The definition of the equilibrium constant (see Section 2.3) for the autodissociation reaction imposes that the product of the relative activities of  $H^+$  and  $OH^-$  ions is a constant:

$$K_w = a_{H^+} a_{OH^-} = \frac{c_{H^+} \gamma_{H^+} c_{OH^-} \gamma_{OH^-}}{c^{\ominus 2}} = 10^{-14},$$

where we have used that [136]  $K_w = 10^{-14}$ . This equation states that there are always  $H^+$  and  $OH^-$  ions (see note 11) and as a consequence also other ionic species  $Na^+$  and  $Cl^-$ , which are needed to fulfill the electroneutrality constraint.

#### Note 11

Forgetting the activity coefficients  $\gamma_{H^+} = 1$  and  $\gamma_{OH^-} = 1$  for a second, we can simplify the equation for the equilibrium constant of the autodissociation of water in the following way:

$$K_w \approx \frac{c_{H^+} c_{OH^-}}{c^{\ominus 2}} \Leftrightarrow c_{OH^-} \approx \frac{K_w c^{\ominus 2}}{c_{H^+}}.$$

This last equation implies that at low concentrations of  $H^+$  the concentration of  $OH^-$  is large and vice versa. As a consequence, the electroneutrality constraint cannot be

fulfilled by the  $H^+$  and  $OH^-$  ions alone: always other ions are needed to make the solution electroneutral:  $Na^+$  (if  $c_{OH^-} > c_{H^+}$ ) or  $Cl^-$  (if  $c_{H^+} > c_{OH^-}$ ). The point to remember is that our reservoir is composed by at least four ion species which we choose for convenience to be  $H^+$ ,  $OH^-$ ,  $Na^+$ ,  $Cl^-$ . Additional salt is modeled in our approach by  $Na^+Cl^-$ . The salt ions could be different from the neutralizing ions above, this would, however, only complicate the model.

In a solution with salt concentration  $c_{salt}^{res}$  the concentration of  $Na^+$  or  $Cl^-$  ions is given by:

$$c_{Na^+}^{res}(c_{salt}^{res}, c_{H^+}^{res}, c_{OH^-}^{res}) = \begin{cases} c_{salt}^{res} & c_{H^+}^{res} \geq c_{OH^-}^{res} \\ c_{salt}^{res} + (c_{OH^-}^{res} - c_{H^+}^{res}) & c_{H^+}^{res} \leq c_{OH^-}^{res} \end{cases} \quad (5.13)$$

$$c_{Cl^-}^{res}(c_{salt}^{res}, c_{H^+}^{res}, c_{OH^-}^{res}) = \begin{cases} c_{salt}^{res} & c_{OH^-}^{res} \geq c_{H^+}^{res} \\ c_{salt}^{res} + (c_{H^+}^{res} - c_{OH^-}^{res}) & c_{OH^-}^{res} \leq c_{H^+}^{res} \end{cases} \quad (5.14)$$

This choice ensures electroneutrality of the reservoir. Given the concentrations of  $OH^-$ ,  $H^+$  and the salt concentration  $c_{salt}^{res}$  in the reservoir, the reservoir concentrations are fully described.

The remaining problem is, however, that often the  $H^+$  concentration is not reported in experiments but rather the pH value:

$$pH = -\log_{10}(a_{H^+}) = -\log_{10}(c_{H^+} \gamma_{H^+} / c^\ominus),$$

with the mean activity coefficient  $\gamma_{H^+} = \exp(\beta \mu_{H^+}^{ex})$ . This adds further complication because the mean excess chemical potential

$\mu_{H^+}^{\text{ex}}(\{c_i^{\text{res}}\})$  is a function of the reservoir composition:

$$\mu_{H^+}^{\text{ex}}(\{c_i^{\text{res}}\}) = f(\{c_i^{\text{res}}\}).$$

As we show later in Section 2.5.3, the function  $f$  is non-trivial and depends on all interactions present in the reservoir. A further simplification can be made, if all our ions interact with the same interaction potentials. In this case, the excess chemical potential becomes a function of the ionic strength  $I^{\text{res}} = \frac{1}{2} \sum_i c_i^{\text{res}}$  because it does not depend on the exact reservoir composition. This means

$$\mu_{H^+}^{\text{res,ex}}(\{c_i^{\text{res}}\}) = f(I^{\text{res}}(c_{H^+}^{\text{res}}, c_{OH^-}^{\text{res}}, c_{\text{salt}}^{\text{res}})).$$

For the excess chemical potential as a function of ionic strength we use results shown in Figure 2.3 which we obtained via the Widom particle insertion method [18]. Knowing the function  $f(I^{\text{res}})$ , we proceed as following: Given the two inputs **pH** and  $c_{\text{salt}}^{\text{res}}$ , we can self-consistently solve the following equations for  $c_{H^+}^{\text{res}}$  and  $\mu_{H^+}^{\text{res,ex}}$  via a numerical scheme:

$$\text{pH} = -\log_{10}(c_{H^+}^{\text{res}} \exp(\beta \mu_{H^+}^{\text{res,ex}}) / c^\ominus) \quad (5.15)$$

$$\mu_{H^+}^{\text{res,ex}} = f(I^{\text{res}}(c_{H^+}^{\text{res}}, c_{OH^-}^{\text{res}}, c_{\text{salt}}^{\text{res}})) \quad (5.16)$$

$$c_{OH^-}^{\text{res}} = \frac{K_w c^\ominus^2 \exp(\beta \mu_s^{\text{res,ex}})}{c_{H^+}^{\text{res}}}, \quad (5.17)$$

where we used the pair excess chemical potential  $\mu_s^{\text{res,ex}}$  and the mean excess chemical potential  $\mu_{H^+}^{\text{res,ex}} = \mu_{OH^-}^{\text{res,ex}} := \mu_s^{\text{res,ex}}/2$  (see discussion on mean activity coefficients in Section 2.5.3).

After solving this set of equations numerically, we obtain  $c_{H^+}^{\text{res}}$  and  $\mu_{H^+}^{\text{res,ex}}$ . From these we can calculate  $c_{OH^-}^{\text{res}}$  (using Equation (5.17)) and then we obtain the remaining concentrations  $c_{Cl^-}^{\text{res}}, c_{Na^+}^{\text{res}}$  (using

equations (5.14) and (5.13)). The excess chemical potentials of all ions is the same ( $\mu_i^{\text{res,ex}}(I^{\text{res}}) = \mu_{\text{H}^+}^{\text{res,ex}}$ ), due to the ions having the same interactions. Together with the concentrations  $c_i^{\text{res}}$  this determines all chemical potentials  $\mu_i$  in the reservoir (see Section 2.5.3). Therefore, the reservoir chemical potentials are completely determined by the pH value and the salt concentration in the reservoir. As starting point for solving the equations we use the solution for  $f(I^{\text{res}}) \equiv 0$  (see also note 12).

A naive approach to determine the reservoir composition would neglect excess chemical potential contributions due to interactions in the system. In such a case, we would assign the reservoir concentration of  $\text{H}^+$  ions to  $c_{\text{H}^+}^{\text{res,naive}} := 10^{-\text{pH}} c^\ominus$ , the reservoir concentration of  $\text{OH}^-$  ions to  $c_{\text{OH}^-}^{\text{res,naive}} := 10^{-\text{pOH}} c^\ominus = 10^{-(\text{p}K_w - \text{pH})} c^\ominus$  and the  $\text{Na}^+$ ,  $\text{Cl}^-$  concentrations according to equations (5.13), (5.14). This would result in  $\text{H}^+$  concentrations being too low by up to approximately 30%, depending on the reservoir salt concentration (see Figure 5.5).

Since the excess chemical potential is negative (see Figure 2.3), the activity coefficients of the ions is  $\gamma_i = \exp(\beta\mu_i^{\text{res,ex}}) < 1$  and, therefore, the actual reservoir concentration  $c_{\text{H}^+}^{\text{res}}$  must be higher than the naively assumed  $c_{\text{H}^+}^{\text{res,naive}}$  in order to represent a certain  $\text{pH} = -\log_{10}(c_{\text{H}^+}^{\text{res}} \gamma_{\text{H}^+}^{\text{res}} / c^\ominus)$ . McCarty et al. demonstrate with various examples why it is important to include the mean activity coefficient  $\gamma_{\text{H}^+}$  in the definition of pH [137]. In table 5.1 we compare, for a given pH, the experimentally observed  $\text{H}^+$  concentrations to the ones we determine with the approach presented in this section and observe excellent agreement. Above and including  $\text{pH} = 1.1$  the deviation in  $c_{\text{H}^+}^{\text{res}}$  between our approach and the experiment is below 3%. At  $\text{pH} = 1.1$  the naive approach

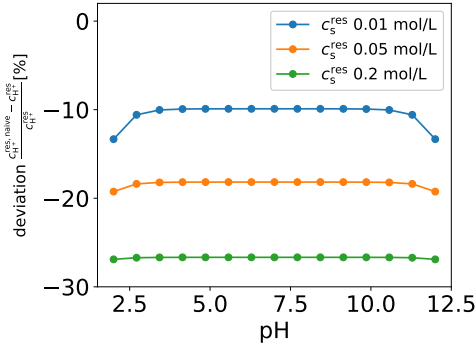


Figure 5.5: Percent-wise deviation between the naively estimated  $H^+$  concentration  $c_{H^+}^{res, naive} := 10^{-pH} c_{\ominus}$  and the  $H^+$  concentration actually present at a given pH, determined with equations (5.15), (5.16) and (5.17).

would result in a deviation of about 20% in the  $H^+$  concentration compared to the experiment. The difference between the naive and our approach increases even further with higher salt concentration (see Figure 5.5).

| pH      | $c_{\text{H}^+}^{\text{res}}$ experiment | $c_{\text{H}^+}^{\text{res}}$ simulation | $c_{\text{H}^+}^{\text{res}}$ naive |
|---------|--|--|-------------------------------------|
| 3.31    | 0.0005                                   | 0.00050                                  | 0.00049                             |
| 2.04    | 0.01                                     | 0.01013                                  | 0.00912                             |
| 1.10    | 0.1                                      | 0.10256                                  | 0.07943                             |
| (0.52   | 0.4                                      | 0.42810                                  | 0.30200)                            |
| (0.2676 | 0.69                                     | 0.77171                                  | 0.54000)                            |

Table 5.1: We compare the experimentally measured pH (column 1) with the actual molar concentration of HCl (column 2), the molar concentration of HCl used in our simulations based on the Section 5.3.1, using the provided pH and  $c_{\text{salt}}^{\text{res}} = 0 \text{ mol/L}$  (column 3) and the naive approach (column 4). The experimental data are taken from [137, table 1], making use of Equation (5.1). Data in brackets are only provided for completeness, but are outside the range of pH values we are interested in. Deviations in this range are due to different interactions in a real solution and the particle-based MD model.

### Note 12

In the Poisson-Boltzmann model, we assume that the excess chemical potentials in the reservoir are zero. In this case, the above equations are simplified considerably. pH is then given by  $\text{pH} = -\log_{10} c_{\text{H}^+}^{\text{res}}/c^\ominus$  and  $c_{\text{OH}^-}^{\text{res}}$  is directly given via Equation (5.17)

$$c_{\text{OH}^-}^{\text{res}} = \frac{K_w c^\ominus^2}{c_{\text{H}^+}^{\text{res}}}.$$

Together with the salt concentration  $c_{\text{salt}}^{\text{res}}$  we obtain the other two concentrations  $c_{\text{Cl}^-}$  and  $c_{\text{Na}^+}$  (via equations (5.14) and (5.13)). Therefore, the reservoir composition is fully described.

### 5.3.2 Particle Exchanges

In the last Section 5.3, we determined the chemical potentials of all species in the reservoir ( $\mu_{\text{H}^+}^{\text{res}}, \mu_{\text{OH}^-}^{\text{res}}, \mu_{\text{Na}^+}^{\text{res}}, \mu_{\text{Cl}^-}^{\text{res}}$ ) given a specific pH value and salt concentration.

We now to use these chemical potentials as an input to the grand-canonical simulation method (see Section 2.5.3). It is important to realize that the electroneutrality constraint of the system can only be obeyed if we exchange always a pair of one anion and one cation. Comparing the acceptance criteria of the grand-canonical simulation method (Equation (2.60)) to the acceptance criteria of the reaction ensemble (Equation (2.67)), we can write these particle exchanges as chemical reactions, in which particles are created (inserted) in the simulation box or deleted (removed) from the simulation box. Specifically, to simulate particle exchange with a reservoir consisting of  $\text{Na}^+$ ,  $\text{Cl}^-$ ,  $\text{H}^+$  and  $\text{OH}^-$  ions, we define the following reactions (ion pair inserctions):



where  $K_w$  is the ionic product of water, and we define the corresponding equilibrium constants  $K = \prod_i a_i^{v_i} = \exp(\beta \sum_i (\mu_i - \mu_i^\ominus) v_i)$ . For example, the equilibrium constant of the insertions (5.18) is given by:

$$K_{\text{Na+Cl}} = a_{\text{Na}^+} a_{\text{Cl}^-}. \quad (5.22)$$

The stoichiometric matrix for this set of exchange moves is given by [138]:

$$\begin{array}{lcl}
 & \text{Na}^+ & \text{Cl}^- & \text{H}^+ & \text{OH}^- \\
 \text{eq. (5.18)} & \left( \begin{array}{cccc} 1 & 1 & 0 & 0 \\ 0 & 1 & 1 & 0 \\ 1 & 0 & 0 & 1 \\ 0 & 0 & 1 & 1 \end{array} \right) & & & \\
 \text{eq. (5.19)} & & & & \\
 \text{eq. (5.20)} & & & & \\
 \text{eq. (5.21)} & & & & 
 \end{array} \quad (5.23)$$

This matrix has rank three and therefore it is rank deficient. The above exchange moves are, hence, not linearly independent. For example adding ( 5.18 + 5.21) yields the same result as ( 5.20 + 5.19) and the corresponding equilibrium constant is given by:

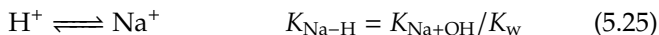
$$K_{\text{Na+Cl}}K_w = K_{\text{H+Cl}}K_{\text{Na+OH}} \quad (5.24)$$

Since  $K_w$  is fixed, only two of the three remaining constants can be chosen independently to uniquely determine the system composition. All sets of exchange moves which can be obtained via Gaussian elimination of the above stoichiometric matrix can be used to simulate the system in contact with the reservoir. A set of moves with a stoichiometric matrix of rank three is sufficient to observe arbitrary compositions (possibly limited in the way the particle numbers fluctuate). A different set of particle exchange move converges to the same final result, however, it may have very different sampling efficiency under different conditions [139].

An alternative to inserting and deleting ion pairs is the exchange



of particle identities which can be formulated as reactions (formally obtained by subtracting ( 5.20 – 5.21) and ( 5.19 – 5.21) ):



where  $K_{i-j} = a_i/a_j$ .

Adding the identity exchange moves in 5.25 and 5.26 to the set of particle exchange moves 5.18 — 5.21 makes the set of exchange moves even more redundant. However, they are computationally very cheap, and very efficiently speed up the simulation. We choose a redundant set of moves to simulate our systems using the same set of moves in a broad range of reservoir compositions.

## 5.4 Chemical Reactions in an Interacting System

Acid-base ionization equilibria involve a reaction with water. The acidity constant  $K$ , i.e. equilibrium constant of the ionization reaction in equation 2.16 is defined as

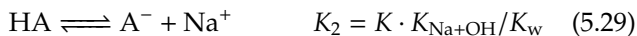
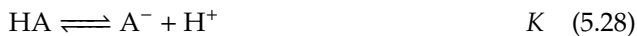
$$K = \frac{a_{\text{A}^-} a_{\text{H}^+}}{a_{\text{HA}}} \quad (5.27)$$

where  $a_i$  is the activity of the corresponding component  $i$ . By convention, the activity of water is assumed to be constant and is included in the definition of  $K$ . This is consistent with the

implicit solvent representation assumed in our simulation model. The  $\text{H}^+$  and  $\text{OH}^-$  ions are explicitly treated which is important for the electrostatic interactions in the system.

We simulate chemical reactions (see section 2.16) using the reaction ensemble [19]. A problem for the efficiency of the algorithm arises at  $\text{pH} \gtrsim 4$ , where the concentration of  $\text{H}^+$  is so low that with the usual simulation box size  $L \approx 20\text{nm}$  one would obtain less than one  $\text{H}^+$  ion per simulation box. In such case, the reaction ensemble simulation suffers from serious finite-size effects. At  $\text{pH} \gtrsim 11$  this problem can be circumvented by re-formulating the ionization reaction using the  $\text{OH}^-$  ion instead of  $\text{H}^+$ , as has been done by Rathee et al. [140, 141]. A different approach is needed in the intermediate pH range [4, 10] where both  $\text{H}^+$  and  $\text{OH}^-$  ions are scarce.

To avoid this bottleneck in the sampling, we re-formulate the ionization reaction using other ions, and modify the equilibrium constants accordingly. This approach greatly increases the sampling efficiency [139]. By using the reaction in 2.16 and performing subsequent ion-exchange reactions in Equations 5.20, 5.19, 5.21, we obtain the following set of alternative reactions with modified reaction constants:



Each of the above reactions has a different equilibrium constant

that follows from the activities involved in the reaction (see Note 13).

### Note 13

In this note we derive the corresponding equilibrium constants for the alternative forms of reaction (5.28) which has, by definition, the equilibrium constant

$$K = \frac{a_{H^+} a_{A^-}}{a_{HA}}.$$

The reaction constant  $K_2$ , for reaction (5.29), is given by:

$$K_2 = \frac{a_{A^-} a_{Na^+}}{a_{HA}} = \frac{a_{A^-} a_{Na^+}}{a_{HA}} \frac{a_{H^+} a_{OH^-}}{a_{H^+} a_{OH^-}} = \frac{K K_{Na+OH}}{K_w}. \quad (5.32)$$

The reaction constant  $K_3$ , for reaction (5.30), is given by:

$$K_3 = \frac{a_{A^-}}{a_{HA} a_{Cl^-}} = \frac{a_{A^-}}{a_{HA} a_{Cl^-}} \frac{a_{H^+}}{a_{H^+}} = \frac{K}{K_{H+Cl}}. \quad (5.33)$$

The reaction constant  $K_4$ , for reaction (5.31), is given by:

$$K_4 = \frac{a_{A^-}}{a_{HA} a_{OH^-}} = \frac{a_{A^-}}{a_{HA} a_{OH^-}} \frac{a_{H^+}}{a_{H^+}} = \frac{K}{K_w}. \quad (5.34)$$

Additionally, we attempt particle swapping moves



which have a symmetric proposal probability and are accepted with the normal Metropolis criterion of Equation (2.58). These moves help to equilibrate the charge profile along the polymer

backbone if the number of other ions present is too small to mediate this swapping reaction.

**Note 14**

There are two distinct reasons why we cannot perform the simulations using the constant pH method (see Section 2.5.3, [48]):

- First, we showed in [4] that the constant pH method treats ions implicitly, and hence, gets the electrostatic screening effects wrong. “Implicit” means, in this context, that the dissociation equilibrium is adjusted as if a certain pH was present in the surrounding of the system, but the  $H^+$  ions which would need to be present in the system are *not existing* in the system. It is important to note that pH is a measure for the chemical potential of  $H^+$  and is therefore directly related to actual  $H^+$  concentrations (compare Equation (5.15)). Implicit ions, therefore, cannot contribute to electrostatic screening or even ideal gas pressures. Hence, this approach is error prone when describing weak polyelectrolyte gels, which requires finding pressure equilibria.
- Second, it is important to note that the ionization equilibrium in a Donnan-partitioned system is not solely determined by the pH of the reservoir, but is sensitive to a Donnan potential induced shift  $\Delta$  (see note 10). This is true for non-interacting and interacting systems. Since the Donnan potential (and

therefore the correct value for the input pH) is unknown, and it is also coupled to the charge state of the weak polyelectrolyte (which we do not know prior to simulation), employing the constant pH method to simulate Donnan-partitioned systems suffers from a systematic error.

## 5.5 Simulation Protocol and Setup

**Parameters of the simulated systems** We simulate 16 polyelectrolyte chains, composed of  $N = 50$  monomers per chain, in an implicit solvent and a cubic simulation box. The simulations are performed at different box lengths  $L \in \{23.09, 40.86, 58.62, 76.39, 80.00\}\sigma$  that correspond to a concentration of monomer units of  $c_0 \in \{2.41, 0.435, 0.147, 0.067, 0.058\}\text{mol/L}$ , which is within the range commonly used in the experiments. The pH of the reservoir is adjusted to the desired value by adding HCl or NaOH as outlined in Section 5.3. We simulate the polyelectrolytes with various acidity constants,  $\text{p}K \in \{1, 2, 3, 4\}$ , in equilibrium with reservoirs at various pH values,  $1 \leq \text{pH} \leq 13$ , and various NaCl concentrations,  $0.01\text{mol/L} \leq c_{\text{salt}}^{\text{res}} \leq 0.2\text{mol/L}$ .

We use the reaction ensemble method to account for the ionization reaction. Because we span a broad range of pH values, the  $\text{H}^+$  ions are often scarce in our simulations. Therefore, we implement the acid ionization reaction 2.16 using the reactions (5.28), (5.29), (5.30) (5.31) and the particle swapping move (5.35). The  $\text{Na}^+$  and  $\text{Cl}^-$  ions are always present in sufficient number, so that the acid protonation reaction is not affected by finite size effects.

The chemical potentials of  $\text{Na}^+$ ,  $\text{Cl}^-$ ,  $\text{H}^+$ ,  $\text{OH}^-$  are determined as outlined in Section 5.3, and are used to couple the system to the reservoir by insertion of  $\text{Na}^+\text{Cl}^-$  ion pairs, (5.18) and by identity exchange moves, (5.25) and (5.26).

Ions are modeled using the restricted primitive model, characterized by the valency and effective ion size. For simplicity, the short-range interactions (excluded volume) of all particles (small ions and monomers of the polymer) are represented by a purely repulsive WCA potential [35], with the effective particle size  $\sigma = 0.355\text{nm}$  and strength of the interaction  $\epsilon = 1.0 k_{\text{B}}T$ . The FENE potential is used to account for polymer connectivity, with the typical Kremer-Grest parameters [36]  $k_{\text{FENE}} = 30.0 k_{\text{B}}T/\sigma^2$ , and  $R_{\text{max}} = 1.5\sigma$ . Functional forms of the interaction potentials are given in Section 2.5. The electrostatic coupling strength is defined by the Bjerrum length  $\lambda_{\text{B}} = 2.0\sigma = 0.71\text{nm}$  that approximately corresponds to aqueous solution at  $T = 298\text{K}$ . We use the value of  $\text{p}K_{\text{w}} = 14$  that corresponds to the same temperature. Note, that the Bjerrum length, all equilibrium constants, and all interaction parameters defined above are temperature-dependent. Therefore, if the simulation has to be performed at a different temperature, all these parameters need to be adjusted in order to remain internally consistent.

**Simulation protocol** The Langevin equation is integrated by a velocity Verlet algorithm with a time step of  $\delta t = 0.01\sigma(m/k_{\text{B}}T)^{1/2}$  where  $m$  is the mass of the particles.<sup>4</sup> The equilibration consists

---

<sup>4</sup> Note that mass of the particles is irrelevant and all presented results are invariant with respect to it. However, the ratio of the particle mass and energy determines the stability window of the algorithm. Also, the time evolution of the system is non-physical, as the Monte Carlo reaction moves do not include the physical dynamics.

of 50 cycles, where each equilibration cycle consists of  $16N + 10$  reaction moves and  $1000 + 2N$  MD integration steps followed by an additional equilibration of the reactions and particle exchanges with 160000 reaction and particle exchange moves. The following production run typically contained 13000 production cycles (median value), each consisting of  $3N + 20$  reaction moves, and  $1000 + 2N$  MD integration steps, with  $N$  the number of monomers per chain. We calculate ensemble-averaged values of the observables from the configurations after each production cycle. To assess the statistical accuracy of our data, we use the correlation-corrected error estimate [142]. The total length of the typically gave  $\approx 500$  uncorrelated samples of the slowest decorrelating observable (i.e. the end-to-end distance).

### 5.5.1 Validation of the Reservoir Chemical Potentials

As a first step to validate our algorithm, we verify that the reservoir chemical potentials determined using the procedure described in Section 5.3 lead to the desired concentrations. We start with a simulation box containing some ions so that the P3M algorithm can tune<sup>5</sup>, and simulate exchange of ions with the reservoir using the exchange moves (5.18), (5.25) and (5.26). We perform the simulations for all combinations of the parameters:  $\text{pH} \in \{1, 2, \dots, 13\}$ ,  $c_{\text{salt}}^{\text{res}} \in \{0.01, 0.2\} \text{ mol/L}$ , and various simulation box lengths between  $\text{box}_l \in [18.4, \dots, 72]\sigma$ . In Figure 5.6, we show

<sup>5</sup>Tuning of the P3M algorithm is crucial for optimal computational efficiency but does not affect the reported results. For optimal efficiency the number of ions during tuning should be close to the expected average number of ions.

that the concentration of ions in the box,  $c_i^{\text{box}}$  coincides with the expected reservoir concentration within 1%.

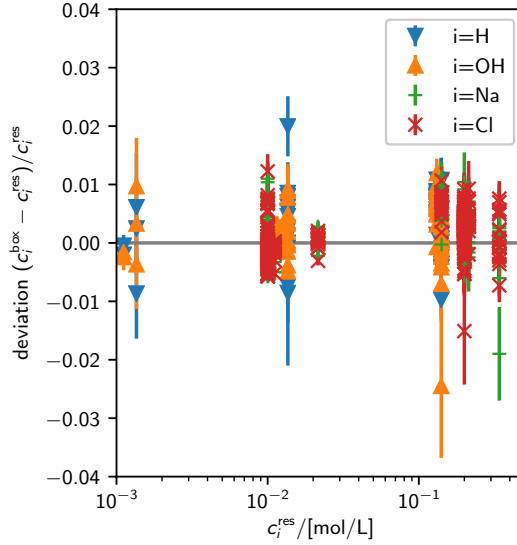


Figure 5.6: Relative deviation of the ion concentrations inside the simulation box and in the reservoir: There are close to no deviations between the concentrations which are set and the ones which are observed.

Results yielding less than 10 particles in the simulation box are omitted because they are affected by finite-size effects. Deviations of all the results shown in Figure 5.6 are within the estimated statistical accuracy, supporting the validity of our algorithm.



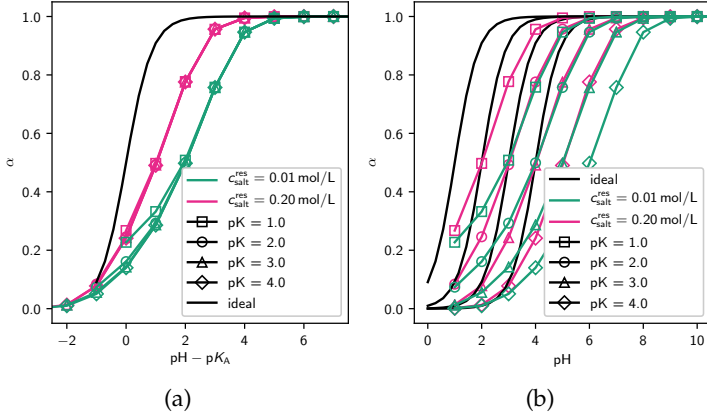


Figure 5.7: Ionization degree of the polyelectrolyte as a function of pH at various salt concentrations in the reservoir, and various acidity constants of the polymer, as indicated in the legend. The box length is  $80\sigma$  corresponding to a monomer concentration  $c_0 \approx 0.057 \text{ mol/L}$ . Error bars are smaller than the point size.

## 5.6 Polyelectrolyte Solution

### 5.6.1 Effect of pH and Salt

After demonstrating that our simulation correctly implements the grand-canonical scheme, we focus our attention on the combined effect of pH and salt concentration on the weak polyelectrolyte ionization process.

In Figure 5.7 a) we show that the polyelectrolyte ionization is suppressed by mutual repulsion between the ionized groups, resulting in the well-known shift of the polyelectrolyte titration curve with respect to the ideal one. Figure 5.7 a) also shows that addition of salt screens the electrostatic interactions and results

in a shift of the titration master curve closer to the ideal one. For comparison, we also show the degree of ionization as a function of pH in Figure 5.7 b).

In a large pH range the titration curves for polymers with different  $pK$  values in Figure 5.7 collapse onto one master curve at one reservoir salt concentration (with minor deviations). In general, the ionization degree is, however, not a universal function of  $pH - pK$  at a given ionic strength. At intermediate pH, the ionic strength is approximately equal to the reservoir salt concentration. Therefore, we obtain the master curves at a fixed reservoir salt concentration. If the ionic strength induced by pH (i.e. at low or high pH) is bigger than the ionic strength caused by the salt, then the added acid or base result in a significantly increased electrostatic screening and a deviation from the master curves [4].

The chain swelling is affected by the pH on both ends of the pH scale, as can be seen from the dependence of chain end-to-end distance  $R_e$  on pH, shown in Figure 5.8. On one end of the pH range, the swelling is controlled by varying polymer ionization, as is demonstrated by all curves at the same salt concentration collapsing on one master curve as a function of  $pH - pK$  at low pH values (Figure 5.8a). Interestingly, the deviations from the master curves at low pH in Figure 5.7 do not show up in Figure 5.8. Presumably, this is because the screening due to  $H^+$  ions at low pH has two counter-acting effects: On one hand, it increases the ionization, which increases the swelling. On the other hand, it reduces electrostatic repulsion among the ionized groups, which reduces the swelling. Apparently, these two effects compensate each other, and we do not observe deviations from the master

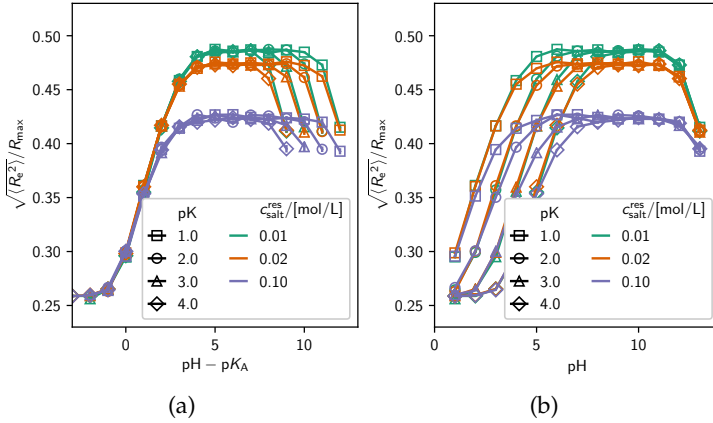


Figure 5.8: End-to-end distance of the polyelectrolyte chain as a function of  $\text{pH} - \text{pK}_a$  (left) and the same data plotted as a function of  $\text{pH}$  (right). Reservoir salt concentrations and  $\text{pK}_a$  values are indicated in the legend. The box length is  $80\sigma$  corresponding to a monomer concentration  $c_0 \approx 0.057$  mol/L. Error bars are smaller than the point size.

curve, as in Figure 5.7. On the other end of the pH range, the swelling is controlled by the electrostatic screening due to  $\text{OH}^-$  ions. This causes all curves to collapse on one master curve as a function of  $\text{pH}$  at high  $\text{pH}$  values in Figure 5.8b. The collapse is independent of  $\text{pK}$ , as long as  $\text{pH} - \text{pK} \gg 1$ , because then the polymer is fully ionized.

This non-monotonic swelling as a function of  $\text{pH}$  and salt concentration has been presumably never observed in coarse-grained simulations. However, it has been previously detected in experiments and via numerical mean-field models. Borisov et al. [143] predicted a non-monotonic swelling of star-like weak polyelectrolytes as a function of salt concentration, and explained this effect by similar arguments: starting from low ionic strength, the

stars first swell because their ionization degree increases as the ionic strength is increased, and at higher ionic strength the fully ionized stars shrink because of ionic screening. A similar effect on the swelling of weak polyelectrolyte micelles are observed experimentally by Matějček et al. [144]. Later, they confirmed it in simulations, combining explicit-particle representation of the polymers with mean-field treatment of small ions on the Poisson-Boltzmann level [145]. The molecular theory of Longo et al. [146] also combined molecular representation of polyelectrolytes with mean-field treatment of small ions to observe a similar effect on the swelling of polyelectrolyte gels grafted to a surface. In all cases mentioned above, the mean-field representation of small ions allowed to set the reservoir concentrations as boundary conditions. Using the same approach in coarse-grained simulations with explicit ions would require unfeasibly big simulation boxes in order to avoid finite-size effects.

We emphasize that the combined effect of salt (ionic strength) and pH on the chain swelling can be observed on both ends of the pH scale only if the concentrations of all ions are correctly accounted for. In Figure 5.9, we show that the grand-reaction method predicts the polyelectrolyte collapse at high pH values, whereas the usual implementation of the constant pH method fails to predict this effect. Instead, it predicts that the polyelectrolyte remains swollen at arbitrarily high pH. At  $\text{pH} \gg \text{pK}$  the polyelectrolyte is fully ionized and the collapse is caused by increasing ionic strength with pH (compare Figure 5.2). The constant pH simulation cannot predict this effect because it completely lacks the  $\text{OH}^-$  ions, and their respective counter-ions. This failure is important at low salt concentrations, and at high or low pH values ( $\text{pH} \lesssim 3$  or  $\text{pH} \gtrsim 11$ ), where the  $\text{H}^+$  and  $\text{OH}^-$

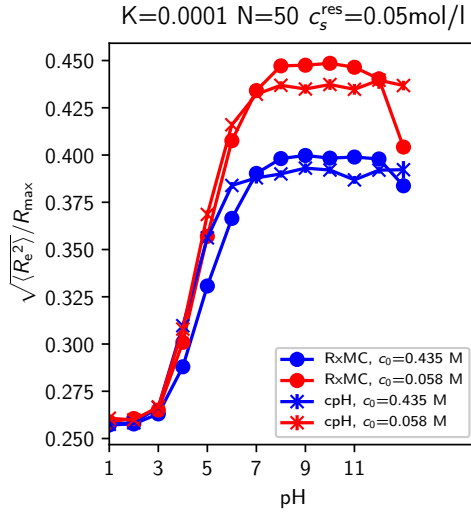


Figure 5.9: End-to-end distance of a polyelectrolyte with  $pK = 4.0$  as a function of pH, simulated using the grand-reaction method (circles) and using the constant pH method (crosses). Different monomer concentrations in the reservoir are indicated in the legend. Error bars are on the order of the point size.

ions dominate the electrostatic screening.

## 5.7 Summary

The grand-reaction method, presented here, provides a robust tool for coarse-grained simulations of ionization equilibria in a broad range of pH values. The pH and salt concentration are defined by the composition of the reservoir, with which the system can exchange small ions. Our implementation of particle exchange with the reservoir avoids known artifacts and nonphysical parameter combinations that have been used in some previous studies which employed the constant pH method. With the grand-reaction method, the accessible pH range is no longer limited by the simulation algorithm.

We demonstrated that our implementation is correct by simulating a solution of weak polyelectrolytes as a model system. In the absence of interactions and the polyelectrolytes, our simulations reproduced the multi-component reservoir. Next, we showed that the grand-reaction method allows to study the combined effect of pH and reservoir ionic strength on the ionization and swelling of weak polyelectrolytes. In particular, it can reproduce the non-monotonic swelling as a function of pH, that has been known and understood from experiments and from mean-field calculations but it has not been observed in simulations before.

The method can be used for simulating any macromolecular or colloidal system in equilibrium with a reservoir at a given pH and salt concentration. The same principles and guidelines can be applied to simulate for example weak polyelectrolyte gels (as outlined in Chapter 6), polymers attached to a surface, interpolyelectrolyte complexes in equilibrium with a reservoir solution, peptides or proteins in salt solutions. In such systems,

the effect of pH and salt on ionization is routinely exploited in experiments but it is often interpreted assuming ideal ionization response. Our method opens up the possibility to predict the properties of such systems, and ensures that the results are physically consistent.

Extensions of the grand-reaction method to a reservoir with more components, or to multiple chemical reactions in the system are straightforward. As another extension to our method one can envision more sophisticated treatment of ions, such that they do not have identical parameters. One could account for the different effective radii of the hydrated ions [147] which affects their excess chemical potential. The influence of multivalent ions could also be simulated using our method. Determination of the reservoir chemical potentials would need to be modified in both cases mentioned above because different interaction parameter imply different excess chemical potential of each ion.





---

## 6 Weak Polyelectrolyte Gels

Most simulations of polyelectrolyte gels have considered strong polyelectrolytes [53], while experiments and applications often consist of weak polyelectrolytes like, for example, polyacrylic acid (shown in Figure 6.1). Polyacrylic acid has titrable groups

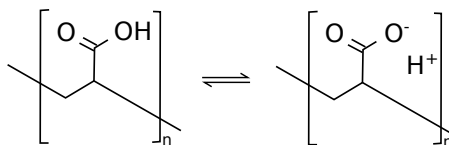


Figure 6.1: Polyacrylic acid is an example for a weak polyelectrolyte.

which are, depending on pH, either protonated or deprotonated. The influence of pH gives rise to protonation-configuration coupling [148, 149]. In this chapter, we present (for the first time) particle-based simulations of weak polyelectrolyte gels without mean-field assumptions. We recently discussed the state of art for simulating weak polyelectrolytes in reference [53] and found that so far there are only three simulation methods capable of describing weak polyelectrolyte gels which, however, employ mean-field assumptions: Longo et al. [68] presented their “molecular theory” which combines mean-field approximations with sampling of gel conformations via explicit particle representations. Another mean-field approach is presented by

Rud et al. [90] who applies periodic boundary conditions to a self-consistent mean-field model of a star such that it represents a macroscopic gel.

In this chapter we use the grand-reaction method, introduced in chapter 5, for simulating macroscopic weak polyelectrolyte gels. The grand-reaction method allows to impose the pH of a supernatant solution and to treat all further dissociation processes in the gel correctly. Additionally, we adapt the cell-gel models (CGMs) from chapter 3 to also model weak polyelectrolyte gels.

We are able to reproduce two important experimental results with our adapted periodic gel model and the two CGMs:

- the deswelling of polyelectrolyte gels at high pH [135, 112]
- the non-monotonic swelling of weak polyelectrolyte gels with increasing salt concentration at fixed pH [112]

These two phenomena can already be understood in the idealized Donnan model, and we already gave details on this simplistic model in the Section 5.2.

### 6.1 Simulation Protocol and Setup

We simulate a tetra-functional weak polyelectrolyte gel with monodisperse chain length  $N = 40$  and acidity constant  $pK = 4$ . The monomers take part in the following reaction:



We vary the pH of the supernatant solution in the range  $\text{pH} \in \{1, 2, 3, \dots, 13\}$  with reservoir salt concentrations in the range  $c_{\text{salt}}^{\text{res}} \in \{10^{-7}, 10^{-6}, \dots, 0.2\} \text{mol/L}$ .

### 6.1.1 Particle-Based Simulations

We use the grand-reaction method as presented in chapter 5. Especially, we employ the particle exchange moves (5.18), (5.19), (5.20), (5.21) and the identity exchange moves, (5.25) and (5.26) in order to be able to simulate low salt concentrations and minimize finite size-effects. For ensuring chemical equilibrium we use reactions (5.28), (5.29), (5.30), (5.31) and the particle swapping move (5.35). The simulation protocol is similar to the one presented in Section 5.5. We perform extensive equilibration of the particle exchanges and reactions in the system prior to producing data. We simulate at different prescribed volumes and calculate the pressure in the gel to obtain  $PV$  curves. The difference to the previous simulations of strong gels is that we now consider weak acidic monomers.

**Periodic Gel Simulations** The periodic gel simulations are set up and used as described in Section 2.6.2.

**Single-Chain Cell-Gel Model** The single-chain cell-gel model (CGM) is set up and used as described in chapter 3.

### 6.1.2 Poisson-Boltzmann Cell-Gel Model

The Poisson Boltzmann cell-gel model (CGM) is set up and used as described in chapter 3. In contrast to the previous simulations,

we now consider weak acidic monomers and couple the cell to a more complicated reservoir containing  $H^+$ ,  $OH^-$ ,  $Na^+$ ,  $Cl^-$  ions. As outlined in Section 2.4, coupling a reservoir to a system which is modeled via Poisson-Boltzmann theory is straightforward, given the reservoir concentrations. In PB theory, we set the reservoir electric potential to zero which means that we assume zero excess chemical potentials in the reservoir. Therefore, we can use the results acquired in note 12. Neglecting  $OH^-$  ions can only be done safely at low pH but not at high pH, where  $OH^-$  ions are ubiquitous. Neglecting  $OH^-$  ions at high pH results in false predictions of the swelling equilibria.

We treat pH-dependent reactions using the charge regulation approach by Ninham et al. [5, 23]. The charge regulation determines the degree of dissociation and, therefore, the space charge density of the penetrable rod. For a weak polyelectrolyte, monomers may be either neutral or charged ( $HA \rightleftharpoons A^- + H^+$ ). The dissociation constant in the Poisson-Boltzmann framework is given by:

$$K = \frac{a_{H^+} a_{A^-}}{a_{HA}} = \frac{c_{H^+}(\vec{r}) c_{A^-}(\vec{r})}{c_{HA}(\vec{r}) c^\ominus}, \quad (6.2)$$

where we used Equation (2.34) to introduce the position dependence.

The concentration of titratable monomers,  $A^-$  or  $HA$ , is  $c_0(\vec{r}) = c_{A^-}(\vec{r}) + c_{HA}(\vec{r})$  and is distributed with probability density  $p(\vec{r})$ , i.e.  $c_0(\vec{r}) = Np(\vec{r})$ . This gives  $c_{HA}(\vec{r}) = Np(\vec{r}) - c_{A^-}(\vec{r})$  which we substitute into Equation (6.2) and solve for  $c_{A^-}(\vec{r})$ :

$$c_{A^-}(\vec{r}) = \frac{c_0(\vec{r}) K c^\ominus}{c_{H^+}^{\text{res}} \exp(-e_0 \psi(\vec{r}) / (k_B T)) + K c^\ominus}. \quad (6.3)$$

The fixed charge density used in the PB Equation (3.14) is then given by  $\rho_f(\vec{r}) = -e_0 c_{A^-}(\vec{r})$ .

Equation (6.3) is equivalent to a space dependent degree of dissociation  $\alpha(\vec{r})$ , given by:

$$\alpha(\vec{r}) = \frac{c_{A^-}(\vec{r})}{c_0(\vec{r})} = \frac{Kc^\ominus}{c_{H^+}^{\text{res}} \exp(-e_0\psi(\vec{r})/(k_B T)) + Kc^\ominus}. \quad (6.4)$$

Using the charge regulation approach above, we can perform PB CGM simulations of weak polyelectrolyte gels.

## 6.2 pH-dependent Swelling of Gels

To compute the equilibrium swelling, we compute, as outlined before in Section 2.6.2, pressure-volume curves. The pressure as a function of the end-to-end distance, for two different pH values and a fixed salt concentration, is shown in Figure 6.2 for the i) periodic gel MD model, ii) the single-chain CGM and iii) the PB CGM. The results  $P(R_e)$  of all three models agree very well. When the gel is compressed, the pressure is greater than the pressure of the reservoir ( $P^{\text{gel}} - P^{\text{res}} > 0$ ) and when the gel is stretched the pressure of the gel is smaller than the pressure of the reservoir ( $P^{\text{gel}} - P^{\text{res}} < 0$ ). Changing the pH value of the supernatant solution increases the pressure in the gel. This can be seen in Figure 6.2: The  $P(R_e)$  curves are shifted upwards for higher pH. The reason for this increased gel pressure is an increased dissociation of the gel charges: at high pH the weak acid is more dissociated. This results in a) an increased osmotic pressure of the ions and b) an increased repulsion of monomers

along the polymer backbone. As for the strong gels before, the zero crossing of the pressure curve is the equilibrium end-to-end distance  $R_{eq}$ . As we can see in Figure 6.2, the three models agree in tendency. For  $pH = 11$  there are differences between the single-chain CGM and the periodic gel model visible left to the zero crossing of the  $P - R_e$  curve. In this pH range the weak polyelectrolyte gel is highly charged and compressing the gel results in strong electrostatic inter-chain repulsions increasing the pressure of the system. Since this chain-chain repulsion is not present in the single chain model, the corresponding  $P - R_e$  curve of the single-chain model is below the one for the periodic gel model. We expect that the chain-chain repulsion decreases, the more the gel is stretched and indeed Figure 6.2 shows that both particle-based models have roughly the same zero crossing. For  $pH = 3$  the gel is almost uncharged and the  $P - R_e$  curve of the single-chain CGM and the periodic gel model agree within errorbars. Around  $pH = 3$  the  $P - R_e$  curve of the PB CGM model however differs from the ones of the two particle-based models. In this pH range the gel is almost uncharged (see Figure 6.3b)). In this case the stretching pressure is the dominating pressure contribution and a deviation from the particle-based models reflects that the expression used for the stretching pressure is based on very simplistic arguments (see Section 3.5.1).

In Figure 6.3 a) we show the equilibrium extension of the chains  $R_{eq}$  of a weak polyelectrolyte gel as a function of pH. All models predict that the gel is collapsed at low pH. With increasing pH the dissociation of the monomers increases (see Figure 6.3 b). This increased charge of the gel results in a stretching of the gel which can be seen in Figure 6.3 a). Around  $pH = 9$  the maximum degree of dissociation  $\alpha$  is reached and the gel

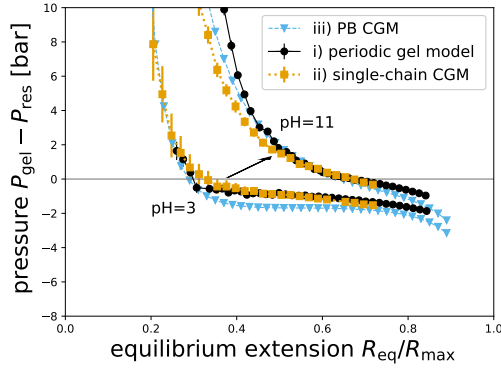


Figure 6.2: Pressure curves of the different gel models ( $pK = 4$ ,  $c_{\text{salt}}^{\text{res}} = 0.01\text{mol/L}$ ) at  $\text{pH} = 3$  and  $\text{pH} = 11$  as a function of  $R_e/R_{\text{max}}$ , where  $R_{\text{max}} = (N - 1)b$  is the contour length of the chain. From these curves the equilibrium end-to-end distances in swelling equilibrium  $R_{\text{eq}}$  are found via linear interpolation. Errors in  $R_e/R_{\text{max}}$  are typically smaller than symbol size.

swelling plateaus. A further increase of pH in the reservoir adds more  $\text{Na}^+$  and  $\text{OH}^-$  ions. On the one hand, this increases the electrostatic screening in the gel and reduces the repulsion of like charged monomers. On the other hand, further addition of  $\text{Na}^+$  and  $\text{OH}^-$  ions increases the (osmotic) pressure excreted by the reservoir. Both effects deswell the gel again around  $\text{pH} = 11$ . These findings in Figure 6.3 a) are in good qualitative agreement with experiments [135, 150] and in analogy to the findings for the end-to-end distance of polyelectrolytes in solution (see Section 5.6).

In Figures 6.3, we observe that the swelling and dissociation behavior of the two particle-based models are very similar. However, for small pH value the PB CGM shows slightly lower

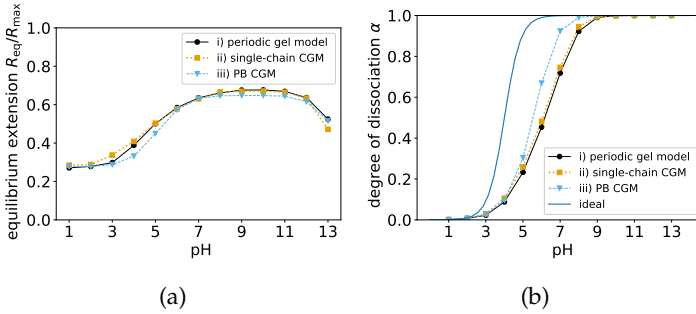


Figure 6.3: a) Swelling of the gel as a function of pH ( $pK=4$ ,  $c_{salt}^{res} = 0.01\text{mol/L}$ ). b) degree of dissociation with pH

equilibrium extensions  $R_{eq}$ . From figures 6.3 b), we see that the gel is only slightly charged in this pH range. Again, the stretching pressure is the dominant contribution here, and we attribute the deviation of the PB CGM to the other models to the simplistic arguments used in deriving the stretching pressure (see Section 3.5.1).

The dissociation behavior in Figure 6.3 b) shows an even more pronounced difference of the PB CGM to the two particle-based models: the degree of dissociation in the PB CGM is constantly increased compared to the two particle-based models. We attribute this to the fact that the dissociation equilibria are determined differently in the PB CGM compared to the particle-based models. In the PB framework only the local concentrations enter the calculation which determines  $\alpha$  (compare Equation (6.4)). In the particle-based models also an energetic contribution enters in the reaction-ensemble acceptance probability (compare (2.67)). This energetic contribution penalizes states with high electrostatic repulsion, resulting in a decreased degree of dissociation



compared to the PB CGM.

## 6.3 Salt-Dependent Swelling of Gels

In Figure 6.4 a) we show the equilibrium end-to-end distance of the chains in the gel as a function of salt concentration.

We observe that the gel swells more with increasing salt concentration. This increase in swelling is caused by an increase in the degree of dissociation (see Figure 6.4 b). This increase of the degree of dissociation  $\alpha$  with increasing salt concentration is also observed for non-interacting particles in Figure 5.3a. The mechanism behind this is the exchange of  $H^+$  ions which are confined in the gel (due to the electroneutrality constraint) with  $Na^+$  ions from the reservoir (see discussion in Section 5.2). At high salt concentrations the gel deswells again due to a) increased electrostatic screening and b) a higher (osmotic) pressure exerted by the salt reservoir.

This non-monotonic swelling with salt concentration is reported by experiments [112, 135] and now for the first time also in particle-based simulations.

In Figure 6.4 a), we again observe that the particle-based models agree very well in tendency. Only at very reservoir salt concentrations below  $10^{-6}$  mol/L, we observe a discrepancy. Since the gel is almost uncharged in that regime (compare Figure 6.4 a)), the only pressure contribution which seems capable of causing such a difference is the stretching pressure, which could be slightly

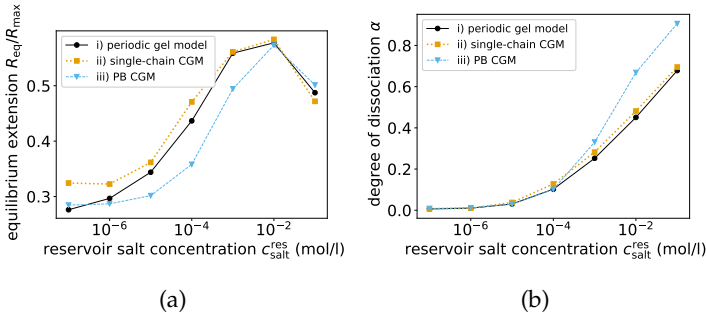


Figure 6.4: Swelling of the gel as a function of pH ( $pK = 4$ ,  $pH = 6$ ). As reported by Ricka [112], there is a non-monotonic swelling as a function of salt concentration. Figure b) Degree of dissociation increases with salt concentration. Figure b) resembles Figure 5.3a for the ideal Donnan-model. When solving the Donnan model, we assumed a fixed polymer concentration  $c_0$ , in contrast the polymer concentration  $c_0 = N_m/V_{eq}$  in the gel decreases when the gel swells.

different for a single chain and a network of chains due to correlations. Compared to the above deviations, the difference in the swelling behavior of the PB CGM and the two particle-based models is more pronounced. Below reservoir salt concentrations  $c_{salt}^{res} = 10^{-2}$  mol/L, the PB CGM is constantly swollen less than the two particle-based models. A possible explanation could involve, that the electrostatic repulsion between like charges is higher in the particle-based models than in the PB CGM. This could be caused by using a fixed charge distribution  $\rho_f(\vec{r})$  in the PB CGM which is too “dilute”, i.e. the used charge distribution does not reflect how tightly packed the charged monomers are in the particle-based models. This would not make a big difference for high salt concentrations because then the electrostatic repulsion between like charges is electrostatically screened. In the future,

one could try to improve the PB CGM with monomer charge distributions  $\rho_f(\vec{r})$  extracted from the *corresponding* single-chain simulations. While this could help to increase the agreement between the models, it would add further complication to the density based model.

While the two particle-based models agree again with respect to their dissociation behavior (see Figure 6.4 b)), it is once more observed (as in Figure 6.3 b)) that the PB CGM results in a higher degree of dissociation than the two particle-based models. This is again due to the fact that the particle-based models penalize states with high electrostatic repulsion of like charges more than the PB model.

## 6.4 Degree of Dissociation on Compression

In systems containing weak acids or weak bases there is the effect of protonation-conformation coupling [149]. In weak polyelectrolyte gels, the protonation-conformation coupling couples the degree of dissociation to the stretching state of the polyelectrolyte gel. In Figure 6.5 a) we observe that the degree of dissociation  $\alpha$  decreases with increasing polymer concentration  $c_0$ , i.e. with compression. This behavior is also obtained when solving the ideal Donnan model (see Section 5.2) which is shown in Figure 6.5 b). The differences between the Donnan model and the periodic gel MD results are due to the presence of interactions in the MD simulations. These interactions reduce the degree of dissociation compared to an ideal system. A decrease of the

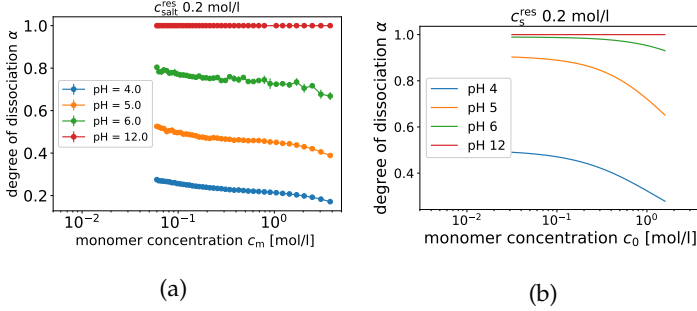


Figure 6.5: a) Periodic gel MD result and b) Donnan model result: The degree of dissociation  $\alpha$  decreases with higher monomer concentration, i.e. on compression.

degree of dissociation  $\alpha$  when compressing weak polyelectrolyte gels has been reported previously by Rud et al. [90].

In the spirit of Longo et al. [68], the reduction of the degree of dissociation with compression can be interpreted in the context of the Poisson-Boltzmann framework: the local degree of dissociation in equation 6.4 depends on the local electrostatic potential. In the Donnan model the degree of dissociation is determined by the same formula which has, however, no spatial dependence and makes use of the Donnan potential  $\Psi_D$  instead:

$$\alpha = \frac{c_{A^-}}{c_0} = \frac{Kc^\ominus}{c_{H^+}^{\text{res}} \exp(-e_0\psi_D/(k_B T)) + Kc^\ominus}. \quad (6.5)$$

Let us recall the electrostatic potential  $\psi_i$  of a point charge with charge  $q_i$  in the three-dimensional space:

$$\psi_i(\vec{r}) = \frac{q_i}{4\pi\epsilon_0\epsilon_r|\vec{r}_i - \vec{r}|} \implies \psi(\vec{r}) = \sum_i \psi_i(\vec{r}), \quad (6.6)$$

which can be superpositioned to give the electrostatic potential of a system of point charges  $\psi(\vec{r})$ . The electrostatic potential  $\psi_i(\vec{r})$  has the sign of the charge  $q_i$ :

$$\text{sign}(\psi_i(\vec{r})) = \text{sign}(q_i) \quad (6.7)$$

Therefore, the total electrostatic potential  $\psi(\vec{r})$  is more negative the more negative charges are located in the vicinity of  $\vec{r}$ . The density of negative charges increases when compressing a gel which undergoes reaction (6.1), or is increased close to the crosslinking points of the gel (see next section). According to Equation (6.5), we expect that the degree of dissociation is closer to zero the more negative the electric potential is (which happens on compression). In Figure 6.5, we observe that the degree of dissociation is reduced on compression, i.e. with higher polymer density  $c_0$ .

## 6.5 Charge Profile Along the Polymer Backbone

The charge profile along the polymer backbone, shown in Figure 6.6, is a microscopic observable which can be obtained from the detailed periodic gel MD simulations. The single-chain CGM and the PB CGM, on the other hand, only provide the degree of dissociation averaged over all monomers. The degree of dissociation  $\alpha_i$  as a function of the monomer index  $i$  in the chain is obtained via averaging over all identical monomers found in the 16 chains in the periodic gel model.

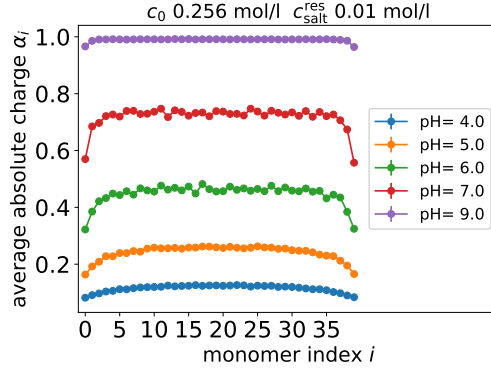


Figure 6.6: Dissociation profile  $\alpha_i$  along the polymer backbone for each monomer  $i$  at different pH values. The monomer next to a node has index 0. The monomer index then increases till  $N - 1$ , where the chain meets the next cross-linking point. In total the chain have  $N=40$  monomers.

As seen in Figure 6.6, monomers close to the nodes ( $i \approx 0$  and  $i \approx N - 1$ ) have a smaller degree of dissociation  $\alpha_i$  and, therefore carry on average a lower absolute charge  $\alpha_i \cdot e_0$ . This behavior was previously reported for microgels [151] and is related to the reduced dissociation of central monomers in linear weak polyelectrolytes [148] or stars [152]. As before, this result can be understood in the Poisson-Boltzmann framework using Equation (6.4): Around the cross-linking points in the gel, the concentration of negatively charged monomers is higher and therefore, the electric potential  $\psi$  is more negative. According to Equation (6.4) this results in a reduced local degree of dissociation  $\alpha(\vec{r})$ .

Figure 6.6 also shows the pH-dependence of the dissociation profile: with increasing pH the overall degree of dissociation  $\alpha = \frac{1}{N} \sum_i \alpha_i$  increases (which is similar to the case in Figure 6.3

b)). At low pH (around pH = 4) the monomers are almost fully associated. Therefore, the change in the electric potential  $\psi$  due to a monomer carrying the average absolute charge  $\alpha_i$  is small and the monomers are very similarly dissociated. With increasing pH, the average absolute charge  $\alpha_i$  increases. Around pH = 7, it is energetically more unfavorable for monomers close to a crosslink to dissociate (due to the increased number of neighbors at the crosslink). At very high pH (around pH = 9), chemical equilibrium dictates that the monomers need to be almost fully dissociated and the monomers along the chain are again more similarly dissociated.

## 6.6 Outlook: Weak Polyampholyte Gels

It is straightforward to apply the grand-reaction method presented in chapter 5 to periodic gels having monomers which take part in multiple chemical reactions, i.e. polyampholyte gels [153]. We perform periodic gel MD simulations in analogy to Section 6.1.1. The monomers in a polyampholyte gel can take part in an acid reaction



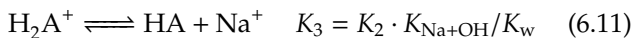
and a base reaction



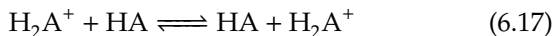
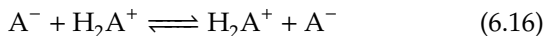
Without referring to a specific chemical substance we impose the following two reaction constants  $K_1 = 10^{-4}$  and  $K_2 = 10^{-10}$ .

For the first reaction (6.8), we use reactions (5.28), (5.29), (5.30) and (5.31) in our grand-reaction method.

For the second reaction (6.9), the following set of redundant reactions is introduced (in analogy to Section 5.4):



Particle swapping moves of the following kind are attempted



and accepted with the normal Metropolis criterion of Equation (2.58). As before, these moves help to equilibrate the charge profile along the polymer backbone if the number of other ions present is too small to mediate this swapping reaction.

The black curve in Figure 6.7 shows the non-monotonic swelling behavior of the polyampholyte gel which is in qualitative agreement with experimentally reported swelling curves [154, 155, 156, 157, 158]. In contrast to the acidic weak polyelectrolyte gel in Figure 6.3 a), this gel swells in acidic and basic environments but is collapsed around  $\text{pH} = 7$ . This behavior results from the charge of the gel which is shown in red in Figure 6.7. According



to Le Chatelier's principle, chemical equilibrium is "shifted" to the state  $\text{H}_2\text{A}^+$  at low pH. This results in a positively charged gel. At high pH the gel is negatively charged because the monomers are mostly in the state  $\text{A}^-$ . Around  $\text{pH} = 7$  the gel is charge neutral and contains both positively and negatively charged monomers  $\sum_{i \in \text{gel}} \langle q_i \rangle = 0$ . At this charge balance point, the ampholytic monomers carry on average zero charge. However, the fluctuating charges induce attractive Kirkwood-Shumaker interactions [159] between temporarily positively and negatively charged monomers. The attraction of the positive and negative charges along the polymer backbone collapses the gel. The swelling behavior is symmetric around  $\text{pH} = 7$  because the dissociation constants  $\text{p}K_1 = 4$  and  $\text{p}K_2 = 10$  have the same distance from  $\text{pH} = 7$ , namely  $|\text{p}K_i - 7| = 3$ . The decreased swelling at extreme pH ( $\text{pH} = 1$  and  $\text{pH} = 13$ ) is a result of the increased electrostatic screening and the osmotic pressure of the reservoir. This is similar to the reduced swelling of an acidic weak polyelectrolyte gel in Figure 6.3 a).

It could also be interesting to investigate the effect of hydrophobicity on the swelling of gels which is reported to cause a phase transition [112] when changing pH. We could also investigate gels with monomers taking part in reactions like  $\text{H}_n\text{A} \rightleftharpoons \text{A}^{n-} + n\text{H}^+$ . Here, we expect a charge fraction (i.e. pH) dependent collapse due to counterion condensation when the polyelectrolyte exceeds a critical charge fraction [160, 161].

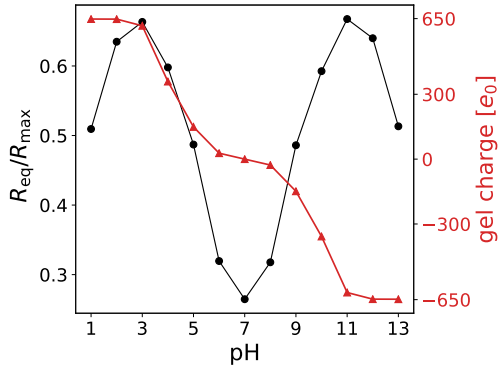


Figure 6.7: Swelling (in black) and gel charge (in red) of polyampholyte gel as a function of pH (for  $pK_1 = 4$ ,  $pK_2 = 10$ ,  $c_{salt}^{res} = 0.01\text{mol/L}$ ,  $N = 40$ ). Data are obtained from periodic gel MD simulations.

## 6.7 Summary

We demonstrated how to explicitly account for pH in three different gel models, namely the periodic gel model, the single-chain CGM and the PB CGM. In the two particle-based models we employed the previously introduced grand-reaction method. To our knowledge, it is the first time that weak polyelectrolyte gels were simulated in particle-based simulations. We generalized the PB CGM to make use of the charge regulation approach to model weak groups [5]. Key to modeling the pH and pOH correctly, is to account for the presence of all ions which influence the osmotic pressure of the reservoir and the electrostatic screening. In conclusion, we found that all three models can predict the experimentally reported collapse of weak polyelectrolyte gels at high pH and the non-monotonic swelling with reservoir salt

concentration.



---

## 7 Conclusion

We have laid out possible applications of hydrogels which span from superabsorbers in agriculture and hygiene products to pH sensors, desalination agents, mechanical actors and improved drug delivery (see Chapter 1). Common to all these use-cases is the need for selecting gels with fine-tuned properties to achieve optimal performance. This task is greatly simplified by applying accurate gel models for finding the optimal gel parameters: instead of tedious synthesis of lots of different gels, the gel with perfect properties is known from the start. Unfortunately, accurate analytical gel models with predictive power are not readily available and fundamental atomistic simulations of a gel have not been performed due to their excessive computational costs. The most fundamental gel simulations performed to-date are coarse-grained periodic gel simulations, where multiple atoms are grouped together to form a particle with effective interactions. However, these simplified simulations are still compute-intensive and a consistent description of the pH-dependent behavior of weak polyelectrolyte gels did not exist, up to now. In this light, the aims of this thesis were

- to introduce new, more efficient mean-field models for polyelectrolyte gels

- to develop methods for studying weak polyelectrolyte which carry a charge that depends on the pH of the environment
- to compare the different models to each other, as well to experiments, with respect to speed and accuracy.

After having outlined the relevant theory and justification for simulations in Chapter 2, we spent the rest of this thesis creating more efficient and reliable gel models: In Chapter 3, we significantly reduced the computational cost of performing particle-based simulations by the introduction of the single-chain cell-gel model (CGM). This simplified model has the advantage that it reduces the amount of particles which need to be simulated by factor 16 and, therefore, improves the computational efficiency by about one order of magnitude. At the same time the model is particle-based, which allowed us to use exactly the same interactions as in the periodic gel model, and hence also investigate specific ion effects (modeled via different short range interactions), poor solvent conditions, as well as the influence of multivalent ions. We found that the periodic gel model and the single-chain CGM agree very well with each other (see Section 3.6.2). Additionally, we demonstrated that the single-chain CGM is also applicable for highly charged gels or for low dielectric permittivity. This opens the door to faster and more cost-effective explorations of parameter spaces. To reduce the computational cost even further, we introduced the Poisson-Boltzmann cell-gel model (PB CGM) which replaces the particle-based description of a single chain with a density-based description. This comes at the cost of reduced accuracy but greatly increases the speed of the computations to a point where compute cluster become unnecessary,

---

since an individual simulation can be performed on a personal computer within seconds. Our new model is comparable to the Katchalsky model in efficiency, but has wider applicability because it can also be used to investigate highly charged gels, while the Katchalsky model fails for charge fractions  $f > 0.5$ . In addition, we demonstrated a simplistic approach of introducing chain length heterogeneity by assuming a mean-field factorization of the gel into separate cells containing only a single chain. These independent cells are then used to calculate the average degree of swelling of a polydisperse gel, with cells weighted according to their occurrence probability.

In Chapter 4, we have compared the periodic gel model and the PB CGM with experimental data of poly(sodium acrylate) hydrogels comprising different network topologies, including single networks (SN) and interpenetrating double networks (IPN). The comparison was performed at pH = 7 such that the gels can be treated as strong polyelectrolyte gels with charge fraction one. The swelling capacity of the gels in deionized water and sodium chloride solutions have been studied, where the absorbency  $Q_m$  decreased with higher salinities and more entanglements in the network caused by a higher degree of cross-linking or the incorporation of a second network. Furthermore, like the experimental results, our MD simulations showed that the water absorbency of an IPN is much smaller at low salinities compared to its related SN, whereas the differences between both network types vanish at higher salt concentrations. Although there are discrepancies between the reported experimental data and our simulations our models capture the main driving forces behind gel swelling. We attribute differences between the models and the experiments to the incomplete characterization of the

experimental gels: it is not clear which gel parameters are underlying the real gel such that it is hard to compare our models directly to experiments.

We introduced a new method in Chapter 5 termed the grand-reaction method, which is a robust tool for coarse-grained simulations of ionization equilibrium throughout the whole range of pH values. In these simulations pH and salt concentration are defined by the composition of the reservoir. Our implementation of particle exchanges with the reservoir avoids known artifacts and non-physical parameter combinations that have been used in previous studies. We showed that the grand-reaction method allows for the study of the combined effect of pH and reservoir ionic strength on the ionization and swelling of weak polyelectrolytes. In particular, it can correctly reproduce the experimentally known non-monotonic swelling as a function of pH which was previously not reproduced in particle-based simulations. Extensions of the grand-reaction method to a reservoir with more components, or to multiple chemical reactions in the system are straightforward.

In Chapter 6, we employed the grand-reaction method for simulations of weak polyelectrolyte gels in the periodic gel model and the single-chain CGM. Additionally, we use the charge regulation approach [5] to model weak polyelectrolyte gels in the PB CGM. Key to modeling the pH value correctly was to account for the presence of all ions which influence the osmotic pressure of the reservoir and the electrostatic screening. In conclusion, we found that all three models can predict the experimentally reported collapse of weak polyelectrolyte gels at high pH and the non-monotonic swelling with reservoir salt concentration.



---

The results presented introduce new very efficient gel models: the single chain CGM and the PB CGM. Both are computationally less demanding than the previously used periodic gel model. We hope that in the future our work will be useful for tailoring polyelectrolyte gels to their application.

During my PhD program, I also contributed to several publications which are connected to my work either through the fact that the systems contain reactive groups (i.e. the application of the reaction ensemble method) or the fact that they consider polyelectrolyte systems. The following publications were not discussed in this thesis:

- **J. Landsgesell**, C. Holm., J. Smiatek “Wang-Landau Reaction Ensemble Method: Simulation of Weak Polyelectrolytes and General Acid-Base Reactions” In: *Journal of Chemical Theory and Computation* 13(2)(852–862) (2017)

URL: <https://dx.doi.org/10.1021/acs.jctc.6b00791>

In this publication following my master thesis, we discuss a combination of the reaction ensemble method and the Wang-Landau sampling method which allows the enhanced sampling of rare protonation states. With this method we can obtain estimates for the density of states and the partition sum.

- **J. Landsgesell**, C. Holm, J. Smiatek. “Simulation of weak polyelectrolytes: A comparison between the constant pH and the reaction ensemble method” In: *The European Physical Journal Special Topics* 226(725–736) (2017)

URL: <https://dx.doi.org/10.1140/epjst/e2016-60324-3>

We compare the reaction ensemble method and the constant pH method (see Chapter 2). We show similarities between

both methods under certain conditions and pronounced differences for extreme pH values. These deviations are due to the presence of explicit protons in the reaction ensemble method inducing electrostatic screening effects.

- T. Richter, J. **Landsgesell**, P. Košován, C. Holm. “On the efficiency of a hydrogel-based desalination cycle” In: *Desalination* 414(28–34) (2017)

URL: <https://dx.doi.org/10.1016/j.desal.2017.03.027>

Polyelectrolyte gels swollen in seawater can release partially desalinated water when being compressed. Hence, they can be used as desalination agents. We use the Katchalsky model to analyse the thermodynamic costs of desalination, with a cycle which I proposed in analogy to the desalination experiments.

- D. Sean, J. **Landsgesell**, C. Holm. “Computer Simulations of Static and Dynamical Properties of Weak Polyelectrolyte Nanogels in Salty Solutions” In: *Gels* 4(2)(2) (2018)

URL: <https://dx.doi.org/10.3390/gels4010002>

With the help of my reaction-ensemble implementation in ESPResSo, we investigate the chemical equilibria of weak polyelectrolyte nanogels. Using the calculated mean-charge configurations of the nanogel from the reaction ensemble simulation as a quenched input to coupled lattice-Boltzmann molecular dynamics simulations, we investigate dynamical nanogel properties such as the electrophoretic mobility and the diffusion coefficient.

- J. **Landsgesell**, L. Nova, O. Rud, F. Uhlik, D. Sean, P. Hebbeker, C. Holm, P. Košován. “Simulations of ionization equilibria in weak polyelectrolyte solutions and gels” In:

---

*Soft Matter* 15(6)(1155-1185) (2019)

URL: <http://dx.doi.org/10.1039/C8SM02085J>

This article recapitulates the state of the art regarding simulations of ionization equilibria of weak polyelectrolyte solutions and gels, focusing on two methods: the constant pH ensemble and the reaction ensemble. We review the existing simulation literature and try to identify gaps and open problems.

- D. Sean, J. **Landsgesell**, C. Holm. “Influence of weak groups on polyelectrolyte mobilities” In: *Electrophoresis* 40(5)(799–809) (2019)

URL: <https://dx.doi.org/10.1002/elps.201800346>

With the help of my reaction-ensemble implementation in ESPResSo, we investigate the inhomogeneous ionization in weak polyelectrolytes and the effect of the resulting charge profile on the electrophoretic mobility. An ensemble pre-average is used to obtain the effective charge profile for linear, rod-like and flexible four-arm star polyelectrolytes. Using molecular dynamics simulations within a Lattice-Boltzman fluid, we investigate how the electrophoretic mobility is affected by the average dissociation profile. We find that the mobility is almost unaltered due to counter-ion condensation effects.

- F. Weik, R. Weeber, K. Szuttor, K. Breitsprecher, J. de Graaf, M. Kuron J. **Landsgesell**, H. Menke, D. Sean, C. Holm, “ESPResSo 4.0 – an extensible software package for simulating soft matter systems” In: *The European Physical Journal Special Topics* 227(14)(1789–1816) (2019)

URL: <http://dx.doi.org/10.1140/epjst/e2019-800186-9>

We present our new Python interface which replaces the older Tcl scripting interface. In addition, many new simulation methods have been implemented. I added several methods handy for simulations of systems with fluctuating particle numbers: the reaction ensemble method, the constant pH method, Widom's insertion method and the H5MD output format [162].

- F. Weik, K. Szuttor, **J. Landsgesell**, C. Holm. "Modeling the current modulation of dsDNA in nanopores – from mean-field to atomistic and back" In: *The European Physical Journal Special Topics* 227(14)(1639–1655) (2019)

URL: <https://dx.doi.org/10.1140/epjst/e2019-800189-3>

All-atom molecular dynamics (MD) simulations of double stranded DNA translocating through a cylindrical nanopore have revealed that ions close to the surface of the DNA experience an additional friction contribution when compared to their bulk value. We present an extended electrokinetic model with such a friction for describing the behavior of a DNA confined to a cylindrical pore. In radial direction the mobile ions are distributed similarly to my PB cell-gel model [102, 2].

- J. Finkbeiner, **J. Landsgesell**, C. Holm. "Dilution Behaviour of Weak Acids Under the Influence of Strong Electrostatic Interactions" *In preparation*

We observe that under the influence of strong electrostatic interactions the dilution behavior is modified compared to an ideal solution: While ideal solutions follow the law of dilution (i.e. become more dissociated the more diluted they are and vice versa become less dissociated the more

---

concentrated they are), we observe an enhanced dissociation with increasing concentration of weak acids under the influence of strong electrostatic interactions. Following my ideas, we can attribute this “abnormal” dissociation behavior to excess contributions of the chemical potential. This behavior resembles the non-monotonic dissociation found in experiments [163], where our simulations could be compared to recently proposed charge regulation theories [164, 165].

- A. Tagliabue, J. **Landsgesell**, M. Mella, C. Holm. “On the Formation of Electrostatically Cross-linked Gels via Self-assembly of Charged Star-shaped Copolymers” *In preparation*

In this work we investigate the possibility to form (meta)stable networks (i.e., gels) by oppositely charged star-shaped diblock polyelectrolytes. We simulated electroneutral mixtures of positively and negatively charged stars with four arms carrying a varying number of charged terminal monomers. We find stable gel phases if the stars have more than two terminal charges per arm. These physically crosslinked gels can be analyzed in analogy to the periodic gel model presented in Section 2.6.2.



---

## 8 Appendix

### 8.1 Directory Structure: Simulation Scripts and Figures

The simulation scripts used in this thesis are documented in the following folder:

```
simulation_scripts
├── MD
│   ├── periodic_gel
│   └── single_chain_CGM
└── PB
```

Figures are located in the folder

```
figures
├── copied_plots_XYZ
└── thesis
```

They are generated in the corresponding git repositories of the papers and are then copied to the thesis (except for figures which were only generated for this thesis).

## 8.2 Polymer Monomer Distribution in the Poisson-Boltzmann Cell-Gel Model

In the spirit of hierarchical multiscale modeling [16] we use results from the more detailed single-chain cell-gel model (CGM) to motivate the fixed charge density  $\rho_f(\vec{r}) = -Nfp(\vec{r})$  which needs to be defined for the Poisson-Boltzmann CGM (PB CGM). We impose different forms of the probability density (Heaviside vs approximately Gaussian) and match the first moment to single-chain CGM, i.e. the average distance from the end to end vector. To this end, we perform single-chain CGM simulations and record the distance  $r$  of each monomer from the cylinder axis. We therefore obtain the average distance from the cylinder axis  $\langle r \rangle_{\text{MD}}$  which depends on the stretching state  $R_e$  of the polymer: for highly stretched gels the chain configuration resembles a rod, for barely stretched gels, we get a more fluffy chain conformation.

From the single-chain CGM data, we extract the parameters for fitting a curve for the average distance  $\langle r \rangle_{\text{MD}}$  of the monomers from the cylinder axis as a function of  $R_e$ :

$$\langle r \rangle_{\text{MD}}(R_e) = N\sigma \left( C_1 \left( \frac{R_e}{N\sigma} \right)^2 + C_2 \frac{R_e}{N\sigma} + C_3 \right). \quad (8.1)$$

From fitting (for a fully charged chain without added salt,  $N \in \{39, 79, 300\}$  and  $\epsilon_r = 80$ ), we obtain the constants  $C_1 = -0.17$ ,  $C_2 = 0.14$  and  $C_3 = 0.03$ . The data to which we fit and the fitted master curve are shown in figure 8.1 a). The fit goes through the data reasonably well (considering fluctuations  $\sqrt{\text{Var}(r)}$  which are shown as bars). Figure 8.1 b) shows the application of the obtained master curve to other parameters than the ones which



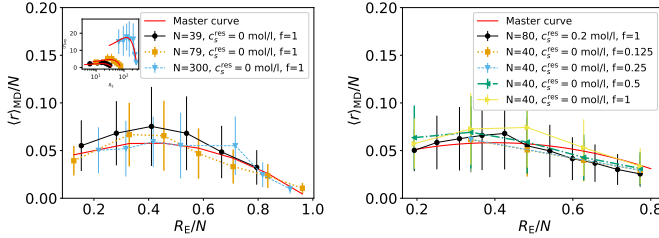


Figure 8.1: Figure a) shows the master curve which was obtained from fitting to the data at charge fraction  $f = 1$  and salt concentration  $c_{salt}^{res} = 0$ . The inset shows the unscaled data (at same parameters). Figure b) shows the master curve applied to data sets which were not included in the fitting process. In both figures the bars show the standard deviation of the data points.

were used for the fitting. It can be seen that the master curve captures the trend of  $\langle r \rangle_{MD}(R_E)$  within fluctuations. Although the conformation of the chain depends on other parameters like charge fraction and salt concentration, we follow the simplistic approach and use the obtained fit parameters for all parameter combinations.

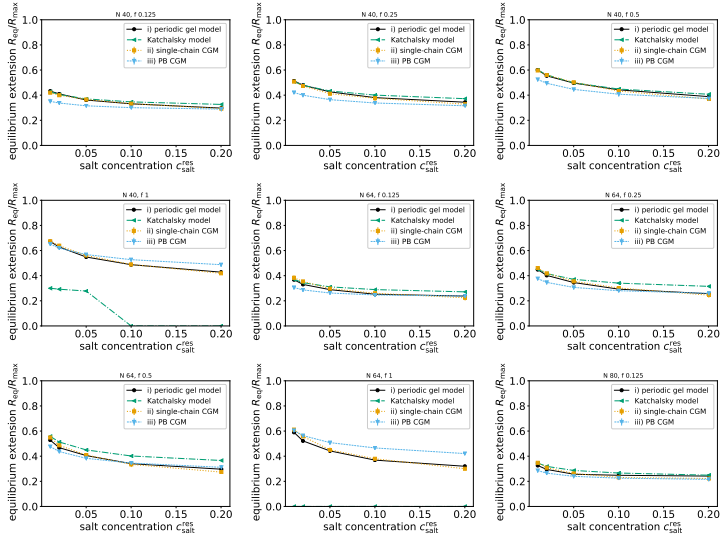
## 8.3 Strong Polyelectrolyte Gels

### 8.3.1 Swelling Equilibria

For completeness, we show the swelling equilibria as a function salt concentration  $c_{salt}$ , charge fraction  $f$  and chain length  $N$ . The plots are analogous to the plots in Figure 3.5b. For parameters where the Katchalsky model predicts more than one zero crossing

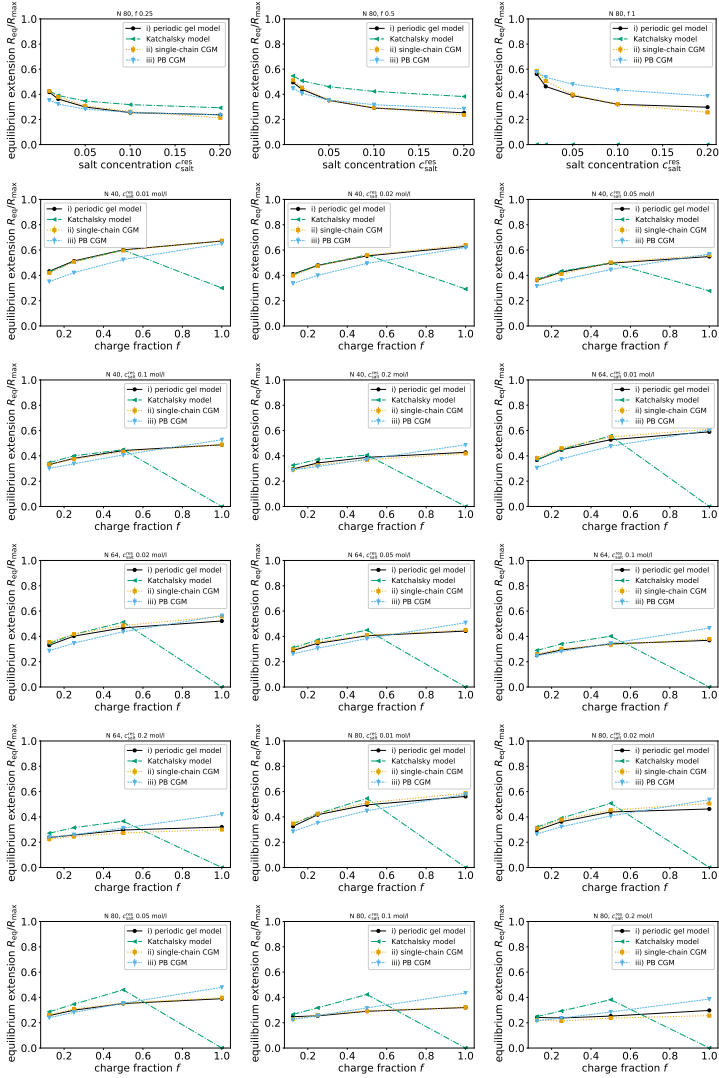
in the  $PV$  curve, the corresponding value of  $R_{eq}$  is set to zero (in order to indicate failure).

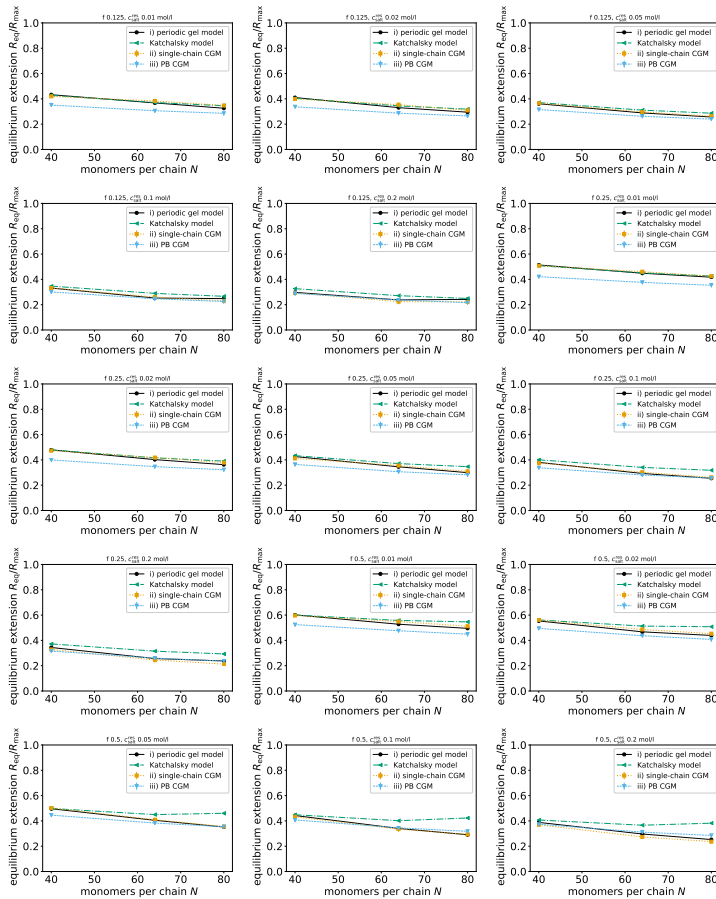
## Salt Concentration Dependence



## Charge Fraction Dependence

## 8.3 Strong Polyelectrolyte Gels

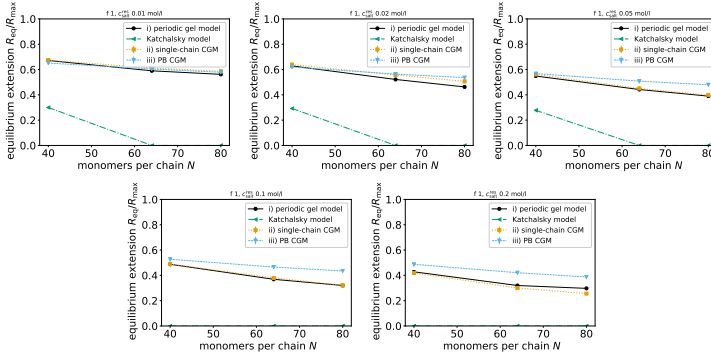




## Chain Length Dependence

### 8.3.2 Comparison of the CGMs to the Periodic Gel Model

We compare the swelling predictions of the two CGMs and the Katchalsky model to the periodic gel model predictions in a



parametric plot (similar to figure 3.7). We separately show the data for two data sets A: ( $N = 40, f = 0.125, c_{\text{salt}} \in \{0.01, 0.02, 0.05, 0.1, 0.2\} \text{ mol/l}$ ) and B: ( $N = 80, f = 1, c_{\text{salt}} \in \{0.01, 0.02, 0.05, 0.1, 0.2\} \text{ mol/l}$ ) in figures 8.2a and 8.2b.

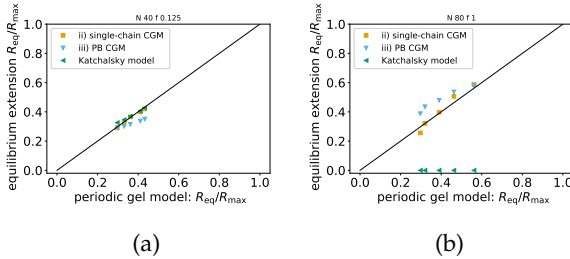


Figure 8.2: a) Data set A:  $N=40, f=0.125$ , different salt concentrations. b) Data set B:  $N=80, f=1$ , different salt concentrations. In each figure the highest salt concentration 0.2 mol/l is associated with the lowest swelling. Reducing the salt concentration increases the swelling. The Katchalsky model fails for  $f=1$ . To illustrate this failure, we set the predicted swelling to  $R_{\text{eq}}/R_{\text{max}} = 0$ .

Plotting both data sets A and B together, like we do it in figure 3.7 gives figure 8.3 below:

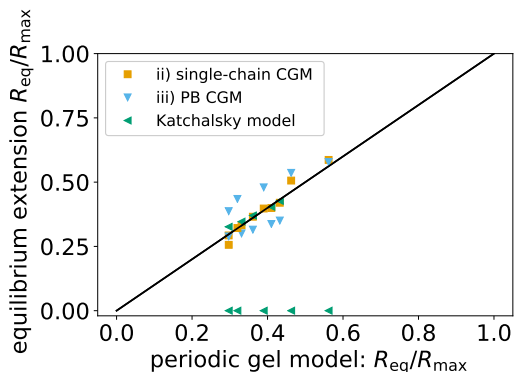


Figure 8.3: Data sets A and B from figures 8.2a and 8.2b plotted together. This plot is similar to figure 5 in the manuscript but contains only 1/6 of the data sets.

The projection of the predictions from a three-dimensional parameter space on one abscissa results in an apparent “scattering” of data around the ideal prediction (although the models do not scatter when plotting one data set alone). This indicates that the different models perform differently well in different parts of the parameter space.

## 8.4 Charge Fraction Dependence of the Swelling of Single Gels and Interpenetrating Gels

The data shown here supplement the data presented in section 4.5. The data are obtained from periodic gel MD simulations. In figure 8.4 we show the behaviour of SNP and IPNs for different

## 8.4 Charge Fraction Dependence of the Swelling of Single Gels and Interpenetrating Gels

charge fractions. This is an example, where we harness that simulations have predictive power and are easier to perform than experiments. We observe that SNPs and IPNs swell differently.

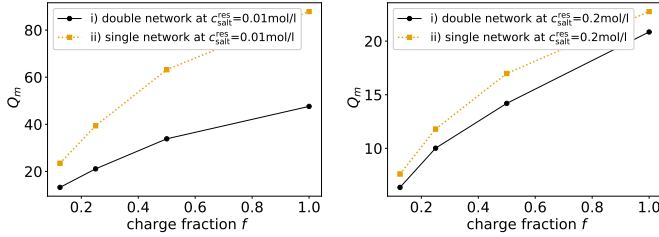


Figure 8.4: The mass based degree of swelling of both double and single networks at varying charge fraction and fixed chain length  $N = 40$  and concentrations of the supernatant solution as indicated in the legend.





---

## 9 Acknowledgement

I wish to thank Dr. Tobias Richter, Dr. David Sean, Dr. Peter Košovan, Dr. Oleg Rud, Dr. Pascal Hebbeker, PD Dr. Jens Smiatek, Kai Szuttor, Dr. Konrad Breitsprecher, Patrick Kreissl and others at the ICP for helpful discussions. Especially, I am grateful for a very insightful discussion on classical density functional theory with Prof. Dr. Markus Bier and for interesting discussions on Kirkwood-Shumaker interactions with Prof. Dr. Rudolf Podgornik. Also, I appreciate Dr. Georg Rempfer and Florian Weik for having pointed out the fact that pressures in electric environments are best described using the Maxwell stress tensor formalism. Many thanks also go to Martin Fischer and Jan Finkbeiner for being interested in my research topics and for writing their bachelor thesis with me. Further, I would like to thank Prof. Dr. Christian Holm for giving me the opportunity to write my PhD thesis at the Institute for Computational Physics.

Of course, I also want to give special tribute my family who supported me.

I am particularly grateful for the great times I have had with the friends I made during my studies, especially (without special ordering)

## 9 Acknowledgement

---

- Anissa Blödorn
- Norbert Witz
- Marco Ströbel
- Sebastian Weber
- Felix Huber
- Tim Opferkuch
- Dr. Dominic Röhm
- Michael Schmid
- Bianca Haszler
- Kai Szuttor
- Kai Phillipi
- Tizian Wenzel
- Daniel Ferbach
- David Ürek
- Matze Schmidt
- Simon Dambach
- Clemens Baier
- Martin Fischer
- Benjamin Wagner
- Daniel Peña
- Dr. Andreas Löhle
- Benjamin Seethaler
- Annika & Christoph Gomringer
- Konstantin Nikolaou
- Michael Iliewicz
- Benedikt Herkommer
- Elias Arnold
- Sven Ilse
- Jonas Binz
- McLovin
- Markus Eberhard
- Pamela Bournigal
- Niklas Liebermann
- Ioannis Caltzidis
- Vincent Fritz
- Michael Öchsle
- Tillman Kleiner
- Thomas Klumpp
- Robert Sittig
- Manuel Abele
- Maximilian Voigt

---

I am very sure I forgot friends in this list and I blame the limited time I had for writing it. For those on the list, and for those I forgot to name: The next evening is on me! Please remind me if I forget :)

I also want to thank my friends, who made my stay in Los Alamos a blast and one of my best summers:

- |                             |                        |                             |
|-----------------------------|------------------------|-----------------------------|
| • Jamie Alexis<br>Merizalde | • Mackenzie<br>Mathews | • Dr. Christoph<br>Junghans |
| • Ebraheem<br>Farag         | • Nate Bieber-<br>dorf | • Collin McCle-<br>nahan    |
| • Matt Price-<br>Williams   | • Emrys Peets          | • Tanner<br>Kennedy         |
| • Jordan Noble              | • Kayleen<br>Noelle    | • Bill & Nicole<br>Dunn     |
| • Josh Plasse               | • Vinay Bharad-<br>waj |                             |

I hope that our paths cross again in the future!



# Bibliography

- [1] T. Richter, "Coarse grained hydrogels," Ph.D. dissertation, 2017.
- [2] J. Landsgesell and C. Holm, "Cell model approaches for predicting the swelling and mechanical properties of polyelectrolyte gels," *Macromolecules*, 2019.
- [3] P. Košován, T. Richter, and C. Holm, "Modeling of polyelectrolyte gels in equilibrium with salt solutions," *Macromolecules*, vol. 48, no. 20, pp. 7698–7708, 2015.
- [4] J. Landsgesell, C. Holm, and J. Smiatek, "Simulation of weak polyelectrolytes: A comparison between the constant pH and the reaction ensemble method," *The European Physical Journal Special Topics*, vol. 226, pp. 725–736, 2017.
- [5] B. W. Ninham and V. A. Parsegian, "Electrostatic potential between surfaces bearing ionizable groups in ionic equilibrium with physiologic saline solution," *Journal of Theoretical Biology*, vol. 31, no. 3, pp. 405–428, Jun. 1971.  
[Online]. Available: <http://www.sciencedirect.com/science/article/pii/0022519371900191>
- [6] M. J. Zohuriaan-Mehr, H. Omidian, S. Doroudiani, and

- K. Kabiri, "Advances in non-hygienic applications of superabsorbent hydrogel materials," *Journal of Materials Science*, vol. 45, no. 21, pp. 5711–5735, Nov. 2010.
- [7] K. Kazanskii and S. Dubrovskii, "Chemistry and physics of agricultural hydrogels," in *Polyelectrolytes Hydrogels Chromatographic Materials. Advances in Polymer Science*. Springer Verlag, 1992, vol. 104, pp. 97–133.
- [8] J. Höpfner, C. Klein, and M. Wilhelm, "A novel approach for the desalination of seawater by means of reusable poly(acrylic acid) hydrogels and mechanical force," *Macromolecular Rapid Communications*, vol. 31, p. 1337, 2010.
- [9] J. Höpfner, "A new method of seawater desalination via acrylic acid based hydrogels: Synthesis, characterisation, and experimental realisation," Ph.D. dissertation, Karlsruher Institut für Technologie (KIT), 2013.
- [10] J. Höpfner, T. Richter, P. Košovan, C. Holm, and M. Wilhelm, "Seawater desalination via hydrogels: Practical realisation and first coarse grained simulations," in *Intelligent Hydrogels*, ser. Progress in Colloid and Polymer Science, G. Sadowski and W. Richtering, Eds. Springer International Publishing, 2013, vol. 140, pp. 247–263. [Online]. Available: <https://www.springer.com/chemistry/polymer+science/book/978-3-319-01682-5>
- [11] A. Richter, G. Paschew, S. Klatt, J. Lienig, K.-F. Arndt, and H.-J. P. Adler, "Review on hydrogel-based pH sensors and microsensors," *Sensors*, vol. 8, no. 1, pp. 561–581, Jan. 2008.

- 
- [12] L. Arens, F. Weißenfeld, C. O. Klein, K. Schlag, and M. Wilhelm, "Osmotic engine: Translating osmotic pressure into macroscopic mechanical force via poly (acrylic acid) based hydrogels," *Advanced Science*, vol. 4, no. 9, p. 1700112, 2017.
- [13] F. Ganji, F. S. Vasheghani, and F. E. VASHEGHANI, "Theoretical description of hydrogel swelling: a review," 2010.
- [14] J. Li and D. J. Mooney, "Designing hydrogels for controlled drug delivery," *Nature Reviews Materials*, vol. 1, no. 12, p. 16071, 2016.
- [15] G. A. Voth, *Coarse-graining of condensed phase and biomolecular systems*. CRC press, 2008.
- [16] S. A. Baeurle, "Multiscale modeling of polymer materials using field-theoretic methodologies: a survey about recent developments," *Journal of Mathematical Chemistry*, vol. 46, no. 2, pp. 363–426, 2009.
- [17] R. R. Netz and H. Orland, "Variational charge renormalization in charged systems," *The European Physical Journal E*, vol. 11, no. 3, pp. 301–311, 2003.
- [18] D. Frenkel and B. Smit, *Understanding Molecular Simulation*, 2nd ed. San Diego: Academic Press, 2002.
- [19] C. Heath Turner, J. K. Brennan, M. Lisal, W. R. Smith, J. Karl Johnson, and K. E. Gubbins, "Simulation of chemical reaction equilibria by the reaction ensemble monte carlo method: a review," *Molecular Simulation*, vol. 34, no. 2, pp. 119–146, 2008.

- [20] M. Sastre and J. Santaballa, "A note on the meaning of the electroneutrality condition for solutions," *Journal of Chemical Education*, vol. 66, no. 5, p. 403, 1989.
- [21] P. W. Atkins and J. de Paula, *Physical Chemistry*. Oxford (UK): Oxford Univ. Press, 2010.
- [22] McNaught and Wilkinson, *IUPAC. Compendium of Chemical Terminology, 2nd ed. (the "Gold Book")*, 1997.  
[Online]. Available: <http://goldbook.iupac.org>
- [23] T. Markovich, D. Andelman, and R. Podgornik, *Charged Membranes: Poisson-Boltzmann theory, DLVO paradigm and beyond*. Taylor & Francis / CRC Press, 2016, ch. 1.
- [24] M. Deserno and C. Holm, "Cell-model and poisson-boltzmann-theory: A brief introduction," in *Electrostatic Effects in Soft Matter and Biophysics*, ser. NATO Science Series II - Mathematics, Physics and Chemistry, C. Holm, P. Kélicheff, and R. Podgornik, Eds. Dordrecht, NL: Kluwer Academic Publishers, Dec. 2001, vol. 46, pp. 27–50.
- [25] N. Laanait, "Ion correlations at electrified soft matter interfaces," Ph.D. dissertation, 2013.
- [26] D. Andelman, *Handbook of Biological Physics*. School of Physics and Astronomy, Tel Aviv University, 1995, ch. 12, p. 603.
- [27] M. Deserno, C. Holm, and S. May, "Fraction of condensed counterions around a charged rod: Comparison of Poisson-Boltzmann theory and computer simulations," *Macromolecules*, vol. 33, pp. 199–206, 2000.



- [28] E. Trizac and J.-P. Hansen, "Wigner-seitz model of charged lamellar colloidal dispersions," *Physical Review E*, vol. 56, p. 3137, 1997.
- [29] S. Oversteegen, P. Barneveld, F. Leermakers, and J. Lyklema, "On the pressure in mean-field lattice models," *Langmuir*, vol. 15, no. 25, pp. 8609–8617, 1999.
- [30] A. Widom, J. Swain, J. Silverberg, S. Sivasubramanian, and Y. Srivastava, "Theory of the maxwell pressure tensor and the tension in a water bridge," *Physical Review E*, vol. 80, no. 1, p. 016301, 2009.
- [31] H. Wennerström, B. Jönsson, and P. Linse, "The cell model for polyelectrolyte systems. exact statistical mechanical relations, monte carlo simulations, and the poisson–boltzmann approximation," *Journal of Chemical Physics*, vol. 76, p. 4665, 1982.
- [32] J. W. Eastwood, "Optimal particle-mesh algorithms," *Journal of Computational Physics*, vol. 18, pp. 1–20, 1975.
- [33] J. Eastwood, *Computational methods in classical and quantum physics*. Advance Publications Limited, 1976, ch. Optimal P<sup>3</sup>M Algorithms For Molecular Dynamcis Simulations, pp. 206–228.
- [34] A. Y. Toukmaji and J. A. Board Jr., "Ewald summation techniques in perspective: a survey," *Computer Physics Commications*, vol. 95, pp. 73–92, 1996.
- [35] J. D. Weeks, D. Chandler, and H. C. Andersen, "Role of repulsive forces in determining the equilibrium structure of simple liquids," *The Journal of Chemical Physics*, vol. 54,

p. 5237, 1971.

- [36] G. S. Grest and K. Kremer, "Molecular dynamics simulation for polymers in the presence of a heat bath," *Physical Review A*, vol. 33, no. 5, pp. 3628–31, 1986.
- [37] M. P. Allen and D. J. Tildesley, *Computer Simulation of Liquids*, 1st ed., ser. Oxford Science Publications. Oxford: Clarendon Press, 1987.
- [38] N. Metropolis *et al.*, "The beginning of the monte carlo method," *Los Alamos Science*, no. 584, pp. 125–130, 1987.
- [39] N. Metropolis, A. W. Rosenbluth, M. N. Rosenbluth, A. H. Teller, and E. Teller, "Equation of state calculations by fast computing machines," *Journal of Chemical Physics*, vol. 21, no. 6, p. 1087, 1953, the original paper of the Metropolis algorithm.
- [40] W. K. Hastings, "Monte carlo sampling methods using markov chains and their applications," 1970.
- [41] L. J. LaBerge and J. C. Tully, "A rigorous procedure for combining molecular dynamics and monte carlo simulation algorithms," *Chemical Physics*, vol. 260, no. 1-2, pp. 183–191, 2000.
- [42] E. C. Neyts and A. Bogaerts, "Combining molecular dynamics with monte carlo simulations: implementations and applications," in *Theoretical Chemistry in Belgium*. Springer, 2014, pp. 277–288.
- [43] J. P. Valleau and L. K. Cohen, "Primitive model electrolytes. i. grand canonical monte carlo computations,"

- The Journal of Chemical Physics*, vol. 72, no. 11, pp. 5935–5941, 1980. [Online]. Available: <http://scitation.aip.org/content/aip/journal/jcp/72/11/10.1063/1.439092>
- [44] D. Frenkel, “Advanced monte carlo techniques,” pp. 93–152, 1993.
- [45] A. H. Truesdell, “Activity coefficients of aqueous sodium chloride from 15° to 50°c measured with a glass electrode,” *Science*, vol. 161, no. 3844, pp. 884–886, 1968. [Online]. Available: <http://www.sciencemag.org/content/161/3844/884.abstract>
- [46] J. M. Prausnitz, R. N. Lichtenthaler, and E. G. de Azevedo, *Molecular Thermodynamics of Fluid Phase Equilibria*. Prentice Hall, 1999.
- [47] E. R. Smith, “Calculating the pressure in simulations using periodic boundary conditions,” *Journal of Statistical Physics*, vol. 77, pp. 449–472, 1994.
- [48] C. E. Reed and W. F. Reed, “Monte carlo study of titration of linear polyelectrolytes,” *Journal of Chemical Physics*, vol. 96, p. 1609, 1992.
- [49] M. Ullner, B. Jönsson, B. Soderberg, and C. Peterson, “A monte carlo study of titrating polyelectrolytes,” *Journal of Chemical Physics*, vol. 104, no. 8, pp. 3048–3057, 1996.
- [50] M. Ullner and B. Jönsson, “A monte carlo study of titrating polyelectrolytes in the presence of salt,” *Macromolecules*, vol. 29, no. 20, pp. 6645–6655, 1996.
- [51] B. Jönsson, M. Ullner, C. Peterson, O. Sommelius, and

- B. Södeberg, "Titrating polyelectrolytes – variational calculations and Monte Carlo simulations," *Journal of Physical Chemistry*, vol. 100, pp. 409–417, 1996.
- [52] F. Carnal and S. Stoll, "Adsorption of weak polyelectrolytes on charged nanoparticles. impact of salt valency, ph, and nanoparticle charge density. monte carlo simulations," *The Journal of Physical Chemistry B*, vol. 115, no. 42, pp. 12 007–12 018, 2011.
- [53] J. Landsgesell, L. Nova, O. Rud, F. Uhlik, D. Sean, P. Hebbeker, C. Holm, and P. Košován, "Simulations of ionization equilibria in weak polyelectrolyte solutions and gels," *Soft Matter*, vol. 15, no. 6, pp. 1155–1185, 2019.
- [54] F. Weik, R. Weeber, K. Szuttor, K. Breitsprecher, J. de Graaf, M. Kuron, J. Landsgesell, H. Menke, D. Sean, and C. Holm, "ESPResSo 4.0 – an extensible software package for simulating soft matter systems," *The European Physical Journal Special Topics*, vol. 227, no. 14, pp. 1789–1816, 2019. [Online]. Available: <https://link.springer.com/epdf/10.1140/epjst/e2019-800186-9>
- [55] K. Kremer and G. S. Grest, "Dynamics of entangled linear polymer melts: A molecular-dynamics simulation," *Journal of Chemical Physics*, vol. 92, no. 8, pp. 5057–5086, 1990.
- [56] M. Deserno and C. Holm, "How to mesh up Ewald sums. I. A theoretical and numerical comparison of various particle mesh routines," *Journal of Chemical Physics*, vol. 109, p. 7678, 1998.

- [57] —, “How to mesh up Ewald sums. II. An accurate error estimate for the Particle-Particle-Particle-Mesh algorithm,” *Journal of Chemical Physics*, vol. 109, p. 7694, 1998.
- [58] M. Rubinstein and R. H. Colby, *Polymer Physics*. Oxford, UK: Oxford University Press, 2003.
- [59] G. Strobl, *The Physics of Polymers*, 3rd ed. Springer, 2007.
- [60] M. Rubinstein and P. S., “Elasticity of polymer networks,” *Macromolecules*, vol. 35, no. 17, pp. 6670–6686, 2002.
- [61] F. G. Donnan, “The theory of membrane equilibria.” *Chemical Reviews*, vol. 1, no. 1, pp. 73–90, 1924. [Online]. Available: <http://pubs.acs.org/doi/abs/10.1021/cr60001a003>
- [62] P. J. Flory and J. John Rehner, “Statistical mechanics of cross-linked polymer networks ii. swelling,” *The Journal of Chemical Physics*, vol. 11, no. 11, pp. 521–526, 1943.
- [63] A. Katchalsky and I. Michaeli, “Polyelectrolyte gels in salt solutions,” *Journal of Polymer Science*, vol. 15, p. 69, 1955.
- [64] S. Schneider and P. Linse, “Swelling of cross-linked polyelectrolyte gels,” *The European Physical Journal E*, vol. 8, pp. 457–460, 2002.
- [65] S. Edgecombe, S. Schneider, and P. Linse, “Monte carlo simulations of defect-free cross-linked gels in the presence of salt,” *Macromolecules*, vol. 37, no. 26, pp. 10 089–10 100, 2004. [Online]. Available: <http://pubs.acs.org/doi/abs/10.1021/ma0486391>
- [66] D.-W. Yin, F. Horkay, J. F. Douglas, and J. J. de Pablo, “Molecular simulation of the swelling of polyelectrolyte

- gels by monovalent and divalent counterions," *Journal of Chemical Physics*, vol. 129, no. 15, Oct. 2008.
- [67] D.-W. Yin, M. O. de la Cruz, and J. J. de Pablo, "Swelling and collapse of polyelectrolyte gels in equilibrium with monovalent and divalent electrolyte solutions," *Journal of Chemical Physics*, vol. 131, no. 19, pp. 194 907–6, Nov. 2009.
- [68] G. S. Longo, M. O. de la Cruz, and I. Szleifer, "Molecular theory of weak polyelectrolyte gels: The role of pH and salt concentration," *Macromolecules*, vol. 44, pp. 147–158, 2011.
- [69] B. A. Mann, R. Everaers, C. Holm, and K. Kremer, "Scaling in polyelectrolyte networks," *Europhysics Letters*, vol. 67, no. 5, pp. 786–792, 2004.
- [70] B. A. Mann, C. Holm, and K. Kremer, "Swelling of polyelectrolyte networks," *Journal of Chemical Physics*, vol. 122, no. 15, p. 154903, 2005.
- [71] B. Mann, C. Holm, and K. Kremer, "The swelling behaviour of charged hydrogels," *Macromolecular Symposia*, vol. 237, pp. 90–107, 2006.
- [72] B. A. Mann, O. Lenz, K. Kremer, and C. Holm, "Hydrogels in poor solvents: A molecular dynamics study," *Macromolecular Theory and Simulations*, vol. 20, pp. 721–734, 2011, cover Issue.
- [73] M. Quesada-Pérez, J. G. Ibarra-Armenta, and A. Martín-Molina, "Computer simulations of thermo-shrinking polyelectrolyte gels," *The Journal of Chemical Physics*, vol. 135, no. 9, p. 094109, 2011.

- [74] M. Quesada-Pérez, J. Ramos, J. Forcada, and A. Martín-Molina, "Computer simulations of thermo-sensitive microgels: Quantitative comparison with experimental swelling data," *The Journal of Chemical Physics*, vol. 136, no. 24, p. 244903, 2012.
- [75] M. Quesada-Pérez, J. A. Maroto-Centeno, and A. Martín-Molina, "Effect of the counterion valence on the behavior of thermo-sensitive gels and microgels: A monte carlo simulation study," *Macromolecules*, vol. 45, no. 21, pp. 8872–8879, 2012. [Online]. Available: <http://pubs.acs.org/doi/abs/10.1021/ma3014959>
- [76] P. Košován, T. Richter, and C. Holm, "Molecular simulations of hydrogels," in *Intelligent Hydrogels*, ser. Progress in Colloid and Polymer Science, G. Sadowski and W. Richtering, Eds. Springer International Publishing, 2013, vol. 140, pp. 205–221. [Online]. Available: <https://www.springer.com/chemistry/polymer+science/book/978-3-319-01682-5>
- [77] A. Philipse and A. Vrij, "The donnan equilibrium: I. on the thermodynamic foundation of the donnan equation of state," *Journal of Physics: Condensed Matter*, vol. 23, no. 19, p. 194106, 2011. [Online]. Available: <http://stacks.iop.org/0953-8984/23/i=19/a=194106>
- [78] M. van Dijk and A. Wakker, *Concepts in Polymer Thermodynamics*. Taylor & Francis, 1998, no. Bd. 2. [Online]. Available: <https://books.google.de/books?id=E1ej3Ue2U8AC>
- [79] U. Essmann, L. Perera, M. L. Berkowitz, T. Darden, H. Lee,

- and L. Pedersen, "A smooth Particle Mesh Ewald method," *Journal of Chemical Physics*, vol. 103, p. 8577, 1995.
- [80] T. Hill, *An Introduction to Statistical Thermodynamics*, ser. Addison-Wesley series in chemistry. Dover Publications, 1986. [Online]. Available: <https://books.google.de/books?id=QttFDwAAQBAJ>
- [81] P. J. Flory and J. Rehner, "Statistical mechanics of crosslinked polymer networks i. rubberlike elasticity," *Journal of Chemical Physics*, vol. 11, p. 512, 1943.
- [82] A. R. Khokhlov, S. G. Starodubtzev, and V. V. Vasilevskaya, "Responsive gels: Volume transitions I," in *Conformational transitions in polymer gels: theory and experiment*, ser. Adv. Polym. Sci., K. Dušek, Ed. New York: Springer Verlag, 1993, vol. 109, p. 123.
- [83] M. Rubinstein, R. H. Colby, A. V. Dobrynin, and J. F. Joanny, "Elastic modulus and equilibrium swelling of polyelectrolyte gels," *Macromolecules*, vol. 29, no. 1, pp. 398–406, 1996.
- [84] G. C. Claudio, K. Kremer, and C. Holm, "Comparison of a hydrogel model to the poisson-boltzmann cell model," *The Journal of Chemical Physics*, vol. 131, no. 9, p. 094903, Sep. 2009.
- [85] M. Quesada-Pérez, J. A. Maroto-Centeno, J. Forcada, and R. Hidalgo-Alvarez, "Gel swelling theories: the classical formalism and recent approaches," *Soft Matter*, vol. 7, pp. 10 536–10 547, 2011.
- [86] P. K. Jha, J. W. Zwanikken, J. J. de Pablo, and M. O. de la



- Cruz, "Electrostatic control of nanoscale phase behavior of polyelectrolyte networks," *Current Opinion in Solid State and Materials Science*, vol. 15, no. 6, pp. 271 – 276, 2011, functional Gels and Membranes. [Online]. Available: <http://www.sciencedirect.com/science/article/pii/S1359028611000441>
- [87] A. J. Liu, G. S. Grest, M. C. Marchetti, G. M. Grason, M. O. Robbins, G. H. Fredrickson, M. Rubinstein, and M. O. de la Cruz, "Opportunities in theoretical and computational polymeric materials and soft matter," *Soft Matter*, vol. 11, no. 12, pp. 2326–2332, 2015.
- [88] Q. Yan and J. J. de Pablo, "Monte carlo simulation of a coarse-grained model of polyelectrolyte networks," *Physical Review Letters*, vol. 91, no. 1, p. 018301, Jul. 2003.
- [89] D.-W. Yin, Q. Yan, and J. J. de Pablo, "Molecular dynamics simulation of discontinuous volume phase transitions in highly-charged crosslinked polyelectrolyte networks with explicit counterions in good solvent," *The Journal of Chemical Physics*, vol. 123, no. 17, p. 174909, 2005.
- [90] O. Rud, T. Richter, O. Borisov, C. Holm, and P. Košovan, "A self-consistent mean-field model for polyelectrolyte gels," *Soft Matter*, vol. 13, no. 18, pp. 3264–3274, 2017.
- [91] A. Gavrillov and A. Chertovich, "Computer simulation of random polymer networks: Structure and properties," *Polymer Science Series A*, vol. 56, no. 1, pp. 90–97, 2014.
- [92] C. Svaneborg, G. S. Grest, and R. Everaers, "Disorder effects on the strain response of model polymer networks,"

- Polymer*, vol. 46, no. 12, pp. 4283–4295, 2005.
- [93] S. Edgecombe and P. Linse, "Monte carlo simulation of polyelectrolyte gels: Effects of polydispersity and topological defect," *Macromolecules*, vol. 40, no. 10, pp. 3868–3875, May 2007.
- [94] B. A. Mann, "The swelling behaviour of polyelectrolyte networks," Ph.D. dissertation, Johannes Gutenberg-University, Mainz, Germany, Dec. 2005.
- [95] G. S. Manning, "Limiting laws and counterion condensation in polyelectrolyte solutions I. colligative properties," *The Journal of Chemical Physics*, vol. 51, pp. 924–933, 1969.
- [96] T. Alfrey, P. W. Berg, and H. J. Morawetz, "The counterion distribution in solutions of rod-shaped polyelectrolyteS," *Journal of Polymer Science*, vol. 7, p. 543, 1951.
- [97] R. M. Fuoss, A. Katchalsky, and S. Lifson, "The potential of an infinite rod-like molecule and the distribution of the counter ions," *Proceedings of the National Academy of Sciences of the United States of America*, vol. 37, pp. 579–589, 1951.
- [98] A. Katchalsky, S. Lifson, and J. Mazur, "The electrostatic free energy of polyelectrolyte solutions. i. randomly kinked macromolecules," *Journal of Polymer Science*, vol. 11, no. 5, pp. 409–423, 1953.
- [99] A. Deshkovski, S. Obukhov, and M. Rubinstein, "Counterion phase transitions in dilute polyelectrolyte solutions," *Physical Review Letters*, vol. 86, no. 11, pp.

2341–2344, 2001.

- [100] D. Antypov and C. Holm, “Optimal cell approach to osmotic properties of finite stiff-chain polyelectrolytes,” *Physical Review Letters*, vol. 96, p. 088302, 2006.
- [101] J.-L. Barrat, J.-F. Joanny, and P. Pincus, “On the scattering properties of polyelectrolyte gels,” *Journal de Physique II*, vol. 2, pp. 1531–1544, 1992.
- [102] J. Landsgesell, D. Sean, P. Kreissl, K. Szuttor, and C. Holm, “Modeling gel swelling equilibrium in the mean field: From explicit to poisson-boltzmann models,” *Physical Review Letters*, vol. 122, p. 208002, May 2019. [Online]. Available: <https://link.aps.org/doi/10.1103/PhysRevLett.122.208002>
- [103] A. Arnold and C. Holm, “MMM1D: A method for calculating electrostatic interactions in 1D periodic geometries,” *Journal of Chemical Physics*, vol. 123, no. 12, p. 144103, Sep. 2005.
- [104] T. Birshtein and V. A. Pryamitsyn, “Coil-globule type transitions in polymers. 2. theory of coil-globule transition in linear macromolecules,” *Macromolecules*, vol. 24, no. 7, pp. 1554–1560, 1991.
- [105] A. Cohen, “A padé approximant to the inverse langevin function,” *Rheologica acta*, vol. 30, no. 3, pp. 270–273, 1991.
- [106] T. Richter, J. Landsgesell, P. Košovan, and C. Holm, “On the efficiency of a hydrogel-based desalination cycle,” *Desalination*, vol. 414, pp. 28–34, 2017. [Online]. Available: <http://www.sciencedirect.com/science/article/pii/>

S001191641730139X

- [107] W. Hummel, U. Berner, E. Curti, F. Pearson, and T. Thoenen, *Nagra/PSI Chemical Thermodynamic Data Base 01/01*. Universal Publishers, 2002. [Online]. Available: <https://books.google.de/books?id=YSWbCgAAQBAJ>
- [108] C. P. Broedersz and F. C. MacKintosh, "Modeling semiflexible polymer networks," *Reviews of Modern Physics*, vol. 86, no. 3, p. 995, 2014.
- [109] W. Demtröder, *Experimentalphysik 1: Mechanik und Wärme*. Springer-Verlag Berlin, Heidelberg, New York, 2004.
- [110] A. Naji and R. R. Netz, "Scaling and universality in the counterion-condensation transition at charged cylinders," *Physical Review E*, vol. 73, no. 5, p. 056105, 2006.
- [111] S. Schneider and P. Linse, "Discontinuous volume transitions in cross-linked polyelectrolyte gels induced by short-range attractions and strong electrostatic coupling," *Macromolecules*, vol. 37, pp. 3850–3856, 2004.
- [112] J. Ricka and T. Tanaka, "Swelling of ionic gels: quantitative performance of the donnan theory," *Macromolecules*, vol. 17, no. 12, pp. 2916–2921, 1984. [Online]. Available: <http://pubs.acs.org/doi/abs/10.1021/ma00142a081>
- [113] M. Karbarz, W. Hyk, and Z. Stojek, "Swelling ratio driven changes of probe concentration in ph-and ionic strength-sensitive poly (acrylic acid) hydrogels," *Electrochemistry Communications*, vol. 11, 2009.

- [114] Y. H. Al-qudah, G. A. Mahmoud, and M. A. Khalek, "Radiation crosslinked poly (vinyl alcohol)/acrylic acid copolymer for removal of heavy metal ions from aqueous solutions," *Journal of Radiation Research and Applied Sciences*, vol. 7, 2014.
- [115] X. J. Liu, H. Q. Li, B. Y. Zhang, Y. J. Wang, X. Y. Ren, S. Guan, and G. H. Gao, "Highly stretchable and tough pH-sensitive hydrogels with reversible swelling and recoverable deformation," *RSC Advances*, 2016.
- [116] L. Arens, D. Barther, J. Landsgesell, C. Holm, and M. Wilhelm, "Poly (sodium acrylate) hydrogels: Synthesis of various network architectures, local molecular dynamics, salt partitioning, desalination and simulation," *Soft Matter*, 2019.
- [117] S. Panyukov and Y. Rabin, "Statistical physics of polymer gels," *Physics Reports*, vol. 269, no. 1–2, pp. 1–131, 1996.
- [118] M. Tehrani, M. H. Moshaei, and A. S. Sarvestani, "Network polydispersity and deformation-induced damage in filled elastomers," *Macromolecular Theory and Simulations*, vol. 26, no. 6, p. 1700038, 2017.
- [119] P. J. Flory, "Molecular size distribution in linear condensation polymers1," *Journal of the American Chemical Society*, vol. 58, no. 10, pp. 1877–1885, 1936.
- [120] C. Roland, "Interpenetrating polymer networks (ipn): structure and mechanical behavior," *Encyclopedia of polymeric nanomaterials*, pp. 1004–1011, 2015.
- [121] S. Edgecombe and P. Linse, "Monte carlo simulation of

- two interpenetrating polymer networks: Structure, swelling, and mechanical properties," *Polymer*, vol. 49, no. 7, pp. 1981–1992, Apr. 2008.
- [122] J. Landsgesell and C. Holm, "Cell model approaches for predicting the swelling and mechanical properties of polyelectrolyte gels," *arXiv preprint arXiv:1908.10804*, 2019.
- [123] M. Mussel, P. J. Basser, and F. Horkay, "Effects of mono-and divalent cations on the structure and thermodynamic properties of polyelectrolyte gels," *Soft matter*, vol. 15, no. 20, pp. 4153–4161, 2019.
- [124] J. G. Crespo and K. W. Böddeker, Eds., *Membrane Processes in Separation and Purification*. Dordrecht: Springer Netherlands, 1994.
- [125] J. B. Tasker, "Clinical Osmometry in Veterinary Medicine," *Bulletin of the American Society of Veterinary Clinical Pathologists*, vol. 4, no. 1, pp. 3–13, 1975.
- [126] B. D. Rose, *Clinical Physiology of Acid-Base Disorders*. Place of publication not identified: Mcgraw-Hill, 2011, oCLC: 704062347.
- [127] J. T. Daugirdas, P. G. Blake, and T. S. Ing, *Handbook of Dialysis*. S.l.: Wolters Kluwer Health, 2014, oCLC: 1105388949.
- [128] M. Mulder, *Basic Principles of Membrane Technology*, 1996, oCLC: 1105291754.
- [129] M. A. Shannon, P. W. Bohn, M. Elimelech, J. G. Georgiadis, B. J. Mariñas, and A. M. Mayes, "Science and technology

- for water purification in the coming decades," *Nature*, vol. 452, no. 7185, pp. 301–310, Mar. 2008.
- [130] J. Kucera, "Reverse osmosis," in *Kirk-Othmer Encyclopedia of Chemical Technology*, J. W. . S. Inc, Ed. Hoboken, NJ, USA: John Wiley & Sons, Inc., Jun. 2017, pp. 1–44.
- [131] J. van Rijssel, R. Costo, A. Vrij, A. P. Philipse, and B. H. Ern , "Thermodynamic Charge-to-Mass Sensor for Colloids, Proteins, and Polyelectrolytes," *ACS Sensors*, vol. 1, no. 11, pp. 1344–1350, Nov. 2016.
- [132] G. F. AZZONE, D. PIETROBON, and M. ZORATTI, "Determination of the proton electrochemical gradient across biological membranes," in *Current topics in bioenergetics*. Elsevier, 1984, vol. 13, pp. 1–77.
- [133] T. Davis, "Donnan dialysis," *Encyclopedia of separation science*, vol. 4, pp. 1701–1707, 2000.
- [134] A. Horta, M. J. Molina, M. R. G mez-Ant n, and I. F. Pi rola, "The ph inside a ph-sensitive gel swollen in aqueous salt solutions: Poly (n-vinylimidazole)," *Macromolecules*, vol. 42, no. 4, pp. 1285–1292, 2009.
- [135] O. E. Philippova, D. Hourdet, R. Audebert, and A. R. Khokhlov, "ph-responsive gels of hydrophobically modified poly (acrylic acid)," *Macromolecules*, vol. 30, no. 26, pp. 8278–8285, 1997.
- [136] P. W. Atkins, *Atkins Physical Chemistry, 6th edition*. Oxford University Publishing, 1998.
- [137] C. G. McCarty and E. Vitz, "ph paradoxes: Demonstrating

- that it is not true that  $\text{pH} \equiv -\log [\text{H}^+]$ ," *Journal of Chemical Education*, vol. 83, no. 5, p. 752, 2006.
- [138] W. R. Smith and R. W. Missen, "What is chemical stoichiometry?," *Chemical Engineering Education*, vol. 13, no. 1, pp. 26–32, 1979.
- [139] J. Carrero-Mantilla and M. Llano-Restrepo, "Chemical equilibria of multiple-reaction systems from reaction ensemble monte carlo simulation and a predictive equation of state: combined hydrogenation of ethylene and propylene," *Fluid phase equilibria*, vol. 242, no. 2, pp. 189–203, 2006.
- [140] V. S. Rathee, H. Sidky, B. J. Sikora, and J. K. Whitmer, "Role of associative charging in the entropy-energy balance of polyelectrolyte complexes," *Journal of the American Chemical Society*, vol. 140, no. 45, pp. 15 319–15 328, 2018.
- [141] V. Rathee, H. Sidky, B. Sikora, and J. Whitmer, "Explicit ion effects on the charge and conformation of weak polyelectrolytes," *Polymers*, vol. 11, no. 1, p. 183, Jan 2019.
- [142] W. Janke, "Statistical analysis of simulations: Data correlations and error estimation," *Quantum Simulations of Complex Many-Body Systems: from Theory to Algorithms*, pp. 423–445, 2002. [Online]. Available: <https://user.fz-juelich.de/record/24560/files/NIC-Band-10.pdf>
- [143] O. V. Borisov, E. B. Zhulina, F. A. Leermakers, M. Ballauff, and A. H. E. Müller, "Conformations and solution properties of star-branched polyelectrolytes," in *Self Organized Nanostructures of Amphiphilic Block Copolymers I*,



- ser. Adv. Polym. Sci., A. H. E. Müller and O. Borisov, Eds. Springer Berlin / Heidelberg, 2011, vol. 241, pp. 1–55.
- [144] P. Matějček, K. Podhajecka, J. Humpolicková, F. Uhlik, K. Jelinek, Z. Limpouchova, K. Prochazka, and M. Špírková, "Polyelectrolyte behavior of polystyrene-block-poly (methacrylic acid) micelles in aqueous solutions at low ionic strength," *Macromolecules*, vol. 37, no. 26, pp. 10 141–10 154, 2004.
- [145] P. Matějček, M. Uchman, J. Lokajová, M. Štěpánek, M. Špírková, and K. Procházka, "Multilayer polymeric nanoparticles based on specific interactions in solution: Polystyrene-block-poly (methacrylic acid) micelles with linear poly (2-vinylpyridine) in aqueous buffers," *Materials and Manufacturing Processes*, vol. 23, no. 6, pp. 557–560, 2008.
- [146] G. S. Longo, M. O. de la Cruz, and I. Szleifer, "Non-monotonic swelling of surface grafted hydrogels induced by pH and/or salt concentration," *The Journal of Chemical Physics*, vol. 141, no. 12, p. 124909, 2014.
- [147] J. Kielland, "Individual activity coefficients of ions in aqueous solutions," *Journal of the American Chemical Society*, vol. 59, no. 9, pp. 1675–1678, 1937.
- [148] M. Castelnovo, P. Sens, and J.-F. Joanny, "Charge distribution on annealed polyelectrolytes," *European Physical Journal E: Soft Matter*, vol. 1, pp. 115–125, 2000.
- [149] C. Shi, J. A. Wallace, and J. K. Shen, "Thermodynamic coupling of protonation and conformational equilibria in

- proteins: theory and simulation," *Biophysical Journal*, vol. 102, no. 7, pp. 1590–1597, 2012.
- [150] T. Tanaka, "Gels," *Scientific American*, vol. 244, no. 1, pp. 124–S, 1981.
- [151] C. Hofzumahaus, P. Hebbeker, and S. Schneider, "Monte carlo simulations of weak polyelectrolyte microgels: ph-dependence of conformation and ionization," *Soft Matter*, vol. 14, no. 20, pp. 4087–4100, 2018.
- [152] D. Sean, J. Landsgesell, and C. Holm, "Influence of weak groups on polyelectrolyte mobilities," *Electrophoresis*, vol. 40, no. 5, pp. 799–809, 2019.
- [153] A. E. English, S. Mafé, J. A. Manzanares, X. Yu, A. Y. Grosberg, and T. Tanaka, "Equilibrium swelling properties of polyampholytic hydrogels," *The Journal of chemical physics*, vol. 104, no. 21, pp. 8713–8720, 1996.
- [154] S. E. Kudaibergenov and V. B. Sigitov, "Swelling, shrinking, deformation, and oscillation of polyampholyte gels based on vinyl 2-aminoethyl ether and sodium acrylate," *Langmuir*, vol. 15, no. 12, pp. 4230–4235, 1999.
- [155] L. Chen, Y. Du, and R. Huang, "Novel ph, ion sensitive polyampholyte gels based on carboxymethyl chitosan and gelatin," *Polymer international*, vol. 52, no. 1, pp. 56–61, 2003.
- [156] Y. Ogawa, K. Ogawa, and E. Kokufuta, "Swelling-shrinking behavior of a polyampholyte gel composed of positively charged networks with immobilized polyanions," *Langmuir*, vol. 20, no. 7, pp. 2546–2552, 2004.

- [157] M. Zhai, Y. Chen, M. Yi, and H. Ha, "Swelling behaviour of a new kind of polyampholyte hydrogel composed of dimethylaminoethyl methacrylate and acrylic acid," *Polymer international*, vol. 53, no. 1, pp. 33–36, 2004.
- [158] T. L. Sun, T. Kurokawa, S. Kuroda, A. B. Ihsan, T. Akasaki, K. Sato, M. A. Haque, T. Nakajima, and J. P. Gong, "Physical hydrogels composed of polyampholytes demonstrate high toughness and viscoelasticity," *Nature materials*, vol. 12, no. 10, p. 932, 2013.
- [159] N. Adzic and R. Podgornik, "Kirkwood-shumaker interactions and general thermal fluctuation forces," *arXiv preprint arXiv:1401.5252*, 2014.
- [160] E. Y. Kramarenko, O. Philippova, and A. Khokhlov, "Polyelectrolyte networks as highly sensitive polymers," *Polymer Science Series C*, vol. 48, no. 1, p. 1, 2006.
- [161] R. G. Winkler, M. Gold, and P. Reineker, "Collapse of polyelectrolyte macromolecules by counterion condensation and ion pair formation: A molecular dynamics simulation study," *Physical Review Letters*, vol. 80, pp. 3731–3734, 1998.
- [162] P. de Buyl, P. H. Colberg, and F. Höfling, "H5md: A structured, efficient, and portable file format for molecular data," *Computer Physics Communications*, vol. 185, no. 6, pp. 1546–1553, 2014.
- [163] J. E. Hallett, D. A. Gillespie, R. M. Richardson, and P. Bartlett, "Charge regulation of nonpolar colloids," *Soft matter*, vol. 14, no. 3, pp. 331–343, 2018.

- [164] Y. Avni, T. Markovich, R. Podgornik, and D. Andelman, "Charge regulating macro-ions in salt solutions: screening properties and electrostatic interactions," *Soft matter*, vol. 14, no. 29, pp. 6058–6069, 2018.
- [165] Y. Avni, D. Andelman, and R. Podgornik, "Charge regulation with fixed and mobile charged macromolecules," *Current Opinion in Electrochemistry*, vol. 13, pp. 70–77, 2019.

## **Erklärung über die Eigenständigkeit der Dissertation**

Ich versichere, dass ich die vorliegende Arbeit mit dem Titel „Simulation and Modeling of Polyelectrolyte Gels“ selbständig verfasst und keine anderen als die angegebenen Quellen und Hilfsmittel benutzt habe; aus fremden Quellen entnommene Passagen und Gedanken sind als solche kenntlich gemacht. Diese Dissertation wurde zu keiner Zeit in derselben oder substantiell ähnlichen Version bei einem anderen Prüfungsamt eingereicht.

## **Declaration of Authorship**

I hereby certify that the dissertation entitled “Simulation and Modeling of Polymer Gels” is entirely my own work except where otherwise indicated. Passages and ideas from other sources have been clearly indicated. This thesis has never been submitted in the same or substantially similar version to any other examination office.

Name/ Name: \_\_\_\_\_

Unterschrift/ Signed: \_\_\_\_\_

Datum/ Date: \_\_\_\_\_